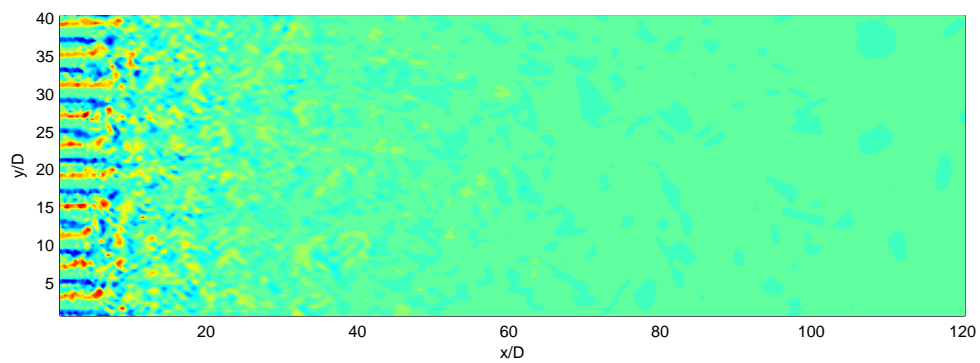


# Large-scale coherent structures in turbulent shallow flows



Wim van Balen  
June 2005

MSc Thesis  
Delft University of Technology  
Faculty of Civil Engineering and Geosciences  
Environmental Fluid Mechanics Section



# Large-scale coherent structures in turbulent shallow flows

MSc Thesis  
Wim van Balen, June 2005

Thesis Committee:  
prof.dr.ir. G.S. Stelling  
dr.ir. W.S.J. Uijttewaal  
dr. G.N. Wells  
ir. H. Talstra

*Cover: vorticity-patterns of a flow downstream of a grid of obstacles, simulated with a two-dimensional Transient Reynolds-Averaged Numerical Simulation with kinematic simulation, for  $Re_\tau = 590$ .*

©2005, Wim van Balen

*De laatste stap van het verstandelijk denken is de erkenning dat er oneindig veel dingen zijn die het te boven gaan. Als het aan dat inzicht niet toekomt, is het zwak. En als de natuurlijke dingen het al te boven gaan, wat moeten we dan niet zeggen van de bovennatuurlijke?*

Blaise Pascal (1623 - 1662)



# Abstract

Shallow flows are three-dimensional flows with two dimensions being significantly larger than the third dimension. Coherent structures, also called eddies, are areas in the flow, where velocity fluctuations are correlated, with a certain rotation. Although, generally, coherent structures of the order of the waterdepth contain most of the turbulent kinetic energy, compared to coherent structures of other length-scales, coherent structures of all length-scales have a certain amount of energy. This research was particularly focussed on the amount of energy of coherent structures with length-scales larger than the water-depth, the so-called supra-depth length-scales. It turned out, that these coherent structures are of large importance with regard to the, for quasi-two-dimensional flow characteristic, upcascading to larger length-scales, which is clearly visible by a peak-shift to the low-frequency side of the energy-density spectra. Considering that large-scale coherent structures are less dissipative compared to smaller-scale coherent structures, it can be inferred that imposing perturbations has a clear effect with respect to the conservation of turbulent kinetic energy in (by definition hypothetical) two-dimensional flows.

This knowledge can be used and applied in two-dimensional depth-averaged simulations (e.g. RANS, TRANS, etc.), where the large-scale part of general spectral distributions can be mimicked by a kinematic simulation. This thus formulated and used model (2D-TRANS+ks) has been applied to a channel flow with a grid of obstacles at the inflow boundary. Considering the quantities energy and enstrophy, and the energy-density spectra, the model performed reasonably well. Nevertheless, this model should be applied with care and a critical eye, as three-dimensional effects are difficult to represent in a two-dimensional model.



# Samenvatting

Ondiepe stromingen zijn drie-dimensionale stromingen met twee dimensies die significant groter zijn dan de derde dimensie. Coherente structuren, ook wel wervels genoemd, zijn gebieden in de stroming, waar snelheids-fluctuaties onderling gecorreleerd zijn, met een zekere rotatie. Hoewel in het algemeen coherente structuren met lengte-schalen gelijk aan de waterdiepte de meeste turbulent kinetische energie bevatten, hebben coherente structuren van alle mogelijke afmetingen een zekere hoeveel energie. Wij hebben specifiek gekeken naar de hoeveelheid energie die aanwezig is bij coherente structuren met een lengte-schaal groter dan de waterdiepte. Hieruit kwam naar voren dat de aanwezigheid van deze coherente structuren van groot belang is, als het gaat om de realisatie van het zelf-organisatie principe, dat kenmerkend is voor quasi-twee-dimensionale stromingen, hetgeen duidelijk zichtbaar werd in een verplaatsing van de initiële piekwaarde naar de lage-frequentie zijde van het energie-dichtheids spectrum. Gezien het feit dat hoe groter de lengte-schaal van een coherente structuur is, hoe minder dissipatief deze is, is het duidelijk dat het aanbrengen van verstoringen zijn effect oogst, als het gaat om het behoud van energie in een (per definitie hypothetische) twee-dimensionale stroming.

Deze opgedane kennis kan worden gebruikt en toegepast in twee-dimensionale, diepte-gemiddelde modellen (zoals RANS, TRANS, etc.), waarbij het grootschalige gedeelte van algemene spectrale verdelingen kan worden nagebootst met een kinematische simulatie. Het daartoe hier geformuleerde en gebruikte model (2D-TRANS+ks) is toegepast op een kanaalstroming met een rooster van obstakels bij de instroom-rand. Na een vergelijking van energie-verloop, enstrofie-verloop en energie-dichtheden, kon geconcludeerd worden dat het model behoorlijk goede resultaten gaf. Desalniettemin zal dit model in de toekomst met zorg en een kritisch oog dienen te worden toegepast, omdat het moeilijk is om drie-dimensionale effecten te representeren in een twee-dimensionaal model.



# Contents

<b>Abstract</b>	<b>vii</b>
<b>Samenvatting</b>	<b>ix</b>
<b>List of Tables</b>	<b>xv</b>
<b>List of Figures</b>	<b>xvi</b>
<b>1 Introduction</b>	<b>1</b>
1.1 Phenomenology . . . . .	2
1.2 Problem statement . . . . .	2
1.3 Methodology . . . . .	3
1.4 Outline of the thesis . . . . .	3
<b>2 Theory of turbulence</b>	<b>5</b>
2.1 General considerations . . . . .	5
2.1.1 Basic equations . . . . .	5
2.1.2 The problem of turbulence . . . . .	6
2.1.3 Energy considerations . . . . .	8
2.1.4 Turbulence close to a wall . . . . .	10
2.2 Shallow flows . . . . .	12
2.2.1 Turbulence in shallow flows . . . . .	12
2.2.2 Properties of 2D-turbulence . . . . .	12
2.3 Coherent structures . . . . .	14
2.3.1 Classification of coherent structures . . . . .	14
2.3.2 Very large-scale motions . . . . .	15
<b>3 Numerical modelling</b>	<b>17</b>
3.1 Turbulence modelling . . . . .	17
3.1.1 Direct Numerical Simulation . . . . .	17
3.1.2 Reynolds Averaged Numerical Simulation . . . . .	18
3.1.3 Large Eddy Simulation . . . . .	19
3.1.4 Detached Eddy Simulation . . . . .	21

3.1.5	Depth-Averaged Large Eddy Simulation . . . . .	22
3.2	Model description . . . . .	23
3.2.1	Spatial discretisation . . . . .	23
3.2.2	Temporal discretisation . . . . .	25
3.2.3	Boundary conditions . . . . .	27
3.2.4	Initial conditions . . . . .	29
<b>4</b>	<b>Channel flow</b>	<b>31</b>
4.1	Background and objective . . . . .	31
4.2	Numerical setup . . . . .	31
4.3	Results . . . . .	32
4.3.1	Validation . . . . .	32
4.3.2	Depth-averaged statistics . . . . .	35
4.3.3	Partial-depth-averaged statistics . . . . .	37
4.3.4	Overall statistics . . . . .	42
4.4	Discussion and conclusion . . . . .	42
<b>5</b>	<b>Kinematic simulation</b>	<b>45</b>
5.1	Depth-averaged simulation . . . . .	45
5.1.1	Shallow water equations . . . . .	45
5.1.2	Kinematic simulation . . . . .	46
5.1.3	Integrating the kinematic simulation with the shallow water equations . . . . .	48
5.2	Analysis of the method . . . . .	48
5.2.1	Imitating the energy-density spectra . . . . .	49
5.2.2	Imitating the velocity-field . . . . .	51
5.3	Multi-layered model . . . . .	52
<b>6</b>	<b>Influence of disturbances</b>	<b>55</b>
6.1	Background and objective . . . . .	55
6.2	Temporal development of coherent structures . . . . .	55
6.2.1	Numerical setup . . . . .	55
6.2.2	Perturbations . . . . .	57
6.2.3	Results . . . . .	58
6.3	Spatial development of coherent structures . . . . .	63
6.3.1	Numerical setup . . . . .	63
6.3.2	Perturbations . . . . .	64
6.3.3	Results . . . . .	64
6.4	Conclusion . . . . .	68
<b>7</b>	<b>Application of 2D-TRANS+ks</b>	<b>71</b>
7.1	Background and objective . . . . .	71
7.2	Numerical setup . . . . .	72
7.3	Results . . . . .	72

7.4	Conclusion and discussion . . . . .	76
<b>8</b>	<b>Conclusions and recommendations</b>	<b>79</b>
8.1	Overview . . . . .	79
8.2	Conclusions . . . . .	79
8.3	Recommendations . . . . .	80
	<b>Bibliography</b>	<b>81</b>
	<b>A List of calculations</b>	<b>83</b>
	<b>B Implementation aspects</b>	<b>85</b>
B.1	Non-dimensionality . . . . .	85
B.2	Large Eddy Simulation . . . . .	86
B.2.1	The algorithm . . . . .	86
B.2.2	The wall-function . . . . .	87
B.3	Transient Reynolds-Averaged Numerical Simulation . . . . .	87
B.3.1	Bottom friction . . . . .	88
B.3.2	Kinematic simulation . . . . .	88
	<b>C Postprocessing aspects</b>	<b>89</b>
C.1	One-dimensional spectral distributions . . . . .	89
C.2	Two-dimensional spectral distributions . . . . .	89
C.3	Averaging algorithms . . . . .	90
C.3.1	Depth-averaged velocity maps . . . . .	90
C.3.2	Grid-flow . . . . .	90
	<b>D List of Symbols</b>	<b>91</b>
	<b>Nawoord</b>	<b>95</b>



# List of Tables

4.1	Flow-geometry for the channel flow . . . . .	31
4.2	Three channel-flow cases . . . . .	32
4.3	Regions to be investigated . . . . .	38
5.1	Different values for $\alpha$ , for different $Re_\tau$ . . . . .	49
6.1	Flow-geometry for the vorticity-checkerboard . . . . .	56
6.2	Parameter settings for the vorticity-checkerboard . . . . .	56
6.3	Perturbation-intensities for the vorticity-checkerboard . . . . .	57
6.4	Imposed perturbations on meso-scale for the vorticity-checkerboard . . . . .	57
6.5	Imposed perturbations on macro-scale for the vorticity-checkerboard . . . . .	58
6.6	Flow geometry for the grid-flow . . . . .	63
6.7	Perturbation-intensities for the grid-flow . . . . .	64
6.8	Imposed perturbations for the grid-flow . . . . .	64
7.1	Flow geometry for the kinematic simulation . . . . .	72
A.1	Calculations . . . . .	83

# List of Figures

1.1	Coherent structures in the Bering Sea . . . . .	1
2.1	General energy density spectra . . . . .	9
2.2	Structure of the wall region . . . . .	10
2.3	Velocity-profiles in the wall-region . . . . .	11
2.4	Evolution of a general spectral distribution . . . . .	14
3.1	Energy-density spectra decomposition for four turbulence modelling methods . . . . .	18
3.2	Computational domain with parallellisation . . . . .	24
3.3	A grid cell of the staggered grid . . . . .	24
3.4	Principle of free-slip and no-slip boundary-conditions . . . . .	28
4.1	Computational domain for the channel flow . . . . .	32
4.2	Velocity profiles . . . . .	33
4.3	1D energy-density spectra . . . . .	34
4.4	1D, depth-averaged, energy-density spectra . . . . .	35
4.5	2D, depth-averaged, energy-density spectra . . . . .	36
4.6	Integrated 2D energy-density spectra . . . . .	37
4.7	Integrated spectra, per half-depth . . . . .	39
4.8	Integrated spectra for a part of the water-depth, 1 . . . . .	40
4.9	Integrated spectra for a part of the water-depth, 2 . . . . .	40
4.10	Integrated spectra, for three values of $z/D$ . . . . .	41
4.11	Integrated spectra, for three values of $z^+$ . . . . .	43
5.1	Imitated 2D energy-density spectra . . . . .	49
5.2	Dependency of $\alpha$ on $Re_\tau$ . . . . .	50
5.3	Imitated 1D energy-density spectra . . . . .	50
5.4	Imitated velocity-fields and vorticity-field . . . . .	51
5.5	Depth-averaged two-dimensional energy-density spectra . . . . .	52
5.6	Imitated 2D energy-density spectra, alternative . . . . .	53
5.7	Imitated 1D energy-density spectra, alternative . . . . .	53
6.1	Computational domain for the vorticity-checkerboard . . . . .	56
6.2	Development of energy and enstrophy, micro-scale case . . . . .	58

6.3	Merging-process . . . . .	59
6.4	Development of energy, meso-scale case . . . . .	60
6.5	Development of energy, macro-scale case . . . . .	61
6.6	Comparison of micro-scale case and macro-scale case . . . . .	62
6.7	Inflow-boundary for the grid-flow . . . . .	63
6.8	Vorticity patterns for grid-flow in a 2D-setting and in a 3D-setting. . . . .	65
6.9	Energy-curves for 2D grid-flow . . . . .	66
6.10	Energy-curves and enstrophy-curves for 2D grid-flow . . . . .	67
6.11	Energy-curves and enstrophy-curves for 3D grid-flow . . . . .	68
6.12	Energy-density spectra in the near-field and the far-field. . . . .	69
7.1	Vorticity patterns for comparison of 2D-TRANS+ks with 3D-LES . . . . .	73
7.2	Profile of streamwise velocities in the far-field . . . . .	74
7.3	Energy-curves and enstrophy-curves for 3D grid-flow . . . . .	74
7.4	Energy-curves and enstrophy-curves for the 2D-TRANS+ks case. . . . .	75
7.5	Energy-density spectra in the near-field and the far-field. . . . .	76



# Chapter 1

## Introduction

Coherent structures, or eddies, are an often occurring phenomenon in civil engineering practice. They are seen in rivers, seas and oceans, for instance in the wake of an island and in shear flows, and have been, with their often spectacular appearances, an interesting subject for scientific studies for years. One of these spectacular examples is seen in the Bering Sea, see Figure 1.1.

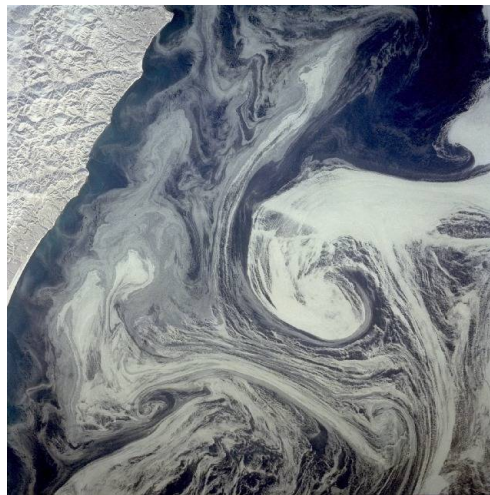


**Figure 1.1:** Coherent structures in the Bering Sea (adapted from <http://www.navis.gr/meteo/eddies.htm>). Sizes of the picture scale with about  $100 \times 100 \text{ km}^2$ .

Figure 1.1 shows a clear example of a large-scale eddy made visible by sea ice, just off the coast of the eastern Kamchatka Peninsula in the Bering Sea, that can be seen in this north-northwest-looking low-oblique view. The Bering Sea is a northward extension of the Pacific Ocean between Siberia (including the Kamchatka Peninsula) and Alaska. It is screened from the Pacific Ocean proper by the Aleutian Islands. The Bering Sea is frozen over from mid to late October until late May. The south-southwest flowing Oyashio Current brings cold waters from the Arctic Ocean through the shallow Bering Strait and the Bering Sea. This cold current meets with the warm northeast flowing Kuroshio Current off the coast of the northern Japanese Islands to form the east flowing Kuroshio extension. In this view, sea ice is visible flowing in the

Oyashio Current. Gyresa, or spiral eddies, existing within the current near the sea surface move the sea ice into circular patterns. Snow cover (white) covers the thicker ice flows just to the right of the center of the image.

As coherent structures appear clearly visible in flows very often and as their dynamics have clear influences on the flow and their associated mixing and transport processes, it is relevant to have insight in the physical behaviour of these structures. Generally, eddy structures with a length-scale of the order of the water-depth are the most energetic ones. Nevertheless, coherent structures of each possible length-scale, larger than these most energetic eddies, occur, all with a certain amount of energy. For this thesis, research was particularly focussed on the structure and energy of the very large-scale motion, as well as its influence to the flow as a whole. This is relevant for dealing with the dynamics in environmental flows, like separating flows, wakes, etc. which often occur in civil engineering practice.

## 1.1 Phenomenology

In three-dimensional flows, turbulent kinetic energy is dissipated by the vortex-stretching mechanism, that transfers the energy to the small scales via the energy cascade. Since this vortex-stretching mechanism is absent in (by definition hypothetical) two-dimensional flows, the energy is transferred to the small scales via the enstrophy cascade, together with an inverse energy cascade. This inverse energy cascade, or self-organisation principle, is visible by the shift of energy to the large scales. The rate at which quasi two-dimensional motion can bring energy into the largest scales has substantial consequences for the decay of turbulent kinetic energy. Previous research (Van Prooijen (2003)) has shown that the development of quasi two-dimensional eddy structures in unstable flows is much affected by the amplitude of random disturbances on a so-called supra-depth scale (length-scales larger than the water-depth).

As three-dimensional Direct Numerical Simulations and Large Eddy Simulations are computationally very expensive for large domains, as usual in civil engineering practice, in the past, several attempts were made to represent the effects of the three-dimensionality in a two-dimensional simulation. The development of two-dimensional simulations, taking into account the three-dimensional physical mechanisms, are of large importance within the context of applications in civil engineering practice. In this context, the PhD dissertations of Van Prooijen (2003) and Hinterberger (2004) are of significant importance. Van Prooijen uses a two-dimensional Reynolds Averaged Numerical Simulation together with a kinematic simulation for the representation of the very-large-scale motions, while Hinterberger uses a two-dimensional LES with a stochastic back-scatter model.

## 1.2 Problem statement

In view of the current status of knowledge and the current presence of modelling tools, the research of this thesis addresses several aspects:

1. A profound study must be made of the structure of large-scale coherent structures in turbulent, shallow channel flows. What can be said about the distribution of energy over the wavenumber range, and to what extent do these distributions differ from each other with increasing wall-normal distance, both if depth-averaging is applied and if not?
2. What is the influence of large-scale disturbances on the development of the flow and the amount of turbulent kinetic energy in it?

3. The two-dimensional model of Van Prooijen (2003) must be applied and compared with a full 3D-LES computation to see if it performs well and is able to represent three-dimensional coherent structures and their influences. Besides this, it must be investigated to what extent it makes sense to extend and how we actually can extend this two-dimensional model with new spectral information.

Several links between these three issues are present, namely 1 – 2: existence and influence of coherent structures with supra-depth length-scales, 1 – 3: existence and representation of these coherent structures and 2 – 3: quality of the representation of the influences of these coherent structures in a two-dimensional simulation.

### 1.3 Methodology

In order to investigate the structure of the large-scale motions three-dimensional Large Eddy Simulations will be carried out on a turbulent, shallow channel flow, at three different Reynolds-numbers. One-dimensional and two-dimensional spectral distributions will give information on the structure and energy content of the occurring coherent structures. Moreover, the information that follows from this investigation can be used for the improvement of the kinematic simulation model of Van Prooijen.

Two-dimensional Large Eddy Simulations will be carried out on flows with supra-depth disturbances to see what the influences of these disturbances really are. This is done for two cases: a case where the influences are measured as a function of time, namely a checkerboard of eddies with alternating sign of vorticity, and a case where the influences are measured as a function of space, namely a flow behind a grid of obstacles. Three-dimensional Large Eddy Simulations are carried out in order to see to what extent the bottom-induced turbulence acts as a disturber on supra-depth length-scales. These three-dimensional Large Eddy Simulations are only carried out on the grid-flow.

The grid-flow is also used for a proper case to test the performance of the model of Van Prooijen on. The model is used to see whether or not the kinematic simulation is able to simulate the influence of the bottom-induced turbulence well. For a good comparison, three-dimensional Large Eddy Simulations are carried out.

### 1.4 Outline of the thesis

First an overview is given on basic theories on turbulence, shallow flows and coherent structures (chapter 2). After that, chapter 3 continues with giving an overview of the current status of modelling tools, both in three-dimensional domains as in two-dimensional domains, whereafter the used Large Eddy Simulation is described in mathematical terms. From chapter 4 unto chapter 7 the proposed methodology is strictly followed: chapter 4 investigates the (spectral) structure of large-scale coherent structure in a shallow channel flow, which can be used for making the kinematic simulation more general (chapter 5), i.e. the dependency on the Reynolds-number can be taken into account. In chapter 5, the equations to be solved in a depth-averaged, time dependent model are described, where the large-scale motions are represented by a kinematic simulation. In chapter 6 the influences of the supra-depth disturbances on the flow (in a temporal and a spatial sense) are studied. At the end, in chapter 7, the two-dimensional, depth-averaged model with kinematic simulation is tested on the grid-flow.



# Chapter 2

## Theory of turbulence

In this chapter, an overview is given of some basic and generally accepted theories about turbulence. Successively, general considerations are made and some aspects of turbulence in shallow flows are dealt with. The theories presented in this chapter form the underlying basis for the following chapters.

### 2.1 General considerations

#### 2.1.1 Basic equations

Classical physics provides conservation laws that fully govern the dynamics of a fluid, namely conservation of mass, momentum and energy. From these laws, partial differential equations can be derived. It is customary to formulate the conservation laws under the assumption that the fluid is a continuous medium (*continuum hypothesis*). For a short derivation of the equations given below the book by Wesseling (2001) is recommended.

#### Definitions

In the following, a channel flow is considered where  $x$  represents the streamwise coordinate, while  $y$  and  $z$  represent the transverse and wall-normal coordinates respectively. The Cartesian coordinate system will be denoted either  $(x, y, z)$  or  $(x_1, x_2, x_3)$ , for convenience. Similarly, the velocity vector is denoted  $(u, v, w)$  or  $(u_1, u_2, u_3)$ . Also the Einstein summation convention is used, unless mentioned otherwise.

#### Continuity

The first equation that can be derived from the conservation laws is the continuity equation using the principle of conservation of mass. Assuming incompressibility of the flow, the continuity equation reads:

$$\frac{\partial u_i}{\partial x_i} = 0, \tag{2.1}$$

for  $i = 1, 2, 3$ . The velocity field is then said to be divergence free or solenoidal.

### The Navier-Stokes equations

The law of conservation of momentum applied to a material volume gives

$$\frac{\partial \rho u_i}{\partial t} + \frac{\partial \rho u_i u_j}{\partial x_j} = \frac{\partial \tau_{ij}}{\partial x_j} + \rho f_i^b, \quad (2.2)$$

for  $i, j = 1, 2, 3$ , where  $\tau_{ij}$  represents the stress tensor and  $\rho f_i^b$  represents the body force. Together with the constitutive relation for the stress tensor for Newtonian fluids and with the assumption of incompressibility of the flow, equation (2.2) results in the well-known incompressible Navier-Stokes equations:

$$\frac{\partial u_i}{\partial t} + \frac{\partial u_i u_j}{\partial x_j} = -\frac{1}{\rho} \frac{\partial p}{\partial x_i} + \nu \frac{\partial^2 u_i}{\partial x_j^2} \quad (2.3)$$

with  $\nu$  the kinematic viscosity. The vector-notation equivalents of (2.1) and (2.3) respectively, are:

$$\nabla \cdot \mathbf{u} = 0 \quad (2.4)$$

$$\frac{\partial \mathbf{u}}{\partial t} + (\mathbf{u} \cdot \nabla) \mathbf{u} = -\frac{1}{\rho} \nabla p + \nu \nabla^2 \mathbf{u} \quad (2.5)$$

which are the equations that fully describe fluid motions.

### The Reynolds number

When making equation (2.3) dimensionless by using a typical length-scale  $L$ , a typical velocity-scale  $U$  and a suitable value for the density  $\rho_r$  we obtain

$$\frac{\partial u_i}{\partial t} + \frac{\partial u_i u_j}{\partial x_j} = -\frac{\partial p}{\partial x_i} + \frac{1}{Re} \frac{\partial^2 u_i}{\partial x_j^2} \quad (2.6)$$

where the Reynolds-number appears as the governing parameter:

$$Re = \frac{\rho_r U L}{\mu} = \frac{U L}{\nu}.$$

The dynamic viscosity  $\mu$  is related to the kinematic viscosity  $\nu$  by  $\nu = \mu/\rho_r$ . The Reynolds number is the only remaining parameter in the dimensionless Navier-Stokes equations and turns out to be a measure of inertial and viscous forces in the flow: for  $Re \ll 1$  viscous stresses dominate and for  $Re \gg 1$  advection dominates. For very large values of  $Re$ , the flow is whirling and chaotic and therefore called *turbulent*.

#### 2.1.2 The problem of turbulence

In principle, equations (2.1) and (2.3) contain all features of incompressible flow of Newtonian fluids. As we have four equations with four unknowns, it is possible to describe the solutions perfectly. However, in real-life flows at moderate and high Reynolds numbers, the flow acts as a chaotic dynamic system. Obviously, this has to do with instabilities and non-linearities of the solutions. Hence, a proper description of the 'perfect' solution given some initial and boundary conditions is impossible.

### The Reynolds equations

For many applications in civil engineering, it is useful to specifically aim at solving for the mean motion while ignoring the fluctuations in the motion. Therefore the velocity vector and the pressure are separated into two parts: an ensemble average component and a fluctuating component respectively:

$$u_i = \bar{u}_i + u_i' \quad \text{and} \quad p = \bar{p} + p' \quad (2.7)$$

Substitution of equation (2.7) into equation (2.3) results in the so-called Reynolds equations:

$$\frac{\partial \rho \bar{u}_i}{\partial t} + \frac{\partial \rho \bar{u}_i \bar{u}_j}{\partial x_j} + \frac{\partial \overline{\rho u_i' u_j'}}{\partial x_j} = -\frac{\partial \bar{p}}{\partial x_i} + \mu \frac{\partial^2 \bar{u}_i}{\partial x_j^2} \quad (2.8)$$

The expression  $\overline{\rho u_i' u_j'} = q_{ij} = q_{ji}$  is called the Reynolds stress tensor which is symmetric and contains nine components (normal stresses and shear stresses). When only focussing on the mean flow the fluctuation term (the third term in equation (2.8)), closure is required in some way.

### Closure problem and Prandtl's hypothesis

One method to solve the problem is simply to write down and solve the transport equations for the Reynolds stresses. But it is easily seen that within this method higher order correlations of fluctuating velocity components will arise. This would become a never ending story which can only be disrupted by assumptions about higher order covariances.

Another approach is based on the assumption of gradient-type transports which means that turbulent transports are assumed to be proportional to gradients of the concerned quantities in the mean motion. This kind of approaches always implies the use of an eddy-viscosity  $\nu_t$ , which is a product of a characteristic length scale and a characteristic velocity.

An often used assumption for gradient-type transport is Prandtl's mixing-length hypothesis. This hypothesis supposes that a fluid-particle during its motion fully mixes with its surroundings after a displacement over a certain distance. A measure for this distance is the so-called mixing-length  $l_m$ . When considering the transport of  $x$ -momentum in  $z$ -direction, a fluid-particle from a distance  $l$  has a velocity deviation

$$u' = \pm l \frac{\partial \bar{u}}{\partial z} \quad (2.9)$$

and  $w'$  of the same order of magnitude. The transport of momentum becomes:

$$q_{zx} = \overline{\rho u' w'} = -\rho l_m^2 \left| \frac{\partial \bar{u}}{\partial z} \right| \frac{\partial \bar{u}}{\partial z} = -\rho \nu_t \frac{\partial \bar{u}}{\partial z} \quad (2.10)$$

The variable  $l_m$  is slightly deviating from  $l$  because of differences between  $u$  and  $w$  and their mutual correlation. At boundary layers the expression

$$l_m = \kappa z \quad (2.11)$$

is often used, with  $\kappa$  the Von Karman constant equal to 0.4 and  $z$  the distance from the wall.

### 2.1.3 Energy considerations

Having applied the conservation laws for mass and momentum, the conservation law for energy has not been used yet. With the density  $\rho$  (which is a constant) we basically describe the energy per unit of volume, the energy density. This property can be recognised when considering the total kinetic energy of the flow and applying the Reynolds decomposition:

$$\bar{q} = \frac{1}{2} \overline{\rho u_i u_i} = \frac{1}{2} \rho \bar{u}_i \bar{u}_i + \frac{1}{2} \overline{\rho u_i' u_i'}. \quad (2.12)$$

The total balance equation for energy can simply be derived by multiplying equation (2.3) by  $u_i$ . The energy balance equation for the mean motion and the turbulent motion can be derived by multiplying (2.8) by  $\bar{u}_i$  and (2.3) minus (2.8) by  $u_i'$  respectively. For a proper description of this equations the book by Pope (2000) is recommended.

#### Energy cascade

From the energy balance equations for the mean motion and the turbulent motion it can be seen that energy is transferred from the large mean motion scales to the small turbulent motion scales, due to non-linearity of the equations. Finally, dissipation of energy takes place by transferring energy from the smallest scales, the so-called Kolmogorov-scales, into heat. This transfer is called the *energy cascade*. Nature makes this process feasible through vortex stretching.

#### Spectral representation

To describe the energy content of the large scales and the small scales, the so-called energy density spectra are used. These spectra represent the distribution of energy densities as a function of the occurring time scales or space scales. From a registration in time of a velocity component  $u_1$  an energy spectrum  $E_1(\omega)$  can be determined:

$$E_1(\omega) = \frac{1}{2} \rho R_{11}(\omega), \quad (2.13)$$

in which  $R_{11}(\omega)$  is the Fourier-transform of the auto-covariance function  $r_{11}(\tau) = \overline{u_1'(t)u_1'(t+\tau)}$ :

$$R_{11}(\omega) = \frac{1}{2\pi} \int_{-\infty}^{+\infty} r_{11}(\tau) e^{-i\omega\tau} d\tau, \quad (2.14)$$

where the angular velocity  $\omega = 2\pi f$  is used (where  $f$  is the frequency). The total amount of kinetic energy can be found by integrating:

$$(q_t)_1 = \int_{-\infty}^{+\infty} E_1(\omega) d\omega. \quad (2.15)$$

In order to extend our interest to three dimensions we write

$$E(\omega) = \sum_{i=1}^3 E_i(\omega),$$

and so we get:

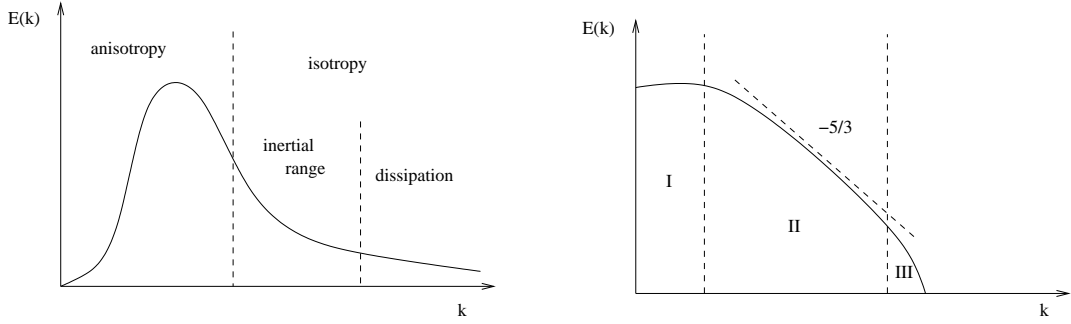


**Figure 2.1:** Energy density spectra. On the left the three-dimensional spectrum, on the right the one-dimensional spectrum (both axes logarithmic).

$$q_t = \int_{-\infty}^{+\infty} E(\omega) d\omega \quad \text{with} \quad E(\omega) = \frac{1}{2} \rho \sum_{i=1}^3 R_{ii}(\omega) \quad (2.16)$$

for the total amount of energy.

When assuming the eddies not changing during the passage time within the measure volume the length-scales become proportional to the time-scales:

$$\lambda_i = \bar{u}_i \tau$$

which is called Taylor's hypothesis of frozen turbulence. Using this hypothesis in all expressions (2.13) to (2.15),  $\omega$  can be replaced by the wavenumber  $k_1$  ( $k_i = \omega/\bar{u}_i$ ). One-dimensional spectra just give the distribution over the length-scales in one direction. In order to obtain insight in the length-scales, that really occur, the three-dimensional spectrum is needed. The spectrum  $E(k)$  is obtained by integration of  $E(k_1, k_2, k_3)$  over wave vectors of the same magnitude,  $k$ . So we get

$$q_t = \int_0^{\infty} E(k) dk \quad (2.17)$$

with  $k$  being the Euclidian norm of vector  $k_i$ .

### Spectral characteristics

Within the three-dimensional spectrum, we can distinguish three important ranges. Firstly, there is a range for small values of  $k$  (large length scales) which contains the eddies with large amounts of energy. This is called the anisotropy range because the eddies are affected in their direction by the main motion. Secondly, there is at larger wavenumbers an inertial range where isotropy reigns. This range is called inertial because in this range the advection dominates while it is not significantly affected by viscosity (high Reynolds-numbers). Thirdly at the high wavenumber end dissipation dominates.

When we take a look at the one-dimensional spectrum (see Figure 2.1 on the right), we obviously see the same three regions: region I is the production range, where energy is transferred from the mean motion to the turbulent motion and where spectral behaviour has not been identified specifically, II is the inertial subrange and III is the viscous range where spectra decay much faster than in the inertial subrange, due

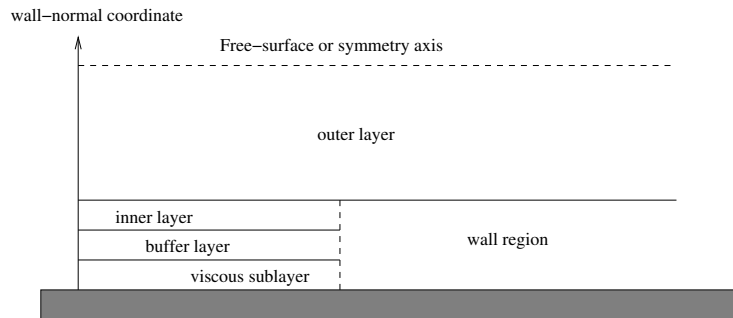


**Figure 2.2:** Wall region.

to dissipation. Kolmogorov (1941) argued that the amount of energy  $\epsilon$  that enters the inertial range must also leave the inertial range to be dissipated on the smallest scales and that therefore  $\epsilon$  can be used for the scaling of the spectral distribution. On dimensional arguments, he found

$$E(k) = \alpha \epsilon^{\frac{2}{3}} k^{-\frac{5}{3}} \quad (2.18)$$

with  $\alpha$  a dimensionless constant.

#### 2.1.4 Turbulence close to a wall

In civil engineering practice, we often have to deal with shear flows. Shear flows are flows with little variation in stream-wise direction, and larger variation in the direction perpendicular to the stream-wise direction. A common example of a shear flow is the flow near a wall. Because of a no-slip condition, a strong velocity gradient arises which is the cause of a *boundary layer*. In this section we present an overview of the structure of this boundary layer, together with some notions about velocity profiles and spectral laws. In this analysis we distinguish a wall region and an outer region.

##### The wall region

In the analysis of the wall region two assumptions are generally accepted:

**Hypothesis 1** *The shear stress  $\tau$  is approximately constant and equal to  $\tau_0 = \rho u_*^2$ . The production of the total turbulence energy  $P$  is approximately equal to the energy dissipation  $\epsilon_d$ :  $P \approx \epsilon_d \sim u_*^3/z$ .*

**Hypothesis 2** *The mean flow instability and velocity shear generate a hierarchy of eddies attached to the wall so that their characteristic scales are proportional to the distance  $z$  from the wall (equations (2.9) – (2.11)).*

Here we define  $u_*$  to be time- or plane-averaged friction velocity. We mention that the assumption of a constant shear stress can be applied up to about one fifth of the waterdepth without a large error. The structure of the wall-region is as given in Figure 2.2. Within the layer closest to the wall, viscous effects dominate and is therefore called the viscous sublayer. In the layer closest to the outer region, turbulent shear stresses dominate and this region is called the inner layer. Between these two layers a transition

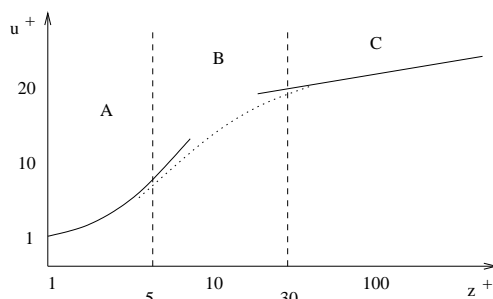


**Figure 2.3:** Velocity-profiles for the wall region: A is the viscous sublayer (see (2.19)), B is the buffer layer and C is the inner layer (see (2.20)).

region is found where both the viscous and the turbulent shear stresses are important. This layer is called the buffer layer.

With  $z^+ = zu_*/\nu$  as the non-dimensional wall coordinate and  $u^+ = u/u_*$ , velocity profiles are found (see for instance Pope (2000)). For the viscous sublayer:

$$u^+ = z^+ \quad (2.19)$$

and for the inner layer:

$$u^+ = \frac{1}{\kappa} \ln z^+ + B \quad (2.20)$$

where often  $B$  is chosen to be equal to 5.5. Because of the transition-character of the buffer layer no pronounced velocity profile has been found for this layer.

In Figure 2.3 the velocity-profiles for the wall region are plotted schematically.

### The outer layer

Within the outer layer we still have a dominant turbulent shear stress. However, the difference with the wall region is now that hypothesis 1 is not valid anymore. Together with that it is not yet clear how to express the relation between a characteristic mixing-length and the wall-normal coordinate  $z/h$ . Therefore the velocity profile of the outer layer is based on empirical approximations. An often used approximation is the velocity defect law:

$$\frac{\bar{u} - U_0}{u_*} = \frac{1}{\kappa} \ln \frac{z}{h} + B' \quad (2.21)$$

with  $U_0$  a characteristic velocity and  $h$  a characteristic length scale, for instance the waterdepth. In practice fiddling with  $B'$  together with a correction function is needed in order to match the outer layer with the inner layer and to account for some deviations near the free surface.

### Spectral law

It was shown that in the one-dimensional spectrum three regions can be distinguished. However, experimental work suggests that there is a transition region between regions I and II (see Figure 2.1) where

a  $k^{-1}$  spectral law is valid for wall-bounded turbulence. Nikora (1999) gives a theoretical basis for this behaviour by suggesting (using hypothesis 2) that at each distance  $z$  from the wall a separate energy cascade is initiated which is *superposed* with other energy cascades initiated at other  $z$ 's. After all, energy injection takes place at each  $z$  by eddies with a characteristic length-scale proportional to  $z$  (see (2.11)). So we have  $l_m \sim z$  from hypothesis 2 and  $z \sim k^{-1}$  from the suggestion of superposition. If we now use hypothesis 1, the following expression is obtained:

$$\epsilon(k) \sim u_*^3 k \quad \text{for} \quad \frac{1}{H} \leq k \leq \frac{1}{z} \quad (2.22)$$

where  $H$  is an external scale of the flow (e.g. the thickness of the boundary layer) and  $z$  the distance from the wall. This proportionality results in:

$$E(k) \sim \epsilon^{\frac{2}{3}} k^{-\frac{5}{3}} \sim u_*^2 k^{-1} \quad \text{for} \quad \frac{1}{H} \leq k \leq \frac{1}{z}. \quad (2.23)$$

Nikora (1999) also argued that this proportionality is also valid for the velocity co-spectra (spectra based on correlation between velocities  $u'_i$  and  $u'_j$ ,  $i \neq j$ ).

## 2.2 Shallow flows

### 2.2.1 Turbulence in shallow flows

One of the main features of turbulence is three-dimensional vorticity fluctuations. Being rotational and three-dimensional is typical of turbulence, and vorticity fluctuations can not maintain themselves in a two-dimensional space. However, many turbulent flows in nature have one dimension which is significantly smaller than the other two dimensions, such that these flows can be approximated as two-dimensional, for instance atmospheric flows and river flows. Such flows are called shallow flows. In that case it is tempting to consider the large scale turbulent motion as two-dimensional turbulence, despite the contradictory character of this term. This kind of turbulence forms a very interesting subject of research as it exhibits totally different features in comparison with three-dimensional turbulence. In this paragraph these differences become clear by giving the main properties of two-dimensional turbulent flows.

### 2.2.2 Properties of 2D-turbulence

#### Vorticity equation

The vorticity field of a flow is defined by the curl of the velocity:

$$\boldsymbol{\omega} = \nabla \times \mathbf{u},$$

which has in two dimensions only one non-zero component which is orthogonal to the plane of velocity, resulting in

$$\omega = \omega_z = \frac{\partial v}{\partial x} - \frac{\partial u}{\partial y}.$$

By introducing the streamfunction  $\psi$  such that

$$u = -\frac{\partial\psi}{\partial y} \quad \text{and} \quad v = \frac{\partial\psi}{\partial x},$$

one can write the vorticity  $\omega$  as the Laplacian of the streamfunction  $\psi$ :

$$\omega = \frac{\partial^2\psi}{\partial x^2} + \frac{\partial^2\psi}{\partial y^2} = \nabla^2\psi.$$

It is convenient to rewrite the two-dimensional Navier-Stokes equations in terms of the vorticity scalar field:

$$\frac{\partial\omega}{\partial t} + \mathbf{u} \cdot \nabla\omega = (\omega \cdot \nabla)\mathbf{u} + \nu\nabla^2\omega. \quad (2.24)$$

The first term of (2.24) represents the temporal evolution of the vorticity, the second term is an advection term, the third is the stretching term and the fourth represents the viscous effects.

### Vortex stretching

The most striking difference between 3D- and 2D-turbulence is the *vortex stretching* effect. If a vortex is stretched, matter is pulled towards the rotation axis of the vortex. Obeying the conservation law for angular momentum, the consequence is that this matter will rotate faster. Since 2D-flows have a third dimension of no practical importance, this vortex stretching effect is absent, because the vorticity vector is perpendicular to the velocity-field. Due to the absence of the vortex stretching effect, the third term in the vorticity equation (2.24) vanishes. When the inviscid limit of  $\nu = 0$  is considered, equation (2.24) becomes:

$$\frac{\partial\omega}{\partial t} + \mathbf{u} \cdot \nabla\omega = 0. \quad (2.25)$$

In other words, in two-dimensional inviscid flows the vorticity  $\omega$  is conserved. Analogously to the concept of kinetic energy, a quantity  $\Omega$  can be defined:

$$\Omega = \frac{1}{2}\omega'^2.$$

This quantity  $\Omega$  (also conserved) is called the enstrophy.

### Spectral characteristics

With 2D-turbulence, two conservation laws are important: conservation of kinetic energy  $q_t = \frac{1}{2}u_i^2$  and conservation of enstrophy  $\Omega = \frac{1}{2}\omega'^2$ . These can be written in spectral form:

$$q_t = \int_0^\infty E(k)dk = \text{constant}, \quad (2.26)$$

$$\Omega = \int_0^\infty k^2 E(k)dk = \text{constant}, \quad (2.27)$$

where  $E(k)$  is again the spectral energy density. Obviously,  $\Omega$  can statistically be considered as the second moment of  $E(k)$ . It has been conjectured by Kraichnan (1967) that the existence of conservation expressions (2.26) and (2.27) implies a simultaneous transfer of energy towards the large scales of motion and

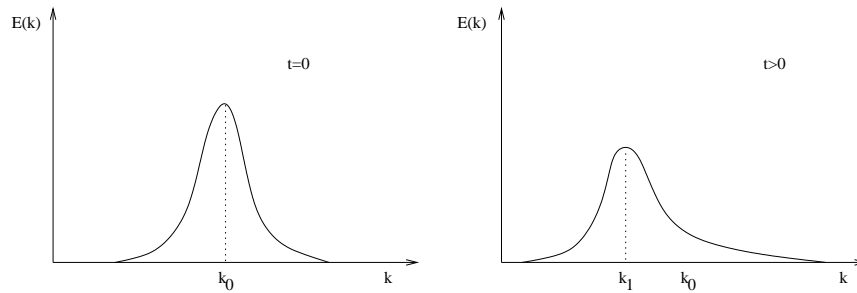


**Figure 2.4:** Evolution in time of a hypothetical spectral distribution of kinetic energy in a 2D-flow.

a transfer of enstrophy to the small scales of motion. Actually, the transfer of energy to the larger scales is the opposite as observed in 3D-turbulent flows and is therefore called the *inverse energy cascade*. The transfer of enstrophy to the smaller scales is called the *enstrophy cascade*. The inverse energy cascade is called the self-organisation principle of 2D-turbulence. Kraichnan (1967) found in his theory two expressions for power-laws in the energy density spectra, both on dimensional arguments. For the inverse energy cascade:

$$E(k) \sim \epsilon^{\frac{2}{3}} k^{-\frac{5}{3}} \quad \text{for} \quad k < k_i, \quad (2.28)$$

and for the enstrophy cascade:

$$E(k) \sim \eta^{\frac{2}{3}} k^{-3} \quad \text{for} \quad k > k_i, \quad (2.29)$$

with  $k_i$  the wave number associated with the injection scale of the forcing,  $\epsilon$  the rate of energy transfer and  $\eta$  the rate of enstrophy transfer. The kinetic energy of the flow thus concentrates after a while in large-scale vortices, which are often very stable and weakly dissipative.

The development of the spectrum in time is clearly made visible in Van Heijst (1993). Consider the evolution of a spectral distribution of kinetic energy in a 2D-flow (see Figure 2.4). The spectrum is spread out in time due to nonlinear interactions in the flow. Because of equation (2.26) the peak value will decrease and because (2.27) (the statistical second moment of  $E(k)$ ) the energy flux to the small length scales will be compensated by a much larger energy flux to the large length scales.

## 2.3 Coherent structures

### 2.3.1 Classification of coherent structures

Visually one of the most striking aspects of shallow flows is the occurrence of two-dimensional coherent structures. We define here the two-dimensional coherent structures as 'connected, large-scale turbulent fluid masses that extend uniformly over the full water depth and contain a phase-correlated vorticity, with the exception of a thin near-bottom boundary layer' (see Jirka and Uijttewaai (2004) and references therein). Jirka (2001) distinguishes three types of generation mechanisms of these two-dimensional coherent structures: (a) topographical forcing, (b) internal transverse shear instabilities and (c) secondary instabilities of base flow.

### Topographical forcing

This first type of generation mechanisms is the strongest kind. Coherent structures are generated because of the presence of obstacles, e.g. groins, islands, etc., in the flow field. One of the most famous examples is the Von Karman vortex street generated beyond an obstacle in the center of the flow. Notice that if we have, for instance, a backward facing step placed in a flow, the occurring coherent structure in the corner just beyond the backward facing step has on itself in principle nothing to do with turbulence. These coherent structures are just part of the solution of the Navier-Stokes equations given the boundary conditions that contain the properties of the backward facing step.

### Internal transverse shear instabilities

A somewhat weaker generation mechanism is defined as internal transverse shear instabilities. Hydrodynamic instabilities gradually grow due to a transverse gradient of the streamwise velocity into large scale coherent structures. The term internal is used to emphasise that there is no external forcing. Coherent structures of this kind are found in, for instance, shallow jets and shallow mixing layers.

### Secondary instabilities of base flow

In shallow flows the length-scale of the large-scale coherent structures are much larger than the water depth. Therefore, as mentioned before, we speak about 2D-turbulence. However, besides these large-scale motions, also small-scale motions (with length-scales smaller than the waterdepth) still occur. These small-scale motions have obviously a three-dimensional character. The third type of generation mechanisms of two-dimensional coherent structures contains coherent structures that are generated by the upcascading of these small-scale three-dimensional turbulent motions to large-scale two-dimensional turbulent motions. In principle, three-dimensional bottom turbulence could give rise to such an upcascading. This generation mechanism is of the weakest kind and experimental evidence is still limited.

## 2.3.2 Very large-scale motions

In the previous paragraphs, we have seen how the turbulent kinetic energy content is distributed over all the length-scales. In the past and until now, the smallest scales received a lot of attention. But recent work of Kim and Adrian (1999), Jimenez (1998) and Del Alamo and Jimenez (2003) shows the existence of energetically significant large-scale structures in turbulent wall flow.

Kim and Adrian (1999), for instance, performed experiments with flow in a pipe with radius  $R$  and a length of about  $280R$  and showed with their experiments that streamwise energetic modes in turbulent pipe flow have wavelengths that range between two and 12-14 pipe radii. Motions of about the latter length are called *very large-scale motions*, while motions of about the former length are just called large-scale motions: motions with characteristic length-scales that are larger than the waterdepth. They found that these very large-scale motions are longest in the lower half of the boundary layer. It is conjectured (see Kim and Adrian (1999) and references therein) that hairpins align coherently in packets that are about  $2R$  long, on average, forming the large-scale motions, and then the packets align coherently to form the very large-scale motions. So they see a strong connection between these very large-scale motions and the mechanism of secondary instabilities of base flow (see previous section), because they conjecture that the very large-scale motions are a consequence of spatial coherence between bulges or between packets of hairpins. Briefly said, some hairpin vortices form vortex packets, some vortex packets form a zone with

uniform (low) momentum, which the very large-scale motions are interrelated with.

As this work has been performed rather recently, many questions remain unanswered, such as: what is the structure of large-scale turbulence in a very wide shallow channel flow? What is the consequence of these supra-depth scales on the energy loss of large-scale horizontal motion? What are the consequences of these supra-depth (i.e. larger than the water depth) scales on separating flow? What is the proper representation of these effects in a depth-averaged time-dependent simulation? In this thesis we want to investigate these questions. In order to obtain data and information which should enable us to answer the questions we like to answer we make use of a Large Eddy Simulation (LES). In the next chapter we shall give an overview of the numerical modelling methods for turbulence and the LES to be used in particular.

# Chapter 3

## Numerical modelling

This chapter provides in some methods for the modelling of turbulent flows. In the first half of this chapter, three important methods for the mathematical modelling of turbulent flows are dealt with. In the second half of this chapter, a model is presented that will be used for calculations to be carried out in the coming chapters.

### 3.1 Turbulence modelling

As mentioned in the previous chapter, turbulence gives rise to problems with regard to finding the proper solution of the governing equations due to its chaotic dynamic character. In order to try to solve these problems three important approaches of numerical modelling of turbulence are common: DNS, RANS and LES. For an elaboration of these methods the book by Sagaut (1998) is recommended. In the following paragraphs a short overview of these three methods is given, together with an extension of the LES-approach for shallow flows at the end.

#### 3.1.1 Direct Numerical Simulation

Direct Numerical Simulation (DNS) aims to resolve the complete Navier-Stokes equations numerically. In order to attain the demanded results, the whole spectrum of occurring length scales must be resolved (see Figure 3.1). This implies a grid size smaller than the smallest occurring length scales, the Kolmogorov scales. The consequence is that the number of grid points which is required becomes very large,:

$$N_g = \left( \frac{\lambda_{large}}{\lambda_{kolm}} \right)^3 = \mathcal{O} \left( Re^{\frac{9}{4}} \right).$$

It is easily seen that for the calculating of flows with high Reynolds numbers, like almost all the flows in civil engineering practice (where  $Re = \mathcal{O}(10^7)$ ), this DNS approach is not suitable as requires high numbers of grid points. This large amount implies small time steps and thus large CPU capacity as well as memory storage are required. On the present day only DNS calculations of low Reynolds number flow are practically feasible.

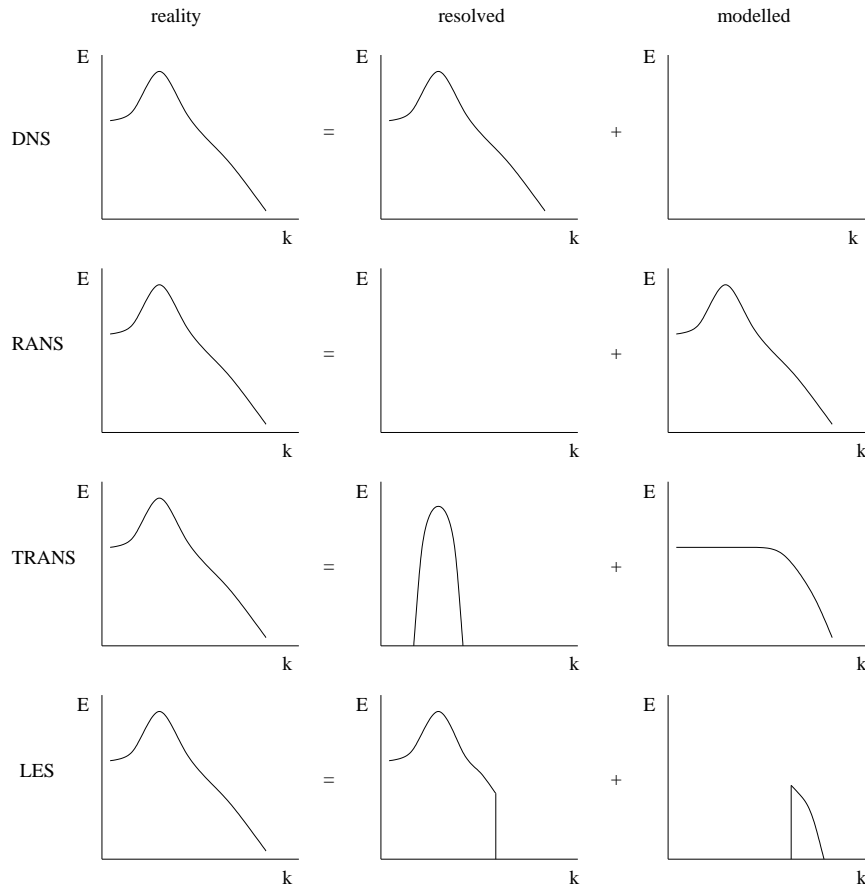


**Figure 3.1:** Decomposition of energy density spectra in a resolved and a modelled part for DNS, RANS, TRANS and LES (adapted from Sagaut (1998)).

### 3.1.2 Reynolds Averaged Numerical Simulation

Another option to represent the motion of the turbulent flow is to use the concept of the Reynolds Averaged Numerical Simulation (RANS, see Figure 3.1). The basic idea of this approach is a decomposition of the flow quantities into a mean and a fluctuation, as done in section 2.1.2, which lead to the Reynolds equations (2.8) in which the effects of turbulent motion appear as the Reynolds stresses. With the Reynolds stresses the closure problem arises and, as seen in paragraph 2.1.2, the remaining problem is then to find a closure for the Reynolds stresses. One approach to do that is by means of an effective eddy viscosity (e.g. an Elder-formulation, an  $k - \epsilon$ -model, etc.).

Mean values are obtained as time averages, ensemble averages or averages in homogeneous directions and may actually vary in time with a time scale much longer than the turbulent time scale. This averaging operation is in practice often equivalent to a time averaging, for instance for the velocity:

$$\bar{u}_i(x_i) = \lim_{T \rightarrow \infty} \frac{1}{T} \int_0^T u_i(x_i, t) dt.$$

Reynolds averaging has the properties:

$$\overline{\overline{u}_i} = \overline{u}_i \quad \text{and} \quad \overline{u_i \overline{u}_j} = \overline{u}_i \overline{u}_j \quad \text{and} \quad \overline{u'_i} = 0.$$

The resulting momentum equation is now that of the steady Navier-Stokes equations. The absence of small scale fluctuations in the solution prevents a fine description of the physical mechanisms, so that this approach is not usable for studies of a fundamental character.

With the RANS-approach exist two approaches: steady RANS and unsteady RANS as the character of the Reynolds-equations, that are to be solved, is steady or unsteady. Unsteady RANS is often called URANS or TRANS (Transient RANS). These approaches are based on the idea to split the turbulent motion in a very-large-scale coherent part and a non-coherent part over the full spectral range (see Figure 3.1), which is accomplished by the following decomposition of the velocity-field:

$$u_i = \tilde{u}_i + u'_i + u''_i. \quad (3.1)$$

The first term is the time average of the exact solution, the second term is interpreted as the contribution of the coherent modes to the flow dynamics, and the third term represents the turbulent fluctuation, again represented by a turbulence model.

The very-large-scale coherent part is to be resolved and the non-coherent part is to be modelled by a turbulence model as used in the RANS-approach.

### 3.1.3 Large Eddy Simulation

An often used approach to get rid of the computational disadvantages of a DNS, is the concept of Large Eddy Simulation. This approach specifically aims at the resolving of the strongly anisotropic and much energy containing large-scale motion, while modelling the isotropic small-scale turbulence (see Figure 3.1).

#### Filtering and subgrid-scale modelling

To get rid of the microstructure of the problem, it is possible to filter the turbulent field (see for instance Nieuwstadt (1998)). Formally we can write the filtering-operation as:

$$\overline{f}(x, y, z) = \int \int \int_V G(\xi - \mathbf{x}) f(\mathbf{x}) d\xi d\eta d\zeta, \quad (3.2)$$

where  $G(\xi - \mathbf{x})$  represents the filter-function. A popular filter is an average over a volume  $V_f = \Delta_f^3$

$$\overline{u}(x, y, z) = \frac{1}{\Delta_f^3} \int \int \int_{V_f} u(\xi, \eta, \zeta) d\xi d\eta d\zeta, \quad (3.3)$$

where the integration volume  $V_f$  is centered around the point  $(x, y, z)$ .  $\Delta_f$  is called the filter-length. By this filter-operation, for which we thus use the overlining sign, all fluctuations with a length-scale smaller than the filter-length  $\Delta_f$  are filtered away. If  $\Delta_f$  is chosen to be the characteristic length-scale of the numerical grid  $\Delta$ , it follows that the filtered velocity-field represents the macrostructure that can be described by the numerical grid. Hence, filtered variables are said to be *resolved* quantities. We can apply the filter-operation to the Navier-Stokes equations with the result:

$$\frac{\partial \overline{u}_i}{\partial x_i} = 0, \quad (3.4)$$

$$\frac{\partial \bar{u}_i}{\partial t} + \bar{u}_j \frac{\partial \bar{u}_i}{\partial x_j} = -\frac{\partial P}{\partial x_i} + \nu \frac{\partial^2 \bar{u}_i}{\partial x_j^2} + \frac{\partial \tau_{ij}^{(s)}}{\partial x_j}, \quad (3.5)$$

where  $P$  represents a modified pressure, defined as:

$$P = \frac{1}{\rho} \bar{p} + \frac{1}{3} \left( \overline{u_i^2} - \bar{u}_i^2 \right).$$

We see that in (3.5) unknown stresses appear, that are formally defined by:

$$\tau_{ij}^{(s)} = -(\overline{u_i u_j} - \bar{u}_i \bar{u}_j) + \frac{1}{3} \left( \overline{u_k^2} - \bar{u}_k^2 \right) \delta_{ij}. \quad (3.6)$$

This term expresses the stresses worked by the microstructure, called *subgrid*, on the large eddies. Hence,  $\tau_{ij}^{(s)}$  are called subgrid stresses. In principle this term is comparable with the Reynolds-stresses  $-\overline{u'_i u'_j}$ . However, we should be aware of the fact that  $\tau_{ij}^{(s)}$  only describes the stresses of the microstructure, while  $-\overline{u'_i u'_j}$  are the stresses on the mean flow as a result of all turbulent scales.

Ergo, we are again confronted with a closing problem as we should prescribe a closing relation for (3.6) in order to be able to solve (3.5). As an example for a closing relation, one can take the Smagorinsky-model:

$$\tau_{ij}^{(s)} = \nu_t \left( \frac{\partial \bar{u}_i}{\partial x_j} + \frac{\partial \bar{u}_j}{\partial x_i} \right) = 2\nu_t \overline{S_{ij}}, \quad (3.7)$$

where  $\overline{S_{ij}}$  is the strain rate tensor and where  $\nu_t$  is the subgrid-eddy-viscosity given by:

$$\nu_t = l_m^2 \left| \frac{\partial \bar{u}_i}{\partial x_j} + \frac{\partial \bar{u}_j}{\partial x_i} \right|. \quad (3.8)$$

It can be shown that the mixing-length  $l_m$  in this case is proportional to the filter-length  $\Delta_f$  with a constant dependent on the type of filtering:

$$C_s = \frac{l_m}{\Delta},$$

which is called the Smagorinsky constant.

### Solid walls

In the vicinity of a solid wall some complications occur, due to the limited resolution and the simplicity of the subgrid model. From a physical point of view the problem is that the flow near a solid wall exhibits substantially different structures than away from it. The dominant scales near the wall are of the order of the boundary layer thickness and hence typically much smaller than in the core of the flow. Moreover, the small scales near a solid wall exhibit substantial anisotropy and the energy transfer mechanisms differ from those away from the wall (see paragraph 2.1.4).

One method to circumvent this, is the use of so-called *wall-functions*. From the wide range of wall models (see Sagaut (1998) and references therein) only the Schumann-approach together with the extending proposed by Grötzbach is presented.

We first recall a few definitions. The boundary layer thickness  $\delta$  is defined as the distance from the wall beyond which the fluid becomes irrotational, and thus where the fluid velocity is equal to the external

velocity (see Figure 2.2), for a fully developed flow at the free surface of the channel or the center of the pipe. The wall shear stress is defined as:

$$\tau_w = \sqrt{\tau_{w,13}^2 + \tau_{w,23}^2}. \quad (3.9)$$

The friction velocity  $u_\tau$  is defined as  $u_\tau = \sqrt{\tau_w}$  and the Reynolds number  $Re_\tau$  as  $Re_\tau = \delta u_\tau / \nu$ . Note the difference between these expressions and the expressions in section 2.1.4:  $\tau_w$  can be interpreted as the wall shear stress  $\tau_0$  per unit of mass integrated over a unit of volume. Therefore, the friction velocities  $u_*$  and  $u_\tau$  are equivalent but in principle not exactly the same. Hence, the wall shear stress  $\tau_w$  has here the dimension  $[L^2/T^2]$ .

Schumann (1975) proposed a wall model for calculating turbulent flow in a channel at finite Reynolds number using a finite volume approach and a staggered grid. As he uses a staggered grid, only the values of the velocity component normal to the wall and of two stress tensor components have to be specified. The boundary conditions proposed are (see Piomelli (2002)):

$$\tau_{w,13}(x, z) = \left( \frac{\bar{u}(x, y, z_1)}{\langle \bar{u}(x, y, z_1) \rangle} \right) \langle \tau_w \rangle, \quad (3.10)$$

$$\bar{w}_w(x, y) = 0, \quad (3.11)$$

$$\tau_{w,23}(x, z) = \nu \left( \frac{\bar{w}(x, y, z_1)}{z_1} \right), \quad (3.12)$$

where  $\langle \cdot \rangle$  denotes either an averaging over a plane parallel to the wall or a long time averaging, and  $z_1$  is the distance of the first point to the wall. The Schumann approach assumes an a priori known mean wall shear stress  $\langle \tau_w \rangle$ , namely a wall shear stress following from the driving pressure gradient. Condition (3.10) assumes the velocity at  $z_1$  to be in phase with the instantaneous wall stress. Condition (3.11) is the impermeability condition. Condition (3.12) is essentially the assumption of a linear velocity profile and a constant-eddy viscosity in the grid cell adjacent to the wall.

Grötzbach extended Schumann's approach by computing the terms in (3.10) differently. Grötzbach uses the actual average of  $\bar{u}(x, y, z_1)$  (taken over the plane  $z = z_1$ ) for  $\langle \bar{u}(x, y, z_1) \rangle$ . Given a plane averaged  $U(z_1)$  he used the logarithmic law to calculate  $\langle \tau_w \rangle$ :

$$u^+(z_1) = \frac{U(z_1)}{u_\tau} = \frac{1}{\kappa} \ln \left( \frac{z_1 u_\tau}{\nu} \right) + B \quad (3.13)$$

where  $B$  is often chosen to be equal to 5.5 and where  $z_1$  is the distance from the wall. Given a  $U(z_1)$  equation (3.13) can be solved for  $u_\tau$  iteratively and applied in equations (3.10) – (3.12). Subsequently the wall shear stress  $\langle \tau_w \rangle$  can be found by  $\tau_w = u_\tau^2$ .

### 3.1.4 Detached Eddy Simulation

We now have three useful options to help us dealing with the numerical modelling of turbulence: DNS, RANS and LES. Each method has its own advantages and disadvantages. It is investigated to what extent it is possible to combine several advantages of the various methods in one method. This investigation has resulted in the so-called Detached Eddy Simulation (DES) approach. A solution is sought for the disadvantage of the LES approach. On the one hand, this approach is very expensive when applied to

complex configurations at high Reynolds numbers because of the resolution required in the boundary layers. An issue that remains even with successful wall-layer modelling. The disadvantage of the RANS approach, on the other hand, is that the statistical models are designed and calibrated on the basis of the mean parameters of thin turbulent shear flows. In DES the aim is to combine the most favourable aspects of the two techniques, i.e., application of RANS models for predicting the attached boundary layers and LES for resolution of time-dependent, three-dimensional large eddies.

Within the DES the LES-method is modified by calculating the eddy-viscosity  $\nu_t$  in a more complicated way: an auxiliary variable  $\tilde{\nu}$  is called into being, which is prescribed by a transport equation for  $\tilde{\nu}$ . For a clear description of the whole model we refer to Piomelli et al. (2003). Essential in this approach is the variable  $\tilde{d} = \min(d, C_{DES}\Delta)$  with  $d$  the distance to the closest wall,  $C_{DES}$  a constant and  $\Delta$  a lengthscale proportional to the local grid spacing. The variable  $\tilde{d}$  serves as a kind of a switch: if  $d \ll \Delta$  the model acts like a RANS, if  $d \gg \Delta$  the model acts as the modified LES-model. Ergo, the separation region near a wall is described by a RANS-approximation. Within the transition region the model smoothly evolves from a RANS-like model to an LES-like model. We refer to Squires (2004) for applications of the DES-approach.

### 3.1.5 Depth-Averaged Large Eddy Simulation

Several attempts are done to represent the three-dimensional effects in a two-dimensional simulation. In order to deal with shallow flows with inclusion of their quasi-2D turbulence several variants on the LES-approach have been developed in the past. These variants are focussed on solving the filtered Navier-Stokes equations after *depth-averaging*. Let  $\bar{u}_i$  be a velocity filtered using a certain filter, then we write the filtered continuity equation and rewrite the equations (3.5):

$$\frac{\partial \bar{u}_i}{\partial x_i} = 0, \quad (3.14)$$

$$\frac{\partial \bar{u}_i}{\partial t} + \frac{\partial}{\partial x_j} (\bar{u}_i \bar{u}_j) = -\frac{1}{\rho} \frac{\partial \bar{p}}{\partial x_i} + \frac{\partial}{\partial x_j} (2\nu \bar{S}_{ij} - \tau_{ij}), \quad (3.15)$$

with  $i, j = 1, 2, 3$  and where  $\tau_{ij} = \overline{u_i u_j} - \bar{u}_i \bar{u}_j$ . Applying a depth-averaging operator  $\widetilde{(\cdot)}$  (thus  $\widetilde{\varphi} = \frac{1}{h} \int_0^h \varphi dz$ ) together with the hydrostatic pressure assumption ( $p = \rho gh$ ) we obtain the depth-averaged filtered Navier-Stokes equations:

$$\frac{\partial \bar{\xi}}{\partial t} + \frac{\partial h \widetilde{u}_i}{\partial x_i} = 0, \quad (3.16)$$

$$\frac{\partial h \widetilde{u}_i}{\partial t} + \frac{\partial}{\partial x_j} (h \widetilde{u}_i \widetilde{u}_j) = -gh \frac{\partial \bar{\xi}}{\partial x_i} + \frac{\partial}{\partial x_j} (h (2\nu \widetilde{S}_{ij} - T_{ij})) - \frac{\bar{\tau}_{w_i}}{\rho}, \quad (3.17)$$

with  $i, j = 1, 2$  and where  $h$ ,  $\xi$  and  $\tau_w$  represent the water depth, the elevation of the water surface and the shear stress at the bottom respectively. Depth integration introduces dispersive stresses

$$D_{ij}(\mathbf{u}) = \frac{1}{h} \int_0^h (u_i - \widetilde{u}_i) (u_j - \widetilde{u}_j) dz = \widetilde{u_i u_j} - \widetilde{u}_i \widetilde{u}_j. \quad (3.18)$$

In (3.15)  $\tau_{ij}$  represents the subgrid-scale stresses and in (3.17)  $T_{ij}$  represents the total stress which results from combining the depth integration and the filtering:

$$T_{ij}(\mathbf{u}) = \widetilde{u_i u_j} - \widetilde{u}_i \widetilde{u}_j. \quad (3.19)$$

The dispersive stresses are related to  $T_{ij}(\mathbf{u})$  by

$$T_{ij}(\mathbf{u}) = D_{ij}(\bar{\mathbf{u}}) + \widetilde{\tau}_{ij}(\mathbf{u}). \quad (3.20)$$

Hence it is clear that there are three unknowns that need to be modelled. Firstly, the subgrid-scale stresses  $\tau_{ij}$  which can for instance be modelled using the Smagorinsky model. Secondly, the quantity  $T_{ij}$  and thirdly the bottom friction  $\tau_w$  which is usually modelled using a quadratic friction law.

One of the models that can be used to model  $T_{ij}$  is the method as presented by Hinterberger *et al.* (2004). This model proposes to model  $T_{ij}$  as follows:

$$\frac{\partial}{\partial x_j} T_{ij} \approx \frac{\partial}{\partial x_j} \left( -2\nu_t \widetilde{S}_{ij} \right) - F_i, \quad (3.21)$$

where  $F_i$  is a random force using a stochastic back scatter model, needed to model the energy transfer from the unresolved 3D turbulence to the resolved 2D turbulence. For the eddy viscosity a simple model based on the local friction velocity and the water depth can be used,  $\nu_t = c_h h u_\tau$ . Expression (3.21) together with the model for  $F_i$  and  $\nu_t$  are put in equation (3.17) that can now be solved numerically.

The use of the depth-averaged equations (3.16) and (3.17) to model 2D-turbulence is called Horizontal Large Eddy Simulation (HLES) or Very Large Eddy Simulation (VLES). Obviously in a LES we only need to model the 3D subgrid-scale stresses to account for the smallest non-resolved scales whereas a HLES we have to account for all 3D-turbulent motion.

## 3.2 Model description

In this thesis, turbulent flows are simulated by using a Large Eddy Simulation (LES). Therefore an extension of the LES-code developed by B.J. Boersma (Laboratory for Aero- and Hydrodynamics, Delft University of Technology) is used. In this section, this code is described by presenting the structure of this code.

The model solves the filtered Navier-Stokes equations (3.4) and (3.5) by means of a finite volume technique, in this case the central-differencing-scheme, which is second-order accurate, on a staggered grid and uses the Smagorinsky closing relations (3.7) and (3.8) to model the subgrid-scale stresses, together with a rigid lid at the free surface. The viscosity is then given by the sum of the molecular viscosity  $\nu_{molc}$  and the eddy viscosity  $\nu_t$ . For the temporal discretisation of the equations the second-order accurate Adams-Bashforth-scheme is used. The connection of the velocity-terms with the pressure-term is made by the so-called pressure-correction method.

### 3.2.1 Spatial discretisation

#### Domain

Because LES-calculations are computationally expensive, the LES-code is parallelised by dividing the domain in several parts (see Figure 3.2). Each part is assigned to one processor.

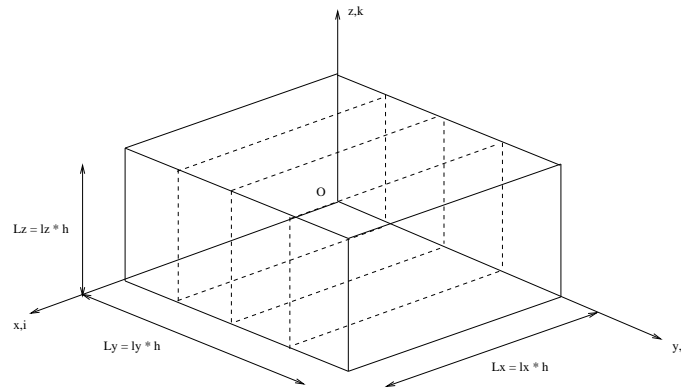


**Figure 3.2:** Domain definitions with parallelisation.

The distances  $L_x$ ,  $L_y$  and  $L_z$  are made dimensionless using the channel depth  $D$  which results in the dimensionless lengths  $l_x$ ,  $l_y$  and  $l_z$ . Characteristic for the program is that the length in  $z$ -direction is set on  $l_z = 1$ . The velocities are made dimensionless by the friction velocity  $u_\tau$ .

### Staggered grid

Let the domain now be discretised by a uniform grid consisting of orthogonal cells. The oldest and most straightforward approach to discretising the Navier-Stokes equations in space is the method proposed in 1965 by Harlow and Welch.

Grid points for different unknowns are staggered with respect to each other. The pressure resides in the cell centers, whereas the cell face centers contain the normal velocity components (see Figure 3.3).

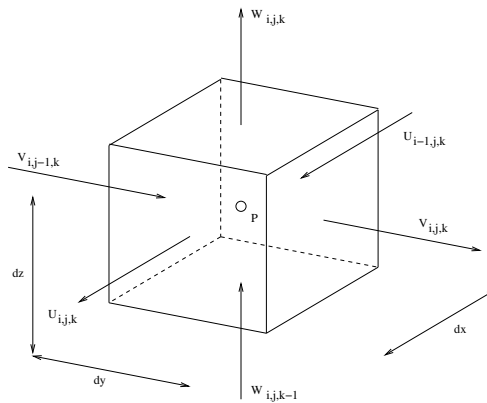


**Figure 3.3:** A grid cell of the staggered grid.

Now having introduced the staggered grid on the defined domain, we can discretise the complete Navier-Stokes equations. We do not give the full discretisation of these equations but restrict ourselves to give the discretisation of the continuity equation and of three examples: an advection term, a pressure term and a diffusion term.

The discretised continuity equation reads:

$$\operatorname{div}(u, v, w) = \frac{1}{dx} (U_{i,j,k} - U_{i-1,j,k}) + \frac{1}{dy} (V_{i,j,k} - V_{i,j-1,k}) + \frac{1}{dz} (W_{i,j,k} - W_{i,j,k-1}) \quad (3.22)$$

An example of an advection term:

$$\frac{\partial uv}{\partial y} = \frac{1}{4} \frac{1}{dy} ([ (U_{i,j,k} + U_{i,j+1,k}) (V_{i,j,k} + V_{i+1,j,k}) ] - [ (U_{i,j,k} + U_{i,j-1,k}) (V_{i,j-1,k} + V_{i+1,j-1,k}) ]) \quad (3.23)$$

An example of a pressure term:

$$\frac{\partial p}{\partial x} = \frac{1}{dx} (P_{i+1,j,k} - P_{i,j,k}) \quad (3.24)$$

An example of a diffusion term:

$$\frac{\partial}{\partial x} \left[ 2\nu \frac{\partial u}{\partial x} \right] = \frac{1}{dx} \left[ 2\nu \left( \frac{U_{i+1,j,k} - U_{i,j,k}}{dx} \right) - 2\nu \left( \frac{U_{i,j,k} - U_{i-1,j,k}}{dx} \right) \right] \quad (3.25)$$

where  $\nu = \nu(x, y, z)$  is a function of the spatial coordinates  $(x, y, z)$ .

For convenience we rewrite the discretised equivalents of the Navier-Stokes equations in vector-notation as:

$$D\mathbf{u} = 0 \quad (3.26)$$

$$\frac{d\mathbf{u}}{dt} + N(\mathbf{u}) + Gp = 0 \quad (3.27)$$

Here  $N$  is a nonlinear algebraic operator arising from the discretisation of the inertia and viscous terms,  $G$  is a linear algebraic operator representing the discretisation of the pressure gradient,  $D$  is a linear algebraic operator representing the discretisation of the divergence operator in the continuity equation. System (3.26), (3.27) is called a *differential-algebraic system*.

$N(\mathbf{u})$  in (3.27) can be split up in a nonlinear inertia part  $C$  and a linear viscous part  $B$ , as follows:

$$N(\mathbf{u}) = C(\mathbf{u}) + B\mathbf{u} \quad (3.28)$$

### 3.2.2 Temporal discretisation

Having discretised the spatial part of the Navier-Stokes equations, we only have to discretise the temporal part of the equations.

#### Adams-Bashforth

For temporal discretisation of system (3.26), (3.27) many methods exist. Here we restrict ourselves by only giving the so-called generalised trapezoidal scheme, applied to equations (3.26) and (3.27):

$$D\mathbf{u}^{n+1} = 0 \quad (3.29)$$

$$\frac{1}{\Delta t} (\mathbf{u}^{n+1} - \mathbf{u}^n) + \theta N(\mathbf{u}^{n+1}) + (1 - \theta) N(\mathbf{u}^n) + Gp^{n+1} = 0 \quad (3.30)$$

where  $n + 1$  is the newest time-step. If  $\theta = 0$  we have the *Euler-explicit* scheme, if  $\theta = 1$  we have the *Euler-implicit* scheme and if  $\theta = 1/2$  we have the *Crank-Nicholson* scheme. The cases  $\theta = 1/2$  and  $\theta = 1$  are not really candidates to be implemented in the LES-code for these schemes are implicit and therefore computationally expensive. Actually, the case  $\theta = 0$  is not a candidate either for the Euler-explicit scheme is only first order accurate in time and very unstable. Therefore, an extension of the Euler-explicit scheme can be introduced: consider a system of ordinary differential equations

$$\frac{df}{dt} = g(f, t)$$

then a *two-step method* can be proposed:

$$\frac{1}{\Delta t} (f^{n+1} - f^n) = ag(f^n, t^n) + bg(f^{n-1}, t^{n-1}) \quad (3.31)$$

The combination  $a = 1$ ,  $b = 0$  gives the Euler-explicit scheme, the combination  $a = 3/2$ ,  $b = -1/2$  gives the *Adams-Bashforth* scheme. The latter scheme has been implemented in the LES-code for it is explicit (and thus cheap) and second-order accurate in time. Now the equations (3.26) and (3.27) to be solved become (combined with (3.28)):

$$D\mathbf{u}^{n+1} = 0 \quad (3.32)$$

$$\frac{1}{\Delta t} (\mathbf{u}^{n+1} - \mathbf{u}^n) + \frac{3}{2} (C(\mathbf{u}^n) - B\mathbf{u}^n) - \frac{1}{2} (C(\mathbf{u}^{n-1}) - B\mathbf{u}^{n-1}) + Gp^{n+1} = 0 \quad (3.33)$$

### Pressure-correction method

The system (3.32), (3.33) is a coupled system for  $\mathbf{u}^{n+1}$  and  $p^{n+1}$ . Computing time is reduced if  $\mathbf{u}^{n+1}$  and  $p^{n+1}$  can be solved for separately. To this end the following method has been devised, which is the method of choice for nonstationary problems: the *pressure-correction* method. This method is as follows.

First rewrite equation (3.33) into:

$$\mathbf{u}^{n+1} + \Delta t Gp^{n+1} = \mathbf{u}^* = \mathbf{u}^n - \Delta t \left[ \frac{3}{2} (C(\mathbf{u}^n) - B\mathbf{u}^n) - \frac{1}{2} (C(\mathbf{u}^{n-1}) - B\mathbf{u}^{n-1}) \right] \quad (3.34)$$

then take the divergence of (3.34) (equivalent to applying the operator  $D$ ):

$$DGp^{n+1} = \frac{1}{\Delta t} D\mathbf{u}^* \quad (3.35)$$

Remembering that  $\text{divgrad}(DG)$  equals the Laplacian, we see that (3.35) looks very much like a discrete Poisson equation; it is frequently called the pressure Poisson equation. To solve this Poisson equation a direct solver of the Poisson equation is included in the LES-code. When the new solution for the pressure is obtained,  $\mathbf{u}^{n+1}$  can be solved by:

$$\mathbf{u}^{n+1} = \mathbf{u}^* - \Delta t Gp^{n+1} \quad (3.36)$$

Each time step this pressure-correction algorithm is evaluated.

### 3.2.3 Boundary conditions

When solving a differential equation one always needs conditions on the boundaries of the considered domain. The domain has already been defined in Figure 3.2. Here we see that for all the six limiting planes proper boundary conditions must be prescribed. Given a certain boundary value problem for a certain  $\varphi(x)$ , a boundary condition at a certain plane  $x = p$  can be prescribed in two different ways:

$$\varphi(p) = a \quad \text{and} \quad \frac{d\varphi(p)}{dx} = b$$

The first type is called a *Dirichlet* condition and the second type is called a *Neumann* condition. In this section we give appropriate specifications for the boundaries in our LES.

Let  $\Omega_{ijk}$  be the computational domain with  $i = 1, \dots, I$ ,  $j = 1, \dots, J$  and  $k = 1, \dots, K$  (defined in the grid-cell center). In the numerical model, the grid points in  $x, y, z$ -direction vary from 1 to  $\text{imax}, \text{jmax}, \text{kmax}$  respectively. Hence, a grid point  $(0, j, k)$  or  $(\text{imax}+1, j, k)$ , for example, is called a virtual grid point: virtual grid points are grid points just outside the domain that are important for prescribing boundary conditions.

Also important is the fact that in the program we use a dimensionless pressure-gradient equal to unity as driving force that has to be in an equilibrium state with the shear-stress at the bottom. Hence we state:

$$\tau = \int_0^h \frac{\partial p}{\partial x} dz = \rho u_*^2 = \tau_0 \quad (3.37)$$

and therefore

$$\frac{\partial p}{\partial x} h = \rho u_*^2 = u_\tau^2 \quad (3.38)$$

If we also use  $h$  as a scaling parameter (thus  $h = 1$ ), then it follows that the friction velocity  $u_\tau$  is equal to 1 which makes it possible to scale velocities, in general, with  $u_\tau$ .

#### Inflow conditions and outflow conditions

If we want to simulate a channel flow with the main flow in  $x$ -direction we need, on the given domain, an inflow condition for the plane  $x = 0$  and an outflow condition for  $x = L_x$ . An often used boundary condition for inflow and outflow boundaries are periodic boundary conditions. With  $\Omega_{ijk}$  representing the computational domain, let  $x = 0$  be the inflow boundary, then  $\Omega_{1jk}$  is at the inflow boundary and let  $x = L_x$  be the outflow boundary, then  $\Omega_{Ijk}$  is at the outflow boundary. In this case the periodic boundary conditions for the streamwise velocities read:

$$u_{0,j,k} = u_{I,j,k} \quad \text{and} \quad u_{I+1,j,k} = u_{1,j,k},$$

with conditions for the transverse and wall-normal velocities similarly. These expressions say that what is going out, is going in again. The same concept is followed when prescribing boundary conditions for the planes  $y = 0$  and  $y = L_y$ .

#### Free surface conditions

When simulating a channel flow, the boundary  $z = L_z$  is the free surface of the flow and  $\Omega_{ijK}$  is at this boundary. Typical for free surfaces are the following *free-slip* conditions (see Figure 3.4 for the definition).

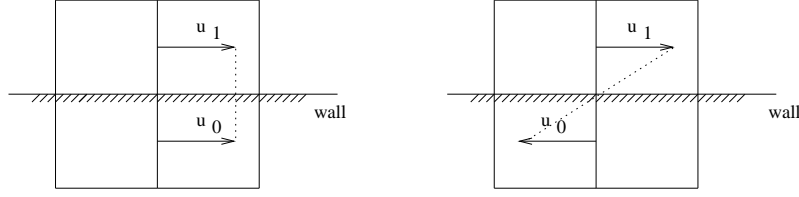


**Figure 3.4:** The principle of a free-slip (left) and a no-slip boundary-condition. The use of a free-slip boundary results in a zero-shear-stress (dotted line), the use of a no-slip boundary results in a non-zero shear-stress. The figure includes four grid-cells and the wall (boundary), the velocities are defined on the boundaries of the grid-cell (see Figure 3.3).

We have  $w_{i,j,K+1/2} = 0$ , so that no discrete equation is required for  $w_{i,j,K+1/2}$ . According to Figure 3.4, we put  $\frac{\partial u}{\partial z} = 0$  and  $\frac{\partial v}{\partial z} = 0$ , resulting in:

$$u_{i+1/2,j,K+1} = u_{i+1/2,j,K} \quad \text{and} \quad v_{i,j+1/2,K+1} = v_{i,j+1/2,K},$$

which are Neumann conditions that tell us that the tangential stresses are zero.

### Bottom conditions

The remaining boundary that needs a prescribed condition is the bottom, i.e. the plane  $z = 0$ . As the bottom acts as a solid wall, in principle *no-slip* conditions should be prescribed. But as we have seen in section 3.1.3, some problems occur when dealing with a sufficient resolution near a no-slip wall. Let  $z = 0$  be the bottom and  $\Omega_{ij0}$  be at the bottom, where  $w_{i,j,1/2} = 0$ , the free-slip conditions read:

$$u_{i+1/2,j,0} = u_{i+1/2,j,1} \quad \text{and} \quad v_{i,j+1/2,0} = v_{i,j+1/2,1},$$

which are the Neumann conditions that prescribe a velocity gradient equal to zero. The no-slip conditions would be the same, except for a factor  $-1$ . Physically, no-slip conditions represent  $\tau = \rho\nu \frac{\partial u}{\partial z}$ .

In order to prescribe the appropriate shear-stress at the wall we modify the free-slip conditions by (3.10) – (3.12) using (3.13). Now these expressions (3.10) – (3.13) can be put into the light of equation (3.34): each time step the momentum contributions

$$N(\mathbf{u}^n) = C(\mathbf{u}^n) - B\mathbf{u}^n \quad \text{and} \quad N(\mathbf{u}^{n-1}) = C(\mathbf{u}^{n-1}) - B\mathbf{u}^{n-1}$$

must be calculated. To account for the influence of the wall an extra momentum source is added to this contributions, but only to the equations to be solved in the first grid point from the wall. Following (3.10) this contribution must, for instance for  $U$ , be equal to

$$\frac{1}{dz} \frac{U_{i,j,1}}{\bar{U}_{i,j,1}} \langle \tau_w \rangle$$

where  $\bar{U}_{i,j,1}$  is the average of the velocities  $U$  over the plane  $(i, j, 1)$  and  $\langle \tau_w \rangle$  as in (3.10) calculated from the log-law (3.13). This principle is described in detail in Appendix B.

As the free-slip-character of the free-slip conditions at the wall now perishes after being modified by Schumann's wall function we call the new assembled boundary conditions for the wall *partial-slip* conditions.

Since the domain in  $y$ -direction is divided into  $n$  parts, we should be careful with dealing with the  $n$  subdomains. Hence, each subdomain provides boundary conditions for the neighbouring subdomains. Thus, the communication between the  $n$  parts takes place via the boundaries of each subdomain.

### 3.2.4 Initial conditions

Besides defined boundary conditions also initial conditions must be prescribed. Obviously, the initial conditions to be imposed, depend on the problem to be calculated. For a free-surface channel flow, the following is proposed. We define the velocities  $v$  and  $w$  to be zero in each gridpoint. For the streamwise velocities  $u$  we prescribe a power-law that is quite suitable for turbulent free-surface flow:

$$u(z) = u_{max} \left( \frac{z}{D} \right)^n \quad (3.39)$$

with  $n = \frac{1}{7}$  and  $u_{max} = 20u_\tau$ . To the velocity profiles of the three velocities  $u$ ,  $v$  and  $w$  is some noise added to give the initial velocity field a somewhat random character. Care should be taken of sufficient asymmetry with respect to parallel domains. After having started the simulation, a certain time will be needed to reach steady state.



# Chapter 4

## Channel flow

The preceding chapter showed the approaches of how to model turbulence and described the LES-code that is going to be used for numerical experiments. In this chapter the first numerical experiment is carried out: three-dimensional Large Eddy Simulations are performed at three different Reynolds-numbers and the results of the calculations are analysed with the focus on spectral distributions. The results of these simulations are to be used for a depth-averaged unsteady RANS method, as will be presented in the next chapter.

### 4.1 Background and objective

As mentioned in the first chapter, we are interested in the structure and characteristics of large-scale coherent structures in shallow flows. An important quantity that tells a lot about this structure and characteristics is the distribution of turbulent kinetic energy in wavenumber-space, because this distribution tells us on which length-scales most of the turbulent kinetic energy is contained. The aim of this numerical experiment is to look whether or not there is a dependency perceptible of the 1D- and 2D-energy density spectra (based on depth-averaged velocity maps) on the Reynolds-number and, more general, to investigate the (spectral) structure of the turbulence occurring in the flow. Hence, three Large Eddy Simulations are carried out on a channel flow at three different Reynolds-numbers.

### 4.2 Numerical setup

Most aspects of the Large Eddy Simulation on channel flow have already been described in the previous chapter. Here we can provide more details on the flow geometry. For the computational domain we use (see also Figure 4.1):

$L_x$	$L_y$	$L_z$	$N_x$	$N_y$	$N_z$
$80D$	$80D$	$D$	1024	1024	16

**Table 4.1:** Lengths of the domain with the number of gridpoints in each direction.

Remembering that all velocities are made dimensionless by the friction velocity  $u_\tau$  and all lengths are made

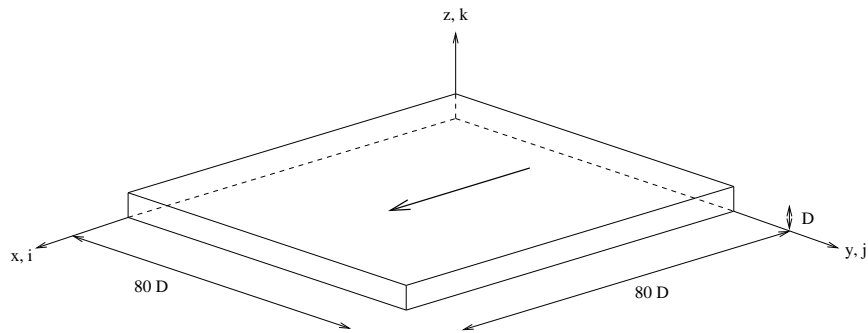


**Figure 4.1:** Computational domain.

dimensionless by the depth  $D$ , both chosen equal to unity, the flow is characterised by the Reynolds-number  $Re_\tau = \frac{u_\tau D}{\nu}$ . For the Smagorinsky constant  $C_s$  the value 0.065 is used.

Three cases at different Reynolds-numbers are carried out:

<i>Case</i>	$Re_\tau$
A	395
B	590
C	1000

**Table 4.2:** Three cases at different Reynolds-numbers.

Cases A and B are chosen for the option of comparison with the data of DNS-results from Moser, Kim and Mansour (1999) (MKM henceforth). Case C is chosen for this Reynolds-number tends to be more realistic in civil engineering applications.

For the description of the boundary conditions and initial conditions we refer to the previous chapter. But a difference between the MKM-simulations and the simulations used here is the fact that MKM uses a no-slip rigid lid upper boundary condition when simulating a closed channel, where here we use a free-slip rigid lid upper boundary condition. Comparison is possible when considering the open channel with only half the closed channel. The initial conditions are given a slight random perturbation to make the generation of coherent structures possible.

## 4.3 Results

As we have special interest in the depth-averaged statistics of the flow, the results are split up into a part with statistics obtained without having applied any depth-averaging operation and into a part with statistics obtained after depth-averaging the velocity-field.

### 4.3.1 Validation

For the first two cases, where  $Re_\tau$  equals 395 and 590 respectively, comparison with the MKM-data is possible. Results for the mean streamwise velocity profile and the turbulence intensities are, for these two Reynolds-numbers, shown in Figure 4.2.

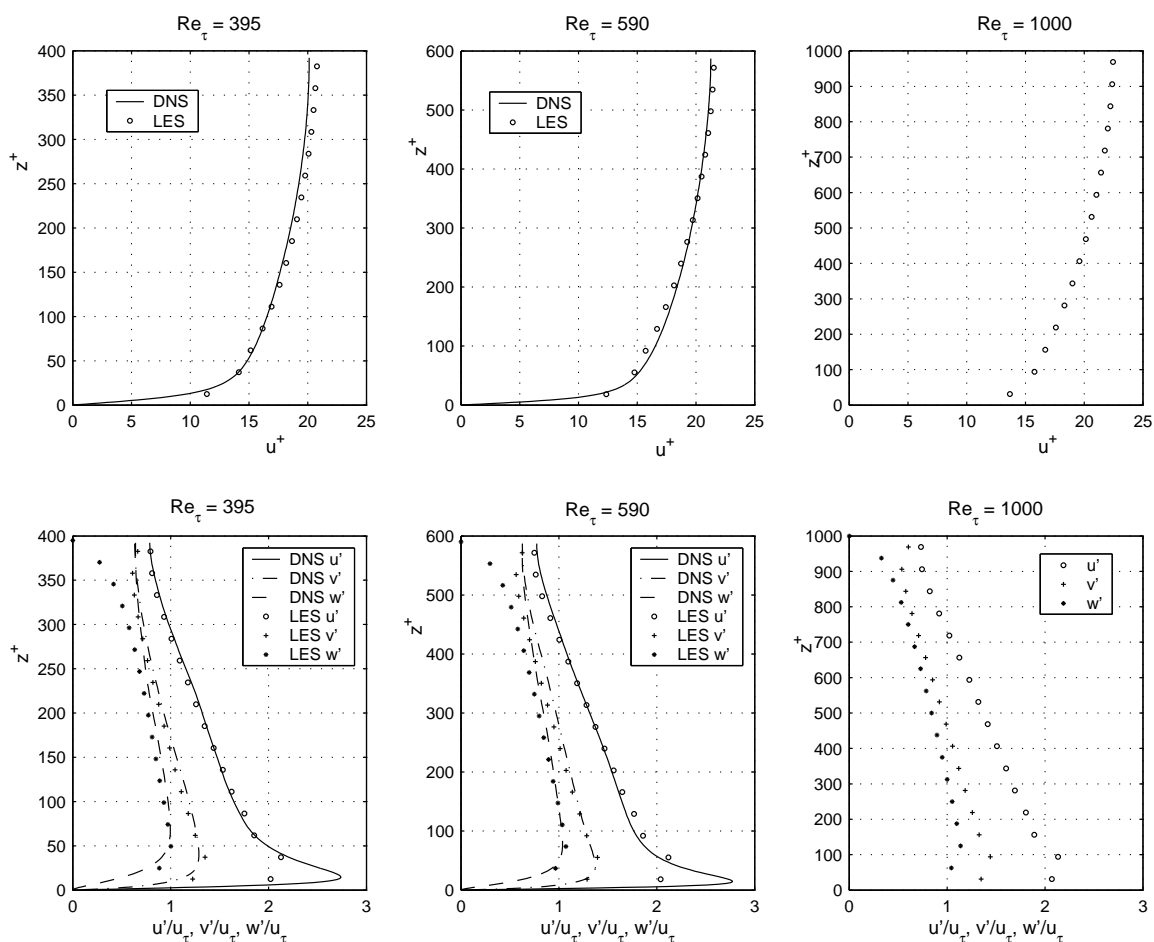


**Figure 4.2:** Streamwise velocity profiles (upper plots) and turbulence intensities profiles (root-mean-square fluctuations)(lower plots) for  $Re_\tau = 395$  (left plots),  $Re_\tau = 590$  (middle plots) and  $Re_\tau = 1000$  (right plots).

From Figure 4.2 it is clear that the difference between the LES and the DNS are quite small despite the coarse resolution near the bottom. An eye-catching difference are the deviations in the vertical turbulence intensities near the free surface. These are a result of the rigid-lid assumption at the free surface, whereas at the DNS computation this line represents the centerline, where obviously vertical turbulence intensities are possible. The turbulence intensities profiles show anisotropy over the whole depth which is at its strongest near the bottom.

Having seen that the velocity profile and turbulence intensities profiles as resulted from the LES are in fairly good agreement with the DNS-results, we can focus on the spectral distributions of the turbulent kinetic energy, both in the one-dimensional case and the two-dimensional case.

Energy density spectra are given in Figure 4.3. Firstly, it should be stated that the LES-results and the DNS-results both span a different range of wavenumbers, which is due to the different domains and discretisations. As for reasons with regard to the duration of the computation, the DNS mainly resolves the large-wavenumber part of the spectra, whereas the LES models this part while focussing on the small-

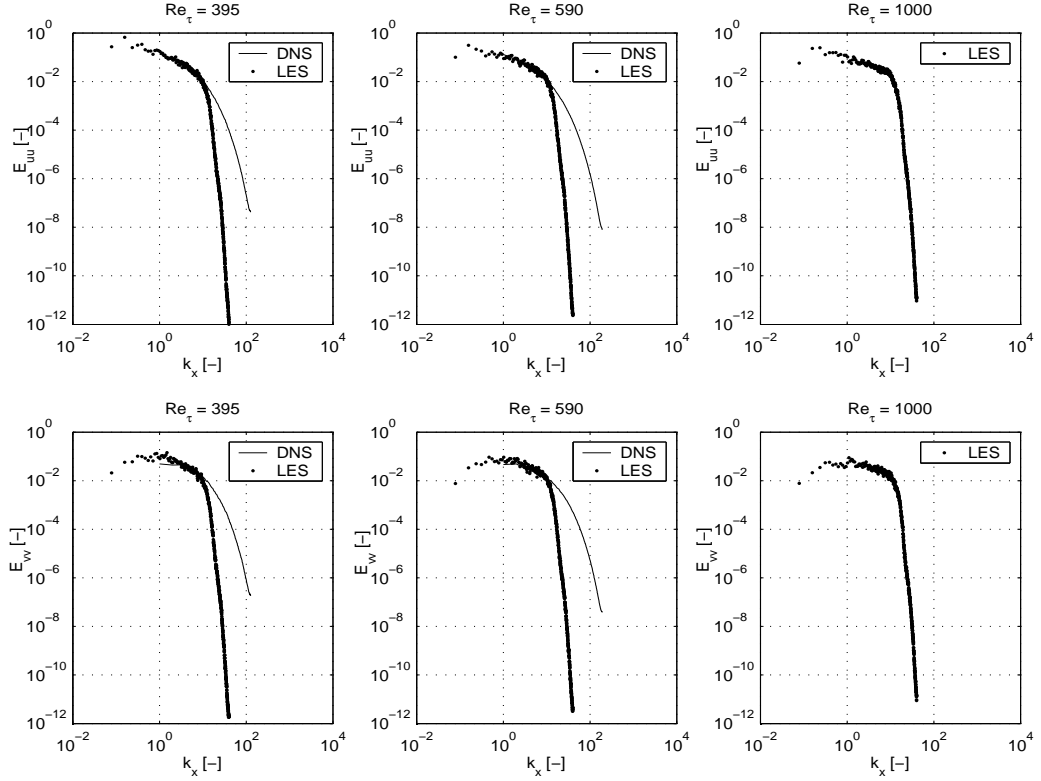


**Figure 4.3:** Energy density spectra for the three Reynolds-numbers, from the LES, compared with the MKM-data. Upper plots show spectra of streamwise velocity fluctuations, lower plots show the spectra of transverse velocity fluctuations, for  $z = D$ .

wavenumber part of the spectra. On the one hand, the spectra are limited by the small wavenumber associated with the size of domain. On the other hand, the spectra are limited by the large wavenumber, that has at least to be smaller than the Nyquist wavenumber related to the gridsize. Hence, the spectra are defined on  $k_x \in \left[ \frac{2\pi}{L_x}, \frac{2\pi}{2dx} \right]$ .

When comparing the DNS-spectra (lines) and LES-spectra (dots) at  $z = D$ , in Figure 4.3, a good agreement of both the results is noticeable. Of course, only in the non-small scale part. These spectra preeminently show how useful Large Eddy Simulations are for the representation of large-scale motions in turbulent flows: fair agreement with Direct Numerical Simulation is possible, and moreover, LES is able to deal with larger domains in order to get information about large-scale motion. Only the small-scale part is, of course, poorly represented, but that is not a problem for our purpose.

Regarding Figure 4.2 and Figure 4.3, the agreement with the DNS is concluded to be sufficient, and therefore the resolution and the wall function used in the LES are concluded to be suitable for the determination of the large-scale depth-averaged motion.

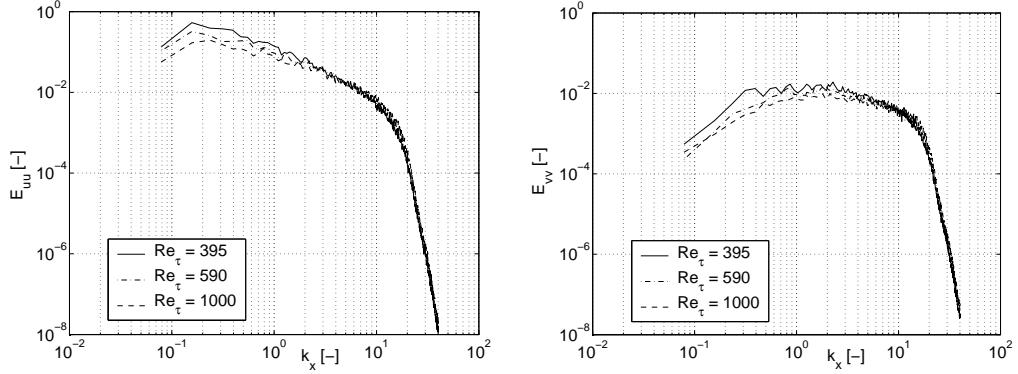


**Figure 4.4:** One-dimensional energy density spectra of the depth-averaged streamwise (plot on the left) and transverse (plot on the right) velocity fluctuations in the  $k_x$ -space .

### 4.3.2 Depth-averaged statistics

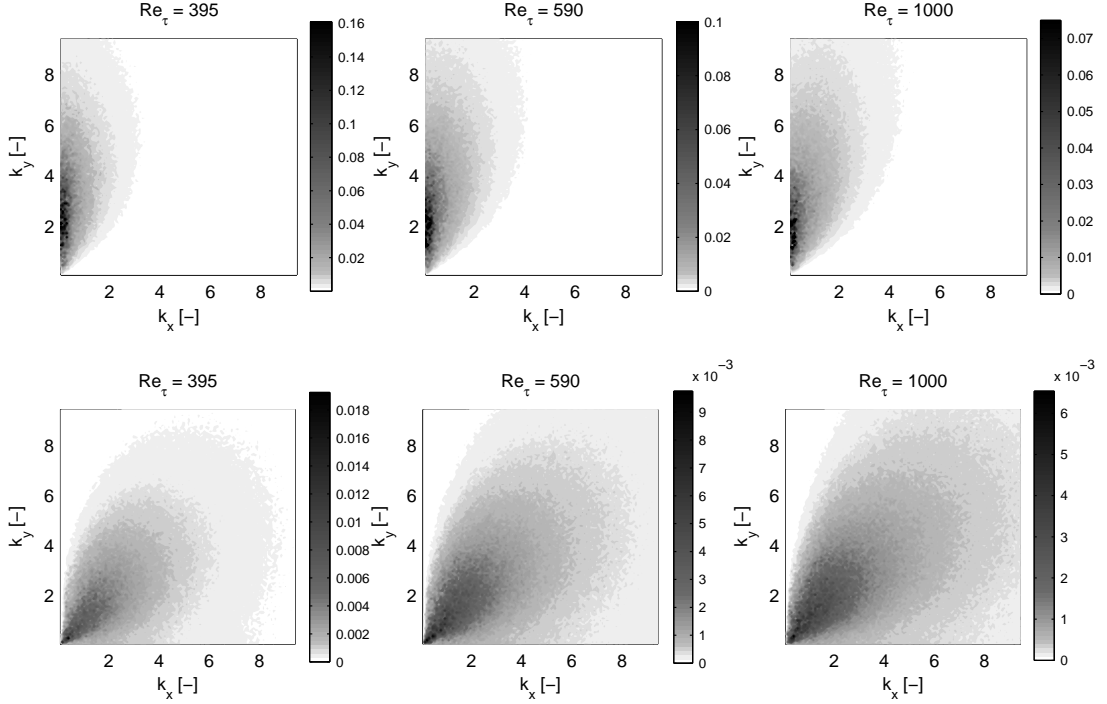
Now when having compared the LES-results and the DNS-results as well as having concluded that both the results are in agreement to an acceptable extent, the depth-averaged statistics can be collected, in particular the 1D- and 2D-energy density spectra. In order to determine these spectra, instantaneous velocity fluctuation maps are first averaged over the depth. The spectra are obtained from 100 statistically independent velocity maps, which is realised by taking 100 velocity maps on mutually equal distances in time. This time-interval should be larger than the time-scale of coherent structures in the flow. This requires a sufficiently small correlation between two randomly chosen velocity maps. Without going into detail, the velocity maps are checked on their mutual correlation, which resulted in sufficiently small correlation-coefficients. If the time-distance is larger than the time-scale of the motions, as in our case (as can be concluded by the fact that the correlation-coefficients are small), the ergoden-theorem says that an averaging operation in time equals an ensemble-averaging operation.

Figure 4.4 and Figure 4.5 give the 1D- and 2D-energy density spectra respectively. As doing an LES, we focus on the large eddies of the flow, while ignoring the small scales. As seen in Figure 4.3, results of length-scales with  $k_x > 10$  are not useful.

Figure 4.4 shows that the three energy-density spectra (both for  $E_{uu}$  and  $E_{vv}$ ) indicate equal energy-densities for each Reynolds-number at  $k_x \approx 7$ . At the large-scale part of the spectra, the spectra start to vary for the three Reynolds-numbers: indicatively, it can be said that the larger the Reynolds-number, the smaller is the energy-density at supra-depth length-scales.

For this supra-depth length-scale part of the  $E_{uu}$ -spectra, the shape of the curve is almost linear with slope varying from about  $-1$  to  $-1.5$ . The  $E_{vv}$ -spectra are almost flat in the supra-depth length-scale part. Both the  $E_{uu}$ - and  $E_{vv}$ -spectra show the Reynolds-dependency on the large scales.

And what about the 2D-energy-density spectra? Figure 4.5 show the distributions of turbulent kinetic energy as a function of  $k_x$  and  $k_y$ . Our first observation is the fact that the  $E_{uu}$ -spectra are pressed towards the  $k_y$ -axis, while the  $E_{vv}$ -spectra seems to be symmetric along the ridge  $k_x = k_y$ . This difference can be explained by the fact that the pattern of the streamwise fluctuations are elongated in streamwise direction, while the transverse fluctuations are more isotropic. Our second observation is that the shape of the spectra is growing with increasing Reynolds-number, while the occurring maxima per spectrum is



**Figure 4.5:** Two-dimensional energy density spectra of the depth-averaged streamwise velocity fluctuations  $E_{uu}$  (upper plots) and the depth-averaged transverse velocity fluctuations  $E_{vv}$  (lower plots) for the three Reynolds-numbers.

decreasing with increasing Reynolds-number.

When introducing

$$k = \sqrt{k_x^2 + k_y^2},$$

we can make Figure 4.5 more manageable by evaluating the integrals

$$E_{uu}^i = \iint E_{uu} k dk d\varphi \quad \text{and} \quad E_{vv}^i = \iint E_{vv} k dk d\varphi, \quad (4.1)$$

where the superscript  $i$  indicates that the quantities concern integrated energy-density spectra. With equation (4.1) we integrate the  $E_{uu}$ - and  $E_{vv}$ -spectra over circular shells, i.e. we try to make spectra containing all information from the 2D-spectra by taking the sum of the contributions of the spectra along a circular shell for an arbitrary radius  $k$ , just as proposed in the first chapter. The result is shown in Figure 4.6.

Figure 4.6 also shows that the amount of turbulent kinetic energy of the very-large-scale part is decreasing with increasing Reynolds-number. The integrated spectra show peak-values at  $k \approx \pi$ , for all the three Reynolds-numbers. The location of these peak-values are consistent with the locations of the peak-values in Figure 4.5. When we are aware of the fact that  $k = 2\pi$  corresponds to coherent structures with wavelength equal to the water-depth, we can conclude that the most energy-containing coherent structures in the depth-averaged velocity-maps are of the order of the water-depth. After all, a coherent

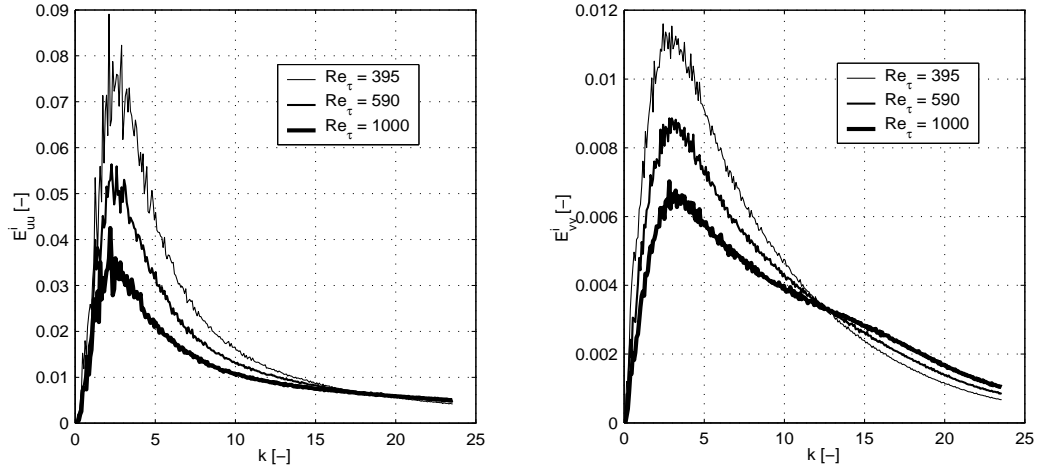


**Figure 4.6:** Integrated  $E_{uu}$ -spectra contributions (on the left) and  $E_{vv}$ -spectra contributions (on the right), for three Reynolds-numbers.

structure with length-scale equal to the water-depth, can be modelled as having a wavelength equal to twice the water-depth.

A remarkable observation is, that the three curves intersect at a single point: at  $k \approx 17$  in the  $E_{uu}^i$ -plot and at  $k \approx 13$  in the  $E_{vv}^i$ -plot. These points are associated with the restricted resolution of an LES compared with a DNS: Figure 4.3 clearly shows the difference between the restricted wavenumber-range on which the LES and the DNS are similar, as concluded from Figure 4.3. Hence, in the following, one should be aware of the fact that the shown spectra has only limited value, namely on  $k \in \langle 0, 17 \rangle$  ( $E_{uu}$ -spectra) and on  $k \in \langle 0, 13 \rangle$  ( $E_{vv}$ -spectra) indicatively.

### 4.3.3 Partial-depth-averaged statistics

The found results make us more interested in the character of the statistics of the large-scale coherent motion. The previous investigation resulted in the insight that with increasing Reynolds-number less energy is transferred to the larger length-scales. But that observation is based on the *fully* depth-averaged statistics of the flow. Now we carry out two more experiments in order to get more insight in the energy-density distributions of the flow at the different Reynolds-numbers. For that, two new experiments are carried out. Firstly, the depth is divided into two parts: a lower half, and an upper half, whereafter a depth-averaging operation is applied per part of the depth, such that we can produce the corresponding two-dimensional energy-density spectra of each part. Secondly, a similar operation is applied, but then dividing the depth into three parts:  $z^+ \in [0, 395]$ ,  $z^+ \in [395, 590]$ ,  $z^+ \in [590, 1000]$ , of course, where possible. For clarity, the depth for the  $Re_\tau = 395$ -case is not divided at all, the depth for the  $Re_\tau = 590$ -case is divided into two parts, and the  $Re_\tau = 1000$ -case is divided into three parts.

In brief, the following regions are to be investigated on their spectral distributions:

Obviously, because of the discretisation in  $z$ -direction (staggered grid), the boundaries of the regions to be investigated can not exactly be set on 395 and 590. But, the largest deviation, namely 406.3 from 395, is 2.9 % and therefore acceptable for a good comparison.

<i>Case, <math>Re_\tau</math></i>	<i>Region</i>	<i>Location bottom, <math>z^+</math></i>	<i>Location top, <math>z^+</math></i>
395	A1	0.0	197.5
395	A2	197.5	395.0
395	A3	0.0	395.0
590	B1	0.0	295.0
590	B2	295.0	590.0
590	B3	0.0	387.0
590	B4	387.2	590.0
590	B5	0.0	590.0
1000	C1	0.0	500.0
1000	C2	500.0	1000.0
1000	C3	0.0	406.3
1000	C4	406.3	593.8
1000	C5	0.0	593.8
1000	C6	593.8	1000.0

**Table 4.3:** Regions to be investigated. The letters A, B and C refer to the cases from Table 4.2.

### Comparison at half-depth

In this experiment we try to obtain the two-dimensional energy-density spectra on the basis of, on the one hand, the depth-averaged velocity field of the lowest half of the water-depth, and, on the other hand, the depth-averaged velocity field of the upper half of the water-depth. To speak in terms of Table 4.3, the spectra from regions A1 and A2, B1 and B2 and C1 and C2 are compared. This comparison is meant to test whether or not there are relative similarities between the several Reynolds-number-cases on the basis of the half the depth.

The results of this experiment are given in Figure 4.7. It should be noted that the spectra are only given here in the integrated version in order to avoid numerous figures with 2d-spectra.

From Figure 4.7, it can be observed that the maxima of the energy-densities are located at the same place as in Figure 4.6, namely at  $k \approx \pi$ . Being aware of the fact that a coherent structure with length-scale equal to the water-depth can be seen as having a wavelength equal to twice the water-depth, it is clear that these coherent structures have the highest energy-density. Another similarity between Figure 4.7 and Figure 4.6 is that the curves intersect each other at  $k \approx 17$  and  $k \approx 13$  respectively.

When comparing Figure 4.7 with Figure 4.6, it is clear that the half-depth-averaged  $E_{vv}$ -spectra contain much more energy than the full-depth-averaged  $E_{vv}$ -spectra. Especially at the low-wavenumber-side of the spectra, Figure 4.7 shows that it has much more energy in the large eddies. The difference in energy-amount is less pronounced in the  $E_{uu}$ -spectra.

Another observation from Figure 4.7 is that the  $E_{uu}$ -peak is higher in the lower-half-spectra, while the  $E_{vv}$ -peak is lower in the lower-half-spectra, compared to the upper-half-spectra.

### Case A compared with case B and case C

Now we will compare spectra, based on depth-averaged velocity-maps, in an absolute sense. The fully depth-averaged case A ( $Re_\tau = 395$ ) is compared with cases B and C (respectively  $Re_\tau = 590$  and  $Re_\tau = 1000$ ), which are for this occasion depth-averaged from  $z^+ = 0$  to  $z^+ = 395$ . In terms of Table 4.3, the

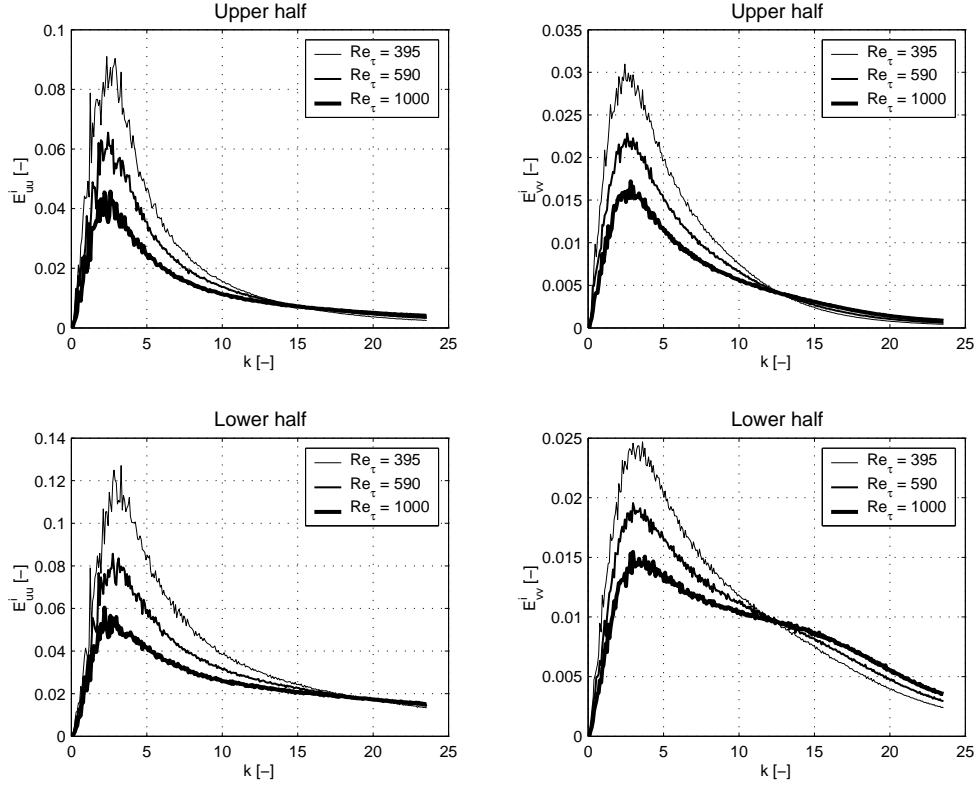


**Figure 4.7:** Integration of the  $E_{uu}$ -spectra contributions (on the left) and  $E_{vv}$ -spectra contributions (on the right), for the upper half of the water-depth (upper plots) and for the lower half of the water-depth (lower plots), for three Reynolds-numbers.

regions A3, B3 and C3 will be compared. The results are shown in Figure 4.8.

Our first observation is that the  $E_{uu}$ -spectra are similar for the three different cases. Only the case  $Re_\tau = 1000$  shows somewhat less energy at the maximum value. At larger wavenumbers the three curves differ a lot, but it should be noted that in this region the LES does not give reliable results. A clear similarity between the curves is the decay of energy on the very-large-scale part of the spectrum: this decay of energy seems to follow the same slope, independent of the Reynolds-number.

The same observation can be made with regard to the 'slope-similarity' of the energy decay of the very-large-scale motion as a result of the  $E_{vv}$ -spectra. Another observation is that the peak-value of the spectra tends to the high wavenumber part with increasing Reynolds-number, while the amount of energy (the peak-value itself) is larger with increasing Reynolds-number.

Comparing Figure 4.6 with Figure 4.8, the figures indicate the depth-averaged velocity maps as resulting from a fully depth-averaging operation to have less energy at the large length-scales than the velocity-maps as resulting from a partially depth-averaging operation near the bottom, especially in the  $E_{vv}$ -cases.

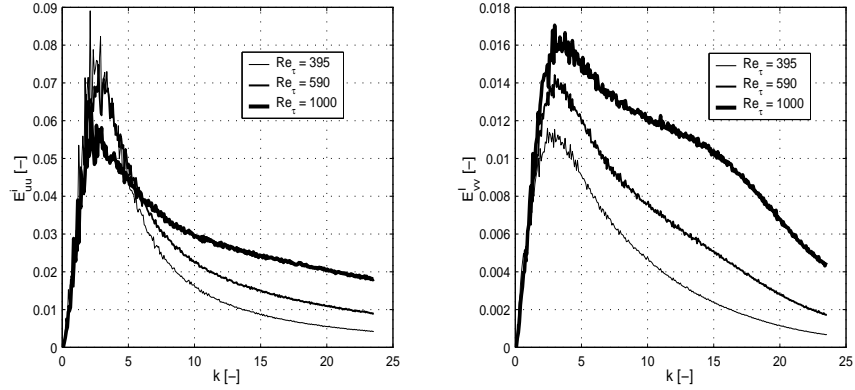


**Figure 4.8:** Integration of the  $E_{uu}$ -spectra contributions (on the left) and  $E_{vv}$ -spectra contributions (on the right), based on depth-averaging from  $z^+ = 0$  to  $z^+ = 395$ , for three Reynolds-numbers.

### Case B compared with case C

Analogously to the investigation in the previous section, the cases B5 and C5 are compared. Thus, again a comparison is made between two cases in order to see whether or not there are similarities in an absolute sense, namely within the region from  $z^+ = 0$  to  $z^+ = 590$ . The results are given in Figure 4.9.

The results as given in Figure 4.9 show us an exactly similar process compared with Figure 4.8: the large-scale part of the  $E_{uu}$ -spectra is the same in both the cases, while the  $E_{vv}$ -spectra show pronounced different peak-values, again, following the concept of the higher the Reynolds-number, the larger the amount of energy, the further the location of the peak-value (i.e. the wavenumber) from the origin, although the latter observation is not very pronounced.

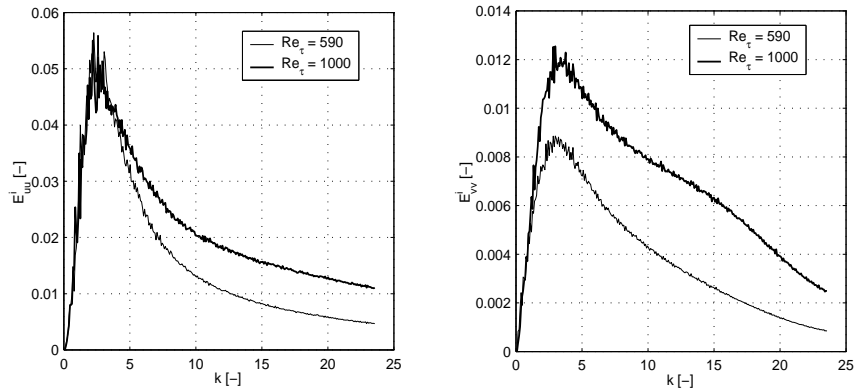


**Figure 4.9:** Integration of the  $E_{uu}$ -spectra contributions (on the left) and  $E_{vv}$ -spectra contributions (on the right), based on depth-averaging from  $z^+ = 0$  to  $z^+ = 590$ , for two Reynolds-numbers.

When comparing Figure 4.8 and Figure 4.9 with Figure 4.7, one sees that Figure 4.8 and Figure 4.9 has a similar decay of energy at the very-large-scales, while Figure 4.7 has maxima on the same locations, for the several Reynolds-numbers.

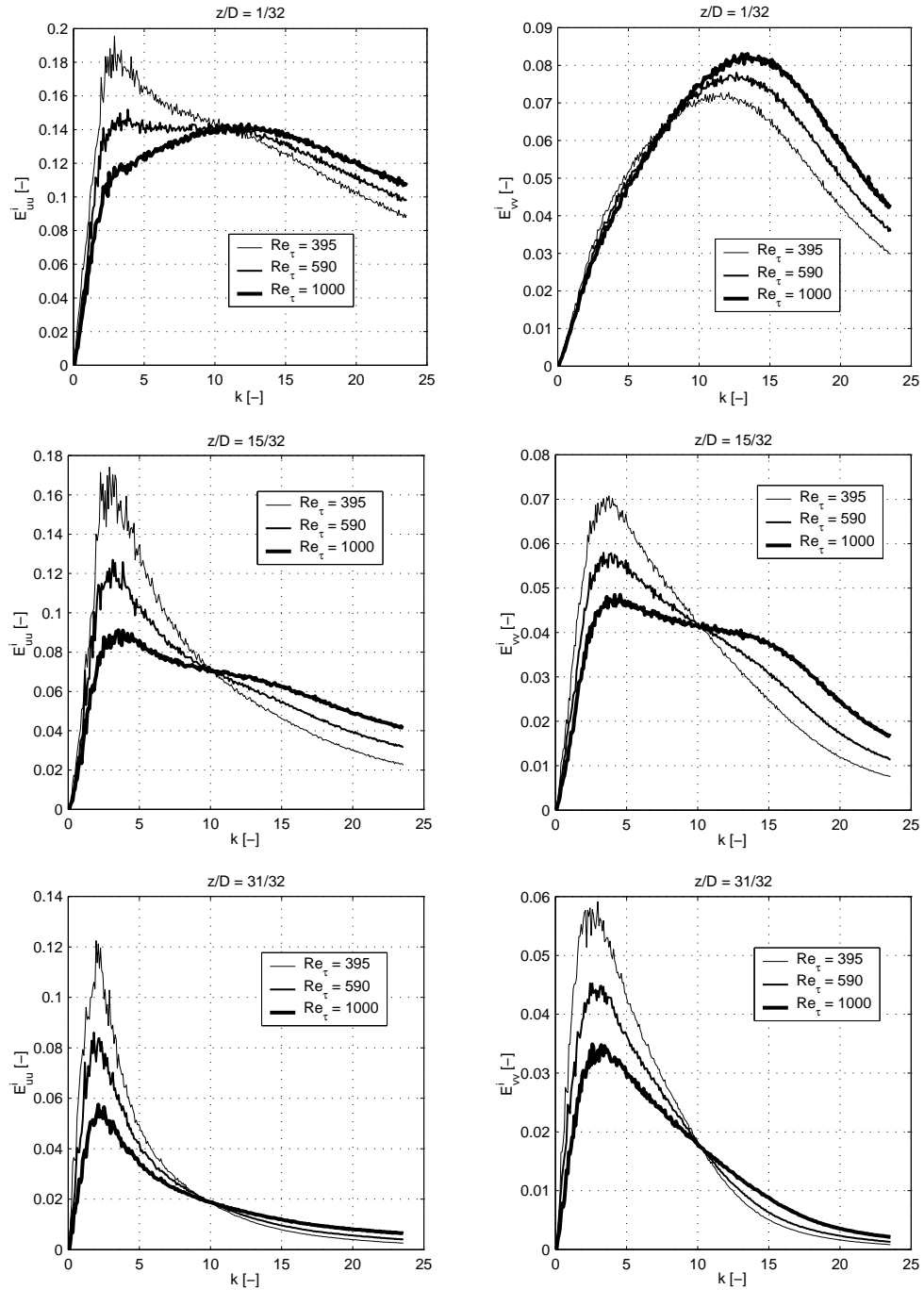


**Figure 4.10:** Two-dimensional energy density spectra of the streamwise velocity fluctuations  $E_{uu}$  (left plots) and the transverse velocity fluctuations  $E_{vv}$  (right plots) for different  $z/D$ , for the three Reynolds-numbers.

### 4.3.4 Overall statistics

To complete the information about the (very-)large-scale motions, another experiment is carried out. Given the fact that for the LES of each case the same discretisation is used, namely  $1024 \times 1024 \times 16$ , we consider the spectral distribution of energy per each layer in the vertical direction. So, for each case 16 2d-spectra are available. These spectra can be observed from a relative view, in terms of outer coordinates  $z/D$ , and an absolute view, in terms of wall-coordinates  $z^+$ .

#### Relative variation in depth

The integrated 2d-spectra can be compared for different values of  $z/D$ . These spectra are given in Figure 4.10. Except for the  $E_{vv}^i$ -case at  $z/D = 1/32$ , one can observe that in each case the amount of energy at the peak-value is decreasing with increasing Reynolds-number. Apparently, with increasing Reynolds-number, less energy is transferred to the larger length-scales. An explanation for this may be that the higher the Reynolds-number, the more three-dimensional velocity fluctuations occur, that claim much energy, such that this process disturbs the energy-transfer to the large length-scales. The exception for the  $E_{vv}^i$ -case at  $z/D = 1/32$  may be found in the fact that, for the case  $Re_\tau = 395$  and the case  $Re_\tau = 590$ , this measuring point is located in the buffer layer ( $z^+ = 12.3$  and  $18.4$  respectively). Here, buffer layer effects may play a role. In any case, in this case the peak-value is not found in the large-scale part of the spectrum at all.

Furthermore, it can be said that the slope-similarity of Figure 4.8 and Figure 4.9 is not observed in Figure 4.10.

#### Absolute variation in depth

In Figure 4.11 the results are given for the spectra as a function of  $z^+$  for each Reynolds-number. Several remarkable observations can be done. Firstly, one sees with higher  $z^+$ -values (larger distance to the bottom) a clear shift of the location of the peak-value to the left, while the peak-value itself is decreasing. In other words: the larger the distance from the bottom, the larger are the length-scales of the coherent structures, while the coherent structures themselves are less energetic. Secondly, closely related to the first observation, one sees again a slope-similarity of the curves in the region between the origin and the peak-value. This observation does not hold for the integrated spectra at the most near-wall gridpoint. As said in the previous subsection, this might be a result of buffer-layer effects or wall-function effects.

## 4.4 Discussion and conclusion

In this chapter we did numerical experiments on a channel flow at three different Reynolds-numbers were shown with particular attention to two-dimensional energy-density spectra and their polar integrated equivalents as well. These spectra were investigated in three ways: (a) on the basis of full-depth-averaged velocity maps, (b) on the basis of partial-depth-averaged velocity maps and (c) 'pure' velocity maps (no depth-averaging at all).

Investigation (a) led to the insight that with increasing Reynolds-number, less turbulent kinetic energy is transferred to the larger length-scales, while the range of wavenumbers with a significant amount of energy is slightly increasing. This is attributed to the stronger generation of three-dimensional turbulence for higher Reynolds-numbers. These three-dimensional turbulence is more isotropic and hampers the

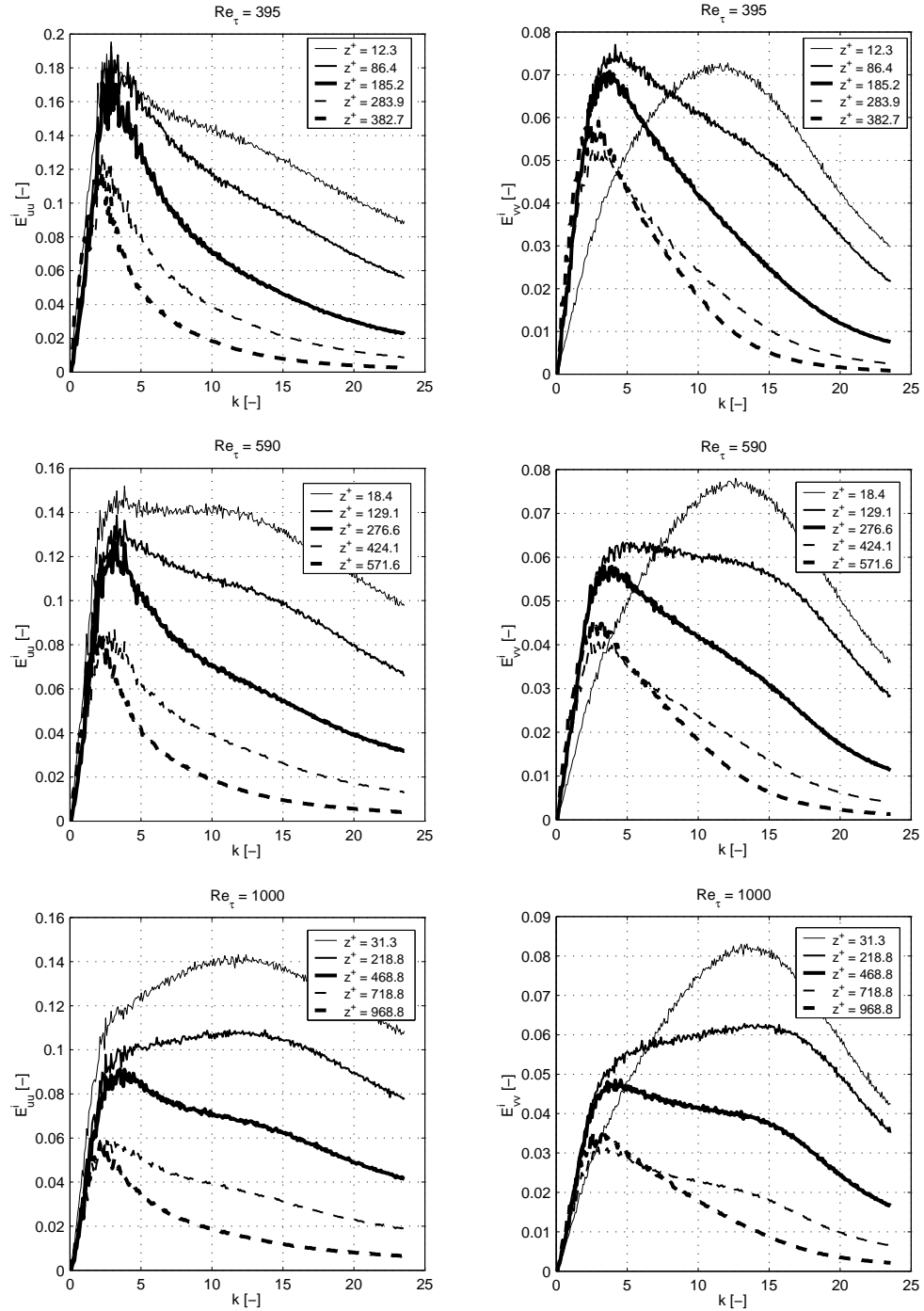


**Figure 4.11:** Two-dimensional energy density spectra of the streamwise velocity fluctuations  $E_{uu}$  (left plots) and the transverse velocity fluctuations  $E_{vv}$  (right plots) for different  $z^+$ , for the three Reynolds-numbers.

two-dimensional effect of the generation of stronger large-scale motions. This effect was observed at investigation (b) and (c) as well.

Main result of investigation (b) is the observation that the large-scale part of the spectra of the streamwise velocities tend to the same shape with increasing Reynolds-number: Figure 4.8 (left panel) shows this similarity between  $Re_\tau = 395$  and  $Re_\tau = 590$  and Figure 4.9 (left panel) shows this similarity between  $Re_\tau = 590$  and  $Re_\tau = 1000$ . This makes the question rise, whether or not the large-scale part of these  $E_{uu}$ -spectra tend to the same shape, invariantly of the Reynolds-number, in the neighbourhood of solid wall. This could give cause to the formulation of a spectral wall-function, independent of the Reynolds-number. The  $E_{vv}$ -spectra, however, only show the same decay towards  $k \downarrow 0$ , but not the same representation of the peak-value and its location.

Investigation (c) showed that a comparison of the data in a 'relative' sense (i.e. in terms of outer coordinates  $z/D$ ) resulted in the insight that the peak-value, in each case, is located at the same  $k$ -value, while a comparison of the data in an 'absolute' sense (i.e. in terms of wall-coordinates  $z^+$ ) resulted in the insight that the decay of large-scale motion shows a kind of slope-similarity towards the very-large-scale motion ( $k \downarrow 0$ ). These results show generally the large-scale motion to have less energy with increasing Reynolds-number as well.

Comparison of these three investigations, furthermore, makes clear that applying a depth-averaging operation on the velocity-maps makes significant amounts of energy vanish. This should be kept in mind when representing these spectra within the context of a kinematic simulation technique.

# Chapter 5

## Kinematic simulation

In the previous chapter, we acquired knowledge about the spectral distributions of the large-scale motion in channel flows at different Reynolds-numbers. This knowledge can be used for an improvement of depth-averaged simulation techniques, in particular depth-averaged simulations with a kinematic simulation (see for instance Van Prooijen (2003)). This method uses *a priori* knowledge about the spectral distribution of the case to be simulated, and is therefore suitable to represent bottom-induced turbulence in a two-dimensional simulation. With the collected data from the previous chapter, a large step is made to formulate proper *a priori* spectral distribution to be used in a depth-averaged simulation with a kinematic simulation.

### 5.1 Depth-averaged simulation

In the following we formulate the basis of a depth-averaged simulation wherein the depth-averaged large-scale motion is simulated by means of a kinematic simulation. Therefore, we start with the two-dimensional shallow water equations, which describe the flow, where the horizontal length-scales are significantly larger than the water depth. Notice that we now leave the LES-paradigm of averaging in space, and replace the averaging in space by an averaging in time. The time-averaged quantities are now provided with an overline ( $\overline{\varphi} = \frac{1}{T} \int_0^T \varphi dt$ ).

#### 5.1.1 Shallow water equations

The continuity equation and the momentum equations in the horizontal plane are averaged over the water-depth and averaged over a period larger than the time scale of the three-dimensional bottom turbulence, but smaller than the time scale of the large scale motion, resulting in:

$$\frac{\partial \overline{u}}{\partial x} + \frac{\partial \overline{v}}{\partial y} = 0 \quad (5.1)$$

$$\frac{\partial \overline{u}}{\partial t} + \overline{u} \frac{\partial \overline{u}}{\partial x} + \overline{v} \frac{\partial \overline{u}}{\partial y} = -\frac{1}{\rho} \frac{\partial \overline{p}}{\partial x} - \frac{c_f}{D} \overline{u} \sqrt{\overline{u}^2 + \overline{v}^2} + \nu_t \left( \frac{\partial^2 \overline{u}}{\partial x^2} + \frac{\partial^2 \overline{u}}{\partial y^2} \right) \quad (5.2)$$

$$\frac{\partial \overline{v}}{\partial t} + \overline{u} \frac{\partial \overline{v}}{\partial x} + \overline{v} \frac{\partial \overline{v}}{\partial y} = -\frac{1}{\rho} \frac{\partial \overline{p}}{\partial y} - \frac{c_f}{D} \overline{v} \sqrt{\overline{u}^2 + \overline{v}^2} + \nu_t \left( \frac{\partial^2 \overline{v}}{\partial x^2} + \frac{\partial^2 \overline{v}}{\partial y^2} \right), \quad (5.3)$$

where  $c_f$  is the bed-friction coefficient for turbulent flow over a smooth bottom and it determined by the relation

$$\frac{1}{\sqrt{c_f}} = \frac{1}{\kappa} (\ln (Re\sqrt{c_f} + 1)) \quad (5.4)$$

in which  $Re = \tilde{u}D/\nu$  represents the depth-based Reynolds-number. As we deal with a TRANS-model, we need to model the bottom turbulence by using a turbulence eddy-viscosity. We take (as in Van Prooijen (2003)):

$$\nu_t = \alpha Du_\tau = \alpha D\sqrt{c_f}\tilde{u}, \quad (5.5)$$

with  $\alpha$  a certain constant, often chosen equal to about 0.10. Now when having the depth-averaged and time-averaged equations, we apply, for our channel-flow, the decomposition

$$\bar{u}(x, y, t) = \tilde{u}(x, y) + u'(x, y, t), \quad \bar{v}(x, y, t) = v'(x, y, t), \quad \bar{p}(x, y, t) = \tilde{p}(x, y) + p'(x, y, t) \quad (5.6)$$

where  $\tilde{u}$  is a mean velocity and  $u'$  a fluctuation, and  $\tilde{p}$  and  $p'$  analogously a mean and a fluctuation. When we apply Reynolds-decomposition to the shallow water equations (5.1) - (5.3), we obtain the equations for the fluctuations. Omitting the higher order terms, these result in:

$$\frac{\partial u'}{\partial x} + \frac{\partial v'}{\partial y} = 0 \quad (5.7)$$

$$\frac{\partial u'}{\partial t} + \tilde{u} \frac{\partial u'}{\partial x} = -\frac{\partial p'}{\partial x} - \frac{2c_f\tilde{u}}{D}u' + \nu_t \left( \frac{\partial^2 u'}{\partial x^2} + \frac{\partial^2 u'}{\partial y^2} \right) \quad (5.8)$$

$$\frac{\partial v'}{\partial t} + \tilde{u} \frac{\partial v'}{\partial x} = -\frac{\partial p'}{\partial y} - \frac{c_f\tilde{u}}{D}v' + \nu_t \left( \frac{\partial^2 v'}{\partial x^2} + \frac{\partial^2 v'}{\partial y^2} \right) \quad (5.9)$$

The second term on the right-hand-side of equations (5.8) and (5.9) is obtained from a first order Taylor expansion of the bottom friction contribution.

### 5.1.2 Kinematic simulation

Having formulated the governing shallow water equations, together with some needed constitutive equations for the friction and eddy-viscosity, and knowing the results of our large-eddy simulations, we apply a *kinematic simulation* to simulate the depth-averaged large-scale motion. The principle of a kinematic simulation is described by Fung *et al.* (1992). The basic idea of a kinematic simulation is the simulation of an instantaneous velocity field by a summation of Fourier modes:

$$u'_{ks}(x, y) = \lim_{N \rightarrow \infty} \frac{1}{N} \sum_{n=1}^N \hat{u}^n \sin(k_x^n x + k_y^n y + \phi^n) \quad (5.10)$$

$$v'_{ks}(x, y) = \lim_{N \rightarrow \infty} \frac{1}{N} \sum_{n=1}^N \hat{v}^n \sin(k_x^n x + k_y^n y + \phi^n) \quad (5.11)$$

In expressions (5.10) and (5.11), the coefficients  $k_x$ ,  $k_y$  and  $\phi$  are random vector Fourier coefficients (wavenumbers and phase). The amplitudes  $\hat{u}$  and  $\hat{v}$  have to be prescribed such that the corresponding

energy density distribution mimicks the spectra of the three-dimensional LES. These amplitudes have to satisfy four requirements.

Firstly, the large-scale motions should satisfy *continuity*. Satisfying this requirement means a coupling of the streamwise and transverse motions, and hence also a coupling of both the corresponding spectra. Thus, the wavenumbers  $k_x$  and  $k_y$  should be linked.

Secondly, as the spectra from Figure 4.5 show a strong anisotropy of the flow, the simulated velocity-field should have this *anisotropy* as well. On the one hand, this anisotropy reflects the shape of the spectra, which are different for the streamwise and transverse velocities. On the other hand, combining the continuity-principle and the anisotropy-principle, the values of the energy-densities in the streamwise direction should be larger than in the values in the transverse direction. This connection is laid by the scaling with  $k_y$  and non-dimensionality for scaling with  $k$ .

Thirdly, the velocities should be scaled with the friction velocity  $u_\tau$ , as done in the 3D-LES. This *velocity scaling* property should enable us to compare the results easily.

Fourthly, the wavenumbers are made dimensionless with the depth. The factor associated with this *length scaling* property is such to be chosen that the spectra fit the data well.

With

$$|k^n| = \sqrt{(k_x^n)^2 + (k_y^n)^2},$$

combining these four requirements, leads us to the following two expressions:

$$\hat{u}(k_x^n, k_y^n) = \underbrace{\alpha u_\tau}_{\text{velocity-scaling}} \cdot \underbrace{\lambda |k^n| D \cdot e^{-\lambda |k^n| D}}_{\text{length-scaling}} \cdot \underbrace{\left(\frac{k_y^n}{|k^n|}\right)^\beta}_{\text{anisotropy}} \cdot \underbrace{\frac{k_y^n}{|k^n|}}_{\text{continuity}}, \quad (5.12)$$

$$\hat{v}(k_x^n, k_y^n) = - \underbrace{\alpha u_\tau}_{\text{velocity-scaling}} \cdot \underbrace{\lambda |k^n| D \cdot e^{-\lambda |k^n| D}}_{\text{length-scaling}} \cdot \underbrace{\left(\frac{k_y^n}{|k^n|}\right)^\beta}_{\text{anisotropy}} \cdot \underbrace{\frac{k_x^n}{|k^n|}}_{\text{continuity}}, \quad (5.13)$$

where  $\alpha$ ,  $\beta$  and  $\lambda$  are model-parameters, which can be used to fit the characteristics of the kinematic simulation with the results from the 3D-LES.

A drawback, or better said, an incompleteness of expressions (5.12) and (5.13) is the lack of a time-dependency. Obviously, time-dependency should be added. Fung (1992) supposes advection of the kinematic fluctuations by the mean flow, along fluid particle trajectories (for a matter of fact, Fung's large-scale motions and small-scale motions are uncorrelated). Hence, Fung (1992) proposes  $x - \int_0^t u dt$  and  $y - \int_0^t v dt$  to replace  $x$  and  $y$  in (5.10) and (5.11). Van Prooijen (2003), however, makes the amplitudes (5.12) and (5.13) time-dependent. The expressions for  $u'_{ks}$  and  $v'_{ks}$  then become:

$$u'_{ks}(x, y, t) = \lim_{N \rightarrow \infty} \frac{1}{N} \sum_{n=1}^N \sqrt{2} \sin \left( \int_0^t (k_x^n \tilde{u} + k_y^n \tilde{v}) dt + \theta^n \right) \hat{u}^n \sin (k_x^n x + k_y^n y + \phi^n), \quad (5.14)$$

$$v'_{ks}(x, y, t) = \lim_{N \rightarrow \infty} \frac{1}{N} \sum_{n=1}^N \sqrt{2} \sin \left( \int_0^t (k_x^n \tilde{u} + k_y^n \tilde{v}) dt + \theta^n \right) \hat{v}^n \sin (k_x^n x + k_y^n y + \phi^n), \quad (5.15)$$

where, obviously, the extra amplitude-term depends on the local mean velocities  $\tilde{u}$  and  $\tilde{v}$  and the random wavenumbers of the mode. The factor  $\sqrt{2}$  is added to keep the total amount of kinetic energy correct.

### 5.1.3 Integrating the kinematic simulation with the shallow water equations

Now we are in the possession of two important tools for the two-dimensional description of shallow flows with large-scale coherent structures: the shallow water equations to account for the depth-averaged motion, and the kinematic simulation to represents large-scale motion. How can these two models be combined in one model?

To this end, two things should be said: firstly, we can learn from equations (5.8) and (5.9) what the influence is of fluctuations. We clearly see the forcing terms arising from these equations: a forcing term representing the bottom-friction force with coefficient  $c_f$ , and a forcing term representing the bottom-turbulence with the eddy-viscosity  $\nu_t$ . Secondly, as we want to solve equations (5.1) - (5.3), the large-scale motion should be represented by a certain forcing term. Combining these two notions, the solution is easily found: add the two forcing terms in equations (5.1) - (5.3), but now with  $u'_{ks}$  and  $v'_{ks}$  as variables. The two forcing terms then become, with opposite sign:

$$F_x = +\frac{2c_f\tilde{u}}{D}u'_{ks} - \nu_t \left( \frac{\partial^2 u'_{ks}}{\partial x^2} + \frac{\partial^2 u'_{ks}}{\partial y^2} \right) \quad (5.16)$$

$$F_y = +\frac{c_f\tilde{u}}{D}v'_{ks} - \nu_t \left( \frac{\partial^2 v'_{ks}}{\partial x^2} + \frac{\partial^2 v'_{ks}}{\partial y^2} \right). \quad (5.17)$$

Then, equations (5.1) - (5.3) to be solved, become:

$$\frac{\partial \bar{u}}{\partial x} + \frac{\partial \bar{v}}{\partial y} = 0 \quad (5.18)$$

$$\frac{\partial \bar{u}}{\partial t} + \bar{u} \frac{\partial \bar{u}}{\partial x} + \bar{v} \frac{\partial \bar{u}}{\partial y} = -\frac{1}{\rho} \frac{\partial \bar{p}}{\partial x} - \frac{c_f}{D} \bar{u} \sqrt{\bar{u}^2 + \bar{v}^2} + \nu_t \left( \frac{\partial^2 \bar{u}}{\partial x^2} + \frac{\partial^2 \bar{u}}{\partial y^2} \right) + \underbrace{\frac{2c_f\tilde{u}}{D}u'_{ks} - \nu_t \left( \frac{\partial^2 u'_{ks}}{\partial x^2} + \frac{\partial^2 u'_{ks}}{\partial y^2} \right)}_{\text{kinematic simulation}} \quad (5.19)$$

$$\frac{\partial \bar{v}}{\partial t} + \bar{u} \frac{\partial \bar{v}}{\partial x} + \bar{v} \frac{\partial \bar{v}}{\partial y} = -\frac{1}{\rho} \frac{\partial \bar{p}}{\partial y} - \frac{c_f}{D} \bar{v} \sqrt{\bar{u}^2 + \bar{v}^2} + \nu_t \left( \frac{\partial^2 \bar{v}}{\partial x^2} + \frac{\partial^2 \bar{v}}{\partial y^2} \right) + \underbrace{\frac{c_f\tilde{u}}{D}v'_{ks} - \nu_t \left( \frac{\partial^2 v'_{ks}}{\partial x^2} + \frac{\partial^2 v'_{ks}}{\partial y^2} \right)}_{\text{kinematic simulation}}, \quad (5.20)$$

which now become the equations to be solved. We refer to expression (3.1) to show the transient-RANS-character of equations (5.18) - (5.20).

## 5.2 Analysis of the method

What we now have is a depth-averaged Transient Reynolds Averaged Numerical Simulation with kinematic simulation, which, henceforth, will be denoted the 2D-TRANS+ks model. We are now ready to generate data with the 2D-TRANS+ks to compare these with the 3D-LES-data in order to see whether or not the 2D-TRANS+ks is useful to model depth-averaged shallow flows with large coherent structures. This comparison will take place in one of the following chapters. Now we will focus on the combination of the obtained information in the previous chapter with the application of the 2D-TRANS+ks model.

### 5.2.1 Imitating the energy-density spectra

#### Two-dimensional spectra

As said, the idea of the kinematic simulation method is to simulate the bottom-induced turbulence by mimicking the two-dimensional spectra. An idea is to use spectra on the basis of the fully depth-averaged velocity maps, as done for instance in Van Prooijen (2003). We can improve this method by taking the Reynolds-dependency of the spectra into account.

For instance, for the case  $Re_\tau = 590$ , it can be seen that the model-parameters  $\alpha$ ,  $\beta$  and  $\lambda$  fit the data (i.e. the spectra) quite well, when being equal to 1.3, 3.0 and 0.4 respectively.

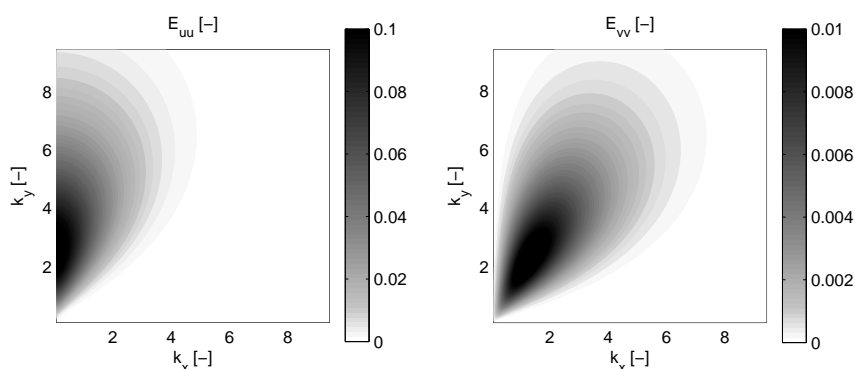


**Figure 5.1:** Simulated energy-density spectra by formulas (5.12) and (5.13) for  $Re_\tau = 590$ , with parameters  $\alpha = 1.3$ ,  $\beta = 3.0$  and  $\lambda = 0.4$ .

When comparing Figure 5.1 with Figure 4.5, it is seen that there is a clear similarity with the simulated spectra and the real spectra. Only the shape of the  $E_{vv}$ -spectra is slightly different: the ridge  $k_y = k_x$  is changed into  $k_y = 1.4 k_x$ .

Within the framework of improving the method, it is important to make the method suitable for each Reynolds-number. From formulas (5.12) and (5.13), it is clear that parameters  $\beta$  and  $\lambda$  determine the shape of the spectra, while  $\alpha$  mainly determines the amount of present energy. Therefore, to make the set of parameters suitable for a whole range of Reynolds-numbers, in fact, only parameter  $\alpha$  is useful. When simulating the spectra of Figure 4.5 by formulas (5.12) and (5.13), the values for  $\alpha$  turned out to be suitable, are given in Table 5.1.

$Re_\tau$	$\alpha$
395	1.6
590	1.3
1000	1.0

**Table 5.1:** Values for  $\alpha$ , for each Reynolds-number-case. For each case,  $\beta = 3.0$  and  $\lambda = 0.4$ .

To represent the dependency of  $\alpha$  on  $Re$ , the following expression is proposed:

$$\alpha(Re_\tau) = \frac{c_1}{Re_\tau} + c_2 \quad (5.21)$$

With expression (5.21) it is possible to represent the decrease of  $\alpha$  with increasing  $Re_\tau$ , without coming into the neighbourhood of zero, which is not possible: the limit-case  $Re_\tau \rightarrow \infty$  should have a non-zero energy-amount, even larger than zero. Applying a least-squares method, parameters  $c_1$  and  $c_2$  turn out to have the values 391 and 0.62 respectively.

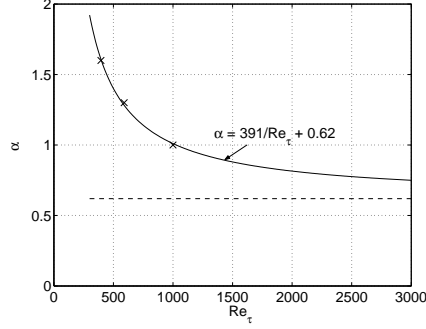


**Figure 5.2:** Dependency of  $\alpha$  on  $Re_\tau$ .

The small difference in shape of the spectra for each case, as found in Figure 4.5, is not taken into account as the difference of the simulated spectra (Figure 5.1) and the real spectra (Figure 4.5) is much larger than the mutual differences of shape within Figure 4.5 itself. But it is expected that the amount of energy (for which the parameter  $\alpha$  plays the most important role) is a quantity that has to be accounted for.

### Integrated spectra

In the previous chapter, we represented the two-dimensional spectra in their one-dimensional, circular integrated equivalents. We can do the same for the mimicked spectra from the kinematic simulation in order to be able to come to a good comparison of the LES results and the kinematic simulation. The results are shown in Figure 5.3.

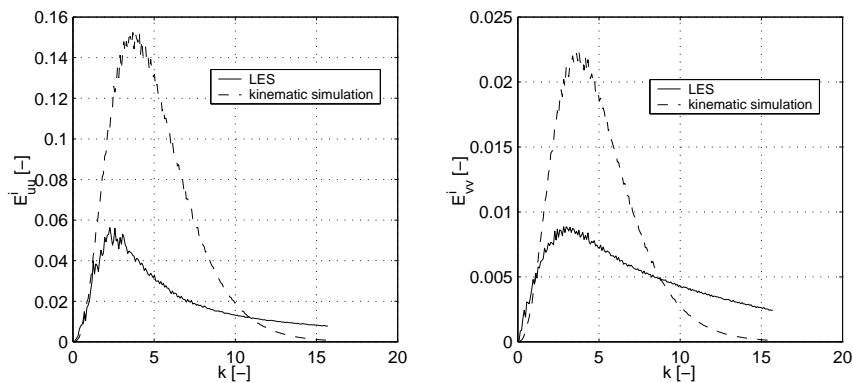


**Figure 5.3:** Comparison of the LES spectra and the spectra from the kinematic simulation, for  $Re_\tau = 590$ .

Remembering that very-large-scale coherent structures with length-scale larger than the waterdepth have  $k < \pi$ , it can be concluded from Figure 5.3, that the large-scale motion is represented quite well by the

kinematic simulation. Coherent structures with length-scale smaller than the waterdepth have, however, much more energy than as follows from the LES.

When we now only use the part of the simulated spectra where these spectra coincide with the spectra as resulted from the LES, we can use the kinematic simulation for the representation of the large-scale motions. If we want to represent large-scale motions with length-scales larger than about two times the waterdepth, we use the  $k$ -range  $k \in \langle 0, \frac{1}{2}\pi \rangle$ .

## 5.2.2 Imitating the velocity-field

How we can apply the expressions from the previous section in order to represent the large-scale motions in a corresponding velocity-field, is explained in Appendix B. The *initial* velocity-fields are given in Figure 5.4, for  $Re_\tau = 590$ .

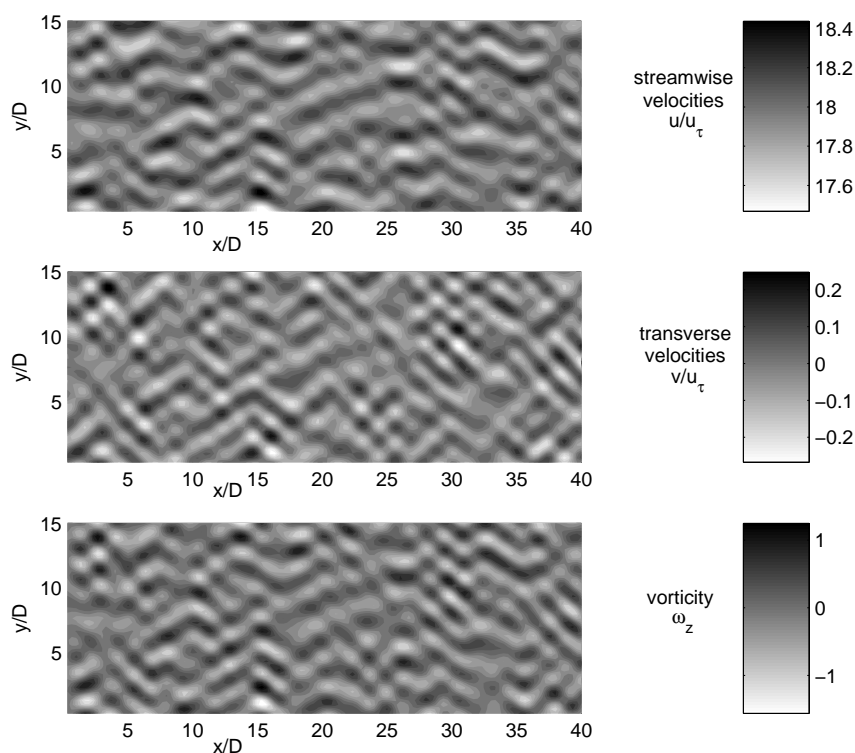


**Figure 5.4:** Simulation of the very-large-scale motion using a kinematic simulation, for  $Re_\tau = 590$ . Upper plot shows the streamwise velocities  $u$ , the middle plot shows the transverse velocities  $v$ , and the lower plot shows the vorticity  $\omega_z$ .

Obviously, Figure 5.4 only shows the large-scale motion, induced by the large-scale bottom turbulence. These velocity maps are imposed as *initial* conditions. Figure 5.4 also shows that the streamwise velocities are elongated in streamwise direction, while the transverse velocities are more isotropic. This is consistent with the shape of the spectra, as found in chapter 4.

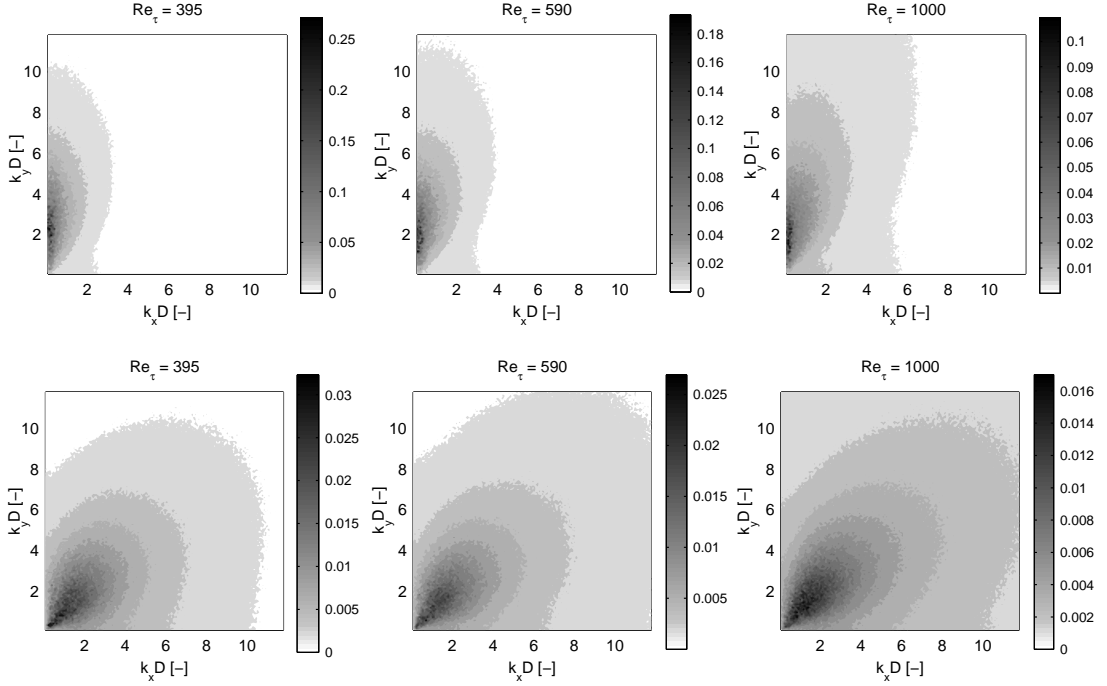


Figure 5.5: Depth-averaged two-dimensional energy-density spectra, for three Reynolds-numbers.

## 5.3 Multi-layered model

### Two-dimensional spectra

If we want to extend the proposed two-dimensional method to more layers in the third dimension, then another method can be used. Using the depth-averaged two-dimensional spectral distributions, see Figure 5.5, and using the slope-similarity for low  $k$ -values, see Figure 4.11, the parameter-set  $\alpha = 1.3$ ,  $\beta = 1.0$ ,  $\lambda = 0.4$  (if  $Re_\tau = 590$ ) can be proposed to represent the bottom influences. The thus obtained mimicked spectra are given in Figure 5.6.

From Figure 5.6 it is clear that the maximum value of the  $E_{uu}$ -spectra seems to be strongly underestimated. However, given the fact that the colorbar of Figure 5.5 shows that the occurring maximum value of 0.18 is not reached in a wide part of the spectrum, this underestimation is not seen as a problem. The shape of the spectra is very well represented by Figure 5.6.

### Integrated spectra

Basis of this alternative is the slope-similarity of Figure 4.11. This slope should therefore appropriately be simulated. Advantage of a good representation of this slope, is that the expression can be used in each layer of the model. Another advantage of this method is, that, as vertical correlations are absent when proposing the same expression for each layer, we do not have spurious correlations, caused by the random terms in Equation 5.14 and Equation 5.15. The integrated, one-dimensional, variants are given in Figure 5.7.

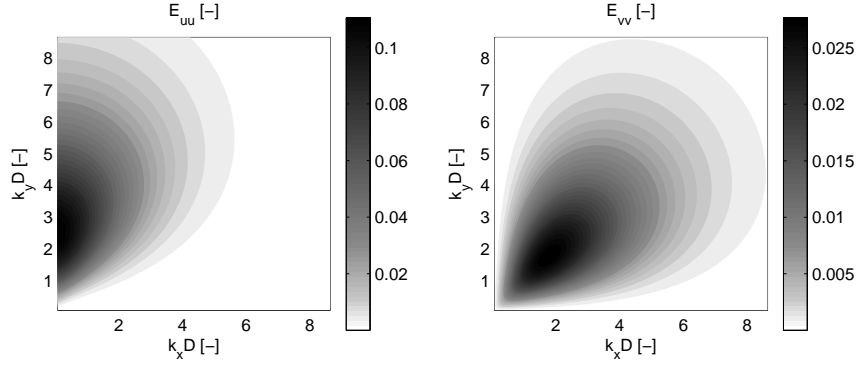


**Figure 5.6:** Simulated energy-density spectra by formulas (5.12) and (5.13) for  $Re_\tau = 590$ , with parameters  $\alpha = 1.3$ ,  $\beta = 1.0$  and  $\lambda = 0.4$ .

The spectra in Figure 5.7 show good resemblance with the integrated equivalents of the two-dimensional spectra from the LES. The spectra roughly coincide for  $k$ -values smaller than about 2.5. Remembering that the  $k$ -values associating with the maximum values in the spectra of Figure 4.11 decrease with increasing distance from the wall, the cut-off wavenumber is determined by the spectrum of the layer most far of the wall, resulting in  $k \approx 2$ .

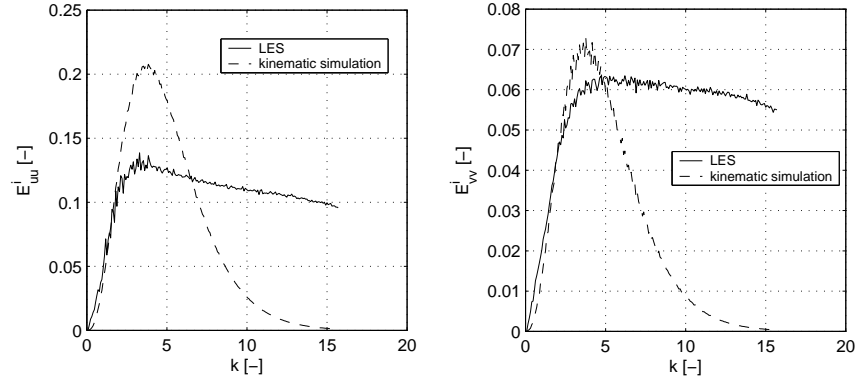


**Figure 5.7:** Comparison of the LES spectra at  $z^+ = 129.1$  and the spectra from the kinematic simulation, for  $Re_\tau = 590$ .

In the previous section it was seen that the parameter  $\alpha$  depends on the Reynolds number. The same yields for the representation of the spectra in Figure 5.6. It turns out that the dependency on the Reynolds-number is exactly the same as in the previous section. Hence, expression (5.21) can be used in the multi-layered model as well, with the same values for  $c_1$  and  $c_2$ .

It can be concluded that the lowering of the parameter  $\beta$  from 3.0 to 1.0, together with the standard values for  $\alpha$  from Table 5.1 and  $\lambda = 0.4$ , results in an appropriate parameter set that can be used in a multi-layered model.



## Chapter 6

# Influence of disturbances

In the previous chapters, we saw that the very-large-scale motions, as present in the investigated channel flow, are significantly energetic: even at the largest possible size (i.e. the domain size) there is a certain amount of energy found. In this chapter, we will look at the effect of energy at the very-large length-scales on the development of coherent structures in shallow flows. Therefore we investigate the influence of disturbances on both the temporal and spatial development of coherent structures in shallow flows. To that end, three experiments are carried out: (*a*) a checkerboard distribution of vortices is implemented as initial condition field in a 2D-LES, (*b*) a 2D-LES is carried out on a grid-flow case, where coherent structures are generated downstream of a grid of obstacles at the inflow boundary and (*c*) a full 3D-LES is carried out on the same grid-flow case.

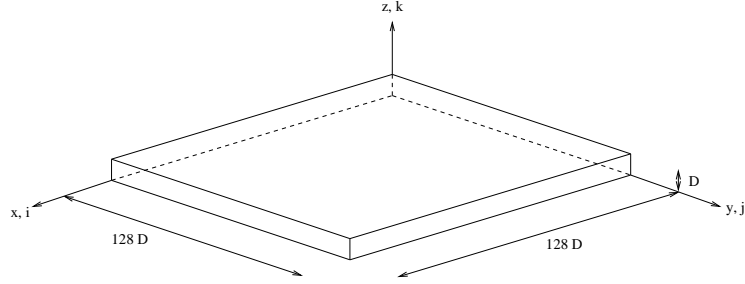
### 6.1 Background and objective

The starting point of thinking is the hypothesis that in quasi-two-dimensional turbulence the dissipation is very much depending on the size of the eddies. Very-large-scale motions are weakly dissipative, which gives rise to the idea that the rate at which turbulent kinetic energy is transferred to the larger scales does affect the decay of turbulent kinetic energy in a quasi-two-dimensional flow. The hypothesis is, that the larger the disturbance of this field with coherent structures, the lesser is the loss of turbulent kinetic energy. Hence, per disturbance, a different energy level is reached. We put this hypothesis to the test by perturbing the initial flow field with increasing disturbances to see what the influence is of these perturbations on the evolution of turbulent kinetic energy and enstrophy. The idea is that experiment (*a*) gives insight in the temporal development of the coherent structures, where experiments (*b*) and (*c*) give insight in the spatial development of these coherent structures.

### 6.2 Temporal development of coherent structures

#### 6.2.1 Numerical setup

The shallow computational domain as used in the previous chapter is now used again, however with modified dimensions in streamwise and spanwise direction. See Figure 6.1. Data on the computational domain and its discretisation, is given in Table 6.1.

**Figure 6.1:** Computational domain.

$L_x$	$L_y$	$L_z$	$N_x$	$N_y$	$N_z$
$128D$	$128D$	$D$	512	512	3

**Table 6.1:** Lengths of the domain with the number of gridpoints in each direction.

The number of gridpoints in  $z$ -direction  $N_z$  is chosen equal to 3, because the options  $N_z = 1$  and  $N_z = 2$  resulted in useless results for technical reasons (pressure-correction-method fails in these cases). To avoid each minimal influence of three-dimensionality, the velocities in  $z$ -direction,  $w$ , are put equal to zero after each time-step. In fact, we use a 3D-LES (with *free-slip* boundaries at the bottom and the free surface) for a 2D calculation. For convenience, however, we will call this calculation a 2D-LES henceforth.

To assure the solenoidality of the velocity-field, the initial conditions are derived from the streamfunction  $\psi$ . Remembering that the vorticity  $\omega$  equals the Laplacian of the streamfunction  $\psi$ ,  $\omega = \nabla^2 \psi$ , the initial streamfunction can be described by:

$$\psi(x, y) = \frac{U_0}{k} \sin(kx) \sin(ky) \quad (6.1)$$

with  $U_0$  a certain velocity to be chosen,  $k = \frac{2\pi}{\Lambda}$  the wavenumber with  $\Lambda$  the wavelength, such that the vorticity-field contains  $2 \cdot 128D/\Lambda$  vortices in each direction, which stays to be an optional parameter. The vorticity-distribution is now:

$$\omega(x, y) = \frac{\partial^2 \psi}{\partial x^2} + \frac{\partial^2 \psi}{\partial y^2} = -2U_0 k \sin(kx) \sin(ky) \quad (6.2)$$

In order to make the principle of self-organisation best visible, the following parameters are chosen to get a vorticity-field of  $8 \times 8$  vortices with alternating sign:

Number of vortices	$Re$	$U_0$	$\Lambda$
$8 \times 8$	100	1	$32D$

**Table 6.2:** Parameter settings.

Everywhere in this chapter an  $8 \times 8$ -vorticity-field is used, unless mentioned otherwise. For lack of a pressure-gradient as an external body force, the  $Re$ -number can be interpreted as an inverse molecular viscosity (see Appendix B).

## 6.2.2 Perturbations

After having defined a proper streamfunction, this streamfunction is to be perturbed in order to get information that should enable us to judge our hypothesis. These random perturbations are applied in the amplitude of the streamfunction. In order to be as complete as possible, three types of disturbances are applied: micro-scale disturbances, meso-scale disturbances and macro-scale disturbances. Obviously, we are mostly interested in the macro-scale perturbations, as these are meant to model the very-large-scale motions, which have, as said, a clear non-zero amount of energy. But, with perturbing the flow also on other length-scales, we are able to put the influence of these large-scale perturbations into a certain perspective. For every perturbation, we disturb the flow on five levels of intensity, to call  $\delta_n$  henceforth. The used values for  $\delta_n$  are given in Table 6.3.

$n$	$\delta_n$
1	0.001 %
2	0.01 %
3	0.1 %
4	1.0 %
5	5.0 %

**Table 6.3:** Values for  $\delta_n$ , representing the intensity of each disturbance.

### Micro-scale disturbances

With micro-scale disturbances, we mean locally imposed disturbances on the streamfunction with each intensity  $\delta_n$ . Thus, each value of the streamfunction, in the whole domain, is randomly perturbed with a amplitude  $\delta_n$ . Perturbations on this length-scale will be referred to as the MI-case.

### Meso-scale disturbances

With meso-scale disturbances, we mean disturbances with a length-scale much larger than the previous ones, but much smaller than the domain sizes  $L_x$  and  $L_y$ . Remembering that  $k = 2\pi/32D$  (see Table 6.2), two cases that will be calculated are given in Table 6.4:

<i>Case</i>	<i>Disturbance</i>
ME-1	$\delta_n \sin(2kx) \sin(2ky)$
ME-2	$\delta_n \sin(\frac{1}{3}kx) \sin(\frac{1}{3}ky)$

**Table 6.4:** Perturbations on meso-scale.

In our initial field with a  $8 \times 8$  checkerboard, simulating  $8 \times 8$  coherent structures, the initial coherent structures have length-scale  $1/8 \cdot 128D = 16D$ . The imposed perturbations are in fact coherent structures with a length-scale, in these cases, equal to  $8D$  and  $48D$  respectively. Thus, in the ME-1-case, a length-scale smaller than the length-scale of the initial coherent structures, and in the ME-2-case, a length-scale larger than the length-scale of the initial coherent structures, which is, in this case, an odd multiple of the initial length-scale.

### Macro-scale disturbances

With macro-scale disturbances we mean disturbances with length-scales equal to the domain size. The following four cases are investigated:

Case	Disturbance
MA-1	$\delta_n \sin\left(\frac{1}{8}kx\right) \sin\left(\frac{1}{8}ky\right)$
MA-2	$\delta_n \sin\left(\frac{1}{8}kx\right) \sin\left(\frac{1}{8}ky\right) + \delta_n \sin\left(\frac{1}{4}kx\right) \sin\left(\frac{1}{4}ky\right) + \delta_n \sin\left(\frac{1}{2}kx\right) \sin\left(\frac{1}{2}ky\right)$
MA-3	$\delta_n \cos\left(\frac{1}{8}kx\right) \cos\left(\frac{1}{8}ky\right)$
MA-4	$\delta_n \sin\left(\frac{1}{8}kx\right) \sin\left(\frac{1}{8}ky\right) + \delta_n \sin(2kx) \sin(2ky)$

**Table 6.5:** Perturbations on macro-scale.

Case MA-1 represents the presence of a coherent structure with a length-scale equal to the full computational domain. Case MA-2 represents the presence of coherent structures of different length-scales, where the largest length-scale equals the size of the computational domain. Case MA-3 is meant to investigate, in a simple manner, the influence of a phase-shift of the coherent structure compared to the case MA-1. This phase-shift can be calculated thanks to the periodic boundaries. The disturbance of case MA-4 is a superposition of the macro-scale disturbance and a meso-scale disturbance.

### 6.2.3 Results

With the LES, we are able to compare the differences for all the seven types of disturbances, for all the five intensities  $\delta_n$ .

#### Micro-scale disturbances

Fully according to the theories as presented in the first chapter, after some time a merging-process takes place, while during this process vortices with larger length-scales are formed. An example of such a process is given in Figure 6.3. The amplitude of the vorticity, given by the colorbar besides each plot, indicates that enstrophy is lost during the merging-process.

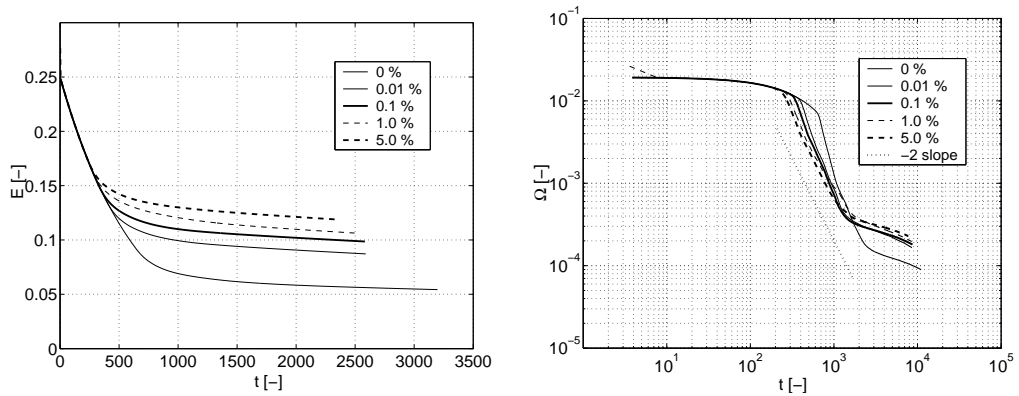


**Figure 6.2:** Development in time of energy (on the left) and enstrophy (on the right) for the MI-case.

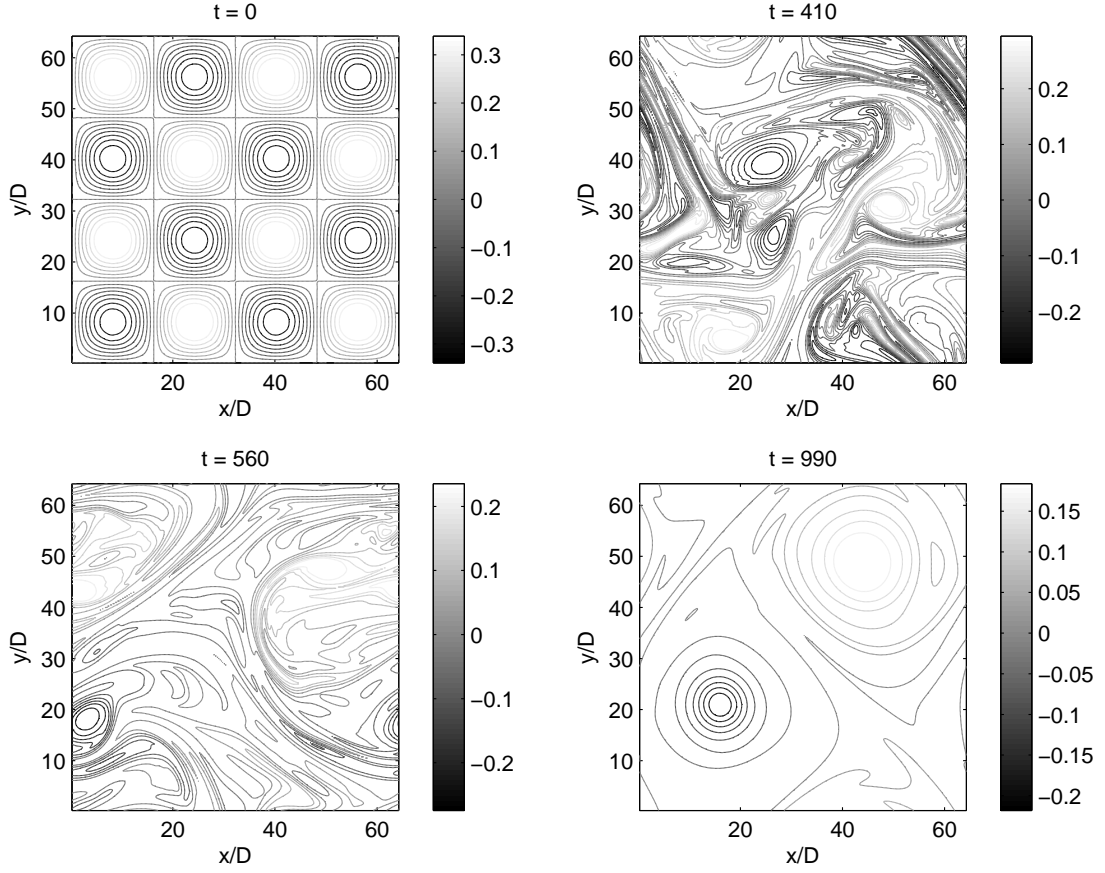


**Figure 6.3:** Merging-process of a  $4 \times 4$  vorticity-checkerboard in a  $64D \times 64D$  domain, with disturbance 0.1 %, in lexicographic ordering. This figure clearly shows the principle of self-organisation.

A good indicator to use for a mutual of the results, is the development of the amount of turbulent kinetic energy ( $E = \frac{1}{2}u'^2 + \frac{1}{2}v'^2$ ) and the amount of enstrophy ( $\Omega = \frac{1}{2}\omega_z'^2$ ) in time. The results for the MI-case, for all intensities  $\delta_n$  are given in Figure 6.2. In this figure, it is clear that the local disturbances do have a certain influence on the development of the coherent structures in time. It is observed that each case leads to merging of the vortices, the zero-disturbed case included. This zero-disturbed case should theoretically not merge, but it does due to truncation errors. Generally, it can be said that the larger the disturbance, the sooner the merging-process starts.

Noticing that the bend in the energy-curves is associated with the merging-process, Figure 6.2 shows that, as stated in the first chapter, the (formed) large-scale motions are weakly dissipative: the slope in the energy-curves for large  $t$ -values is much smaller than in the beginning (small  $t$ -values).

The enstrophy-plot in Figure 6.2 clearly shows a  $-2$ -slope, which can be recognised as a sign of two-dimensionality, as already described by Batchelor (1969) and observed in experiments (e.g. Uijttewaal & Jirka (2003)). The  $t$ -range where this  $-2$ -slope holds, is associated with the occurring merging-process, where again it is visible that the larger the disturbance, the earlier the merging-process sets in.

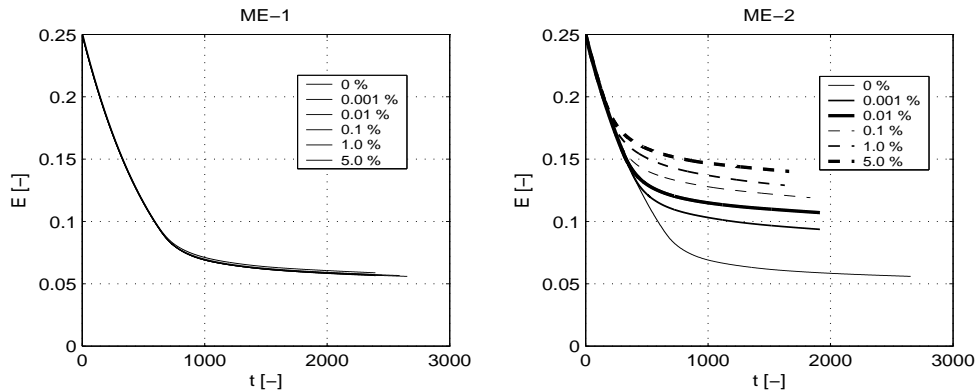


**Figure 6.4:** Development in time of energy in the ME-1-case (on the left) and in the ME-2-case (on the right).

### Meso-scale disturbances

In the cases ME-1 and ME-2, coherent structures with length-scales of  $8D$  and  $48D$  are imposed as perturbations, to see what the influence is on the development of the initial  $8 \times 8$  checkerboard, when these perturbations have, in the first case, a smaller length-scale than the already present vortices, and in the second case, a larger length-scale than the already present vortices. The results of the development of the energy in time is given in Figure 6.4. Here we restrict ourselves to information about only energy, not the enstrophy.

Figure 6.4 clearly shows (on the left), that perturbing the initial vorticity-checkerboard with coherent structures with length-scale equal to half the initial original coherent structures (the ME-1-case), does not make any sense, even stronger, the effect of the disturbances is fully vanished. The ME-2-case, however, shows that a perturbation on larger length-scales than the original ones, does make sense. Also the influence of the disturbances is clearly visible.

When comparing Figure 6.4 with Figure 6.2, it turns out that the two different kinds of perturbing the initial field (MI and ME-2) do not make much difference.

### Macro-scale disturbances

The cases MA-1 until MA-4 have one common similarity: all the cases contain at least perturbations on the maximal possible length-scale, namely a length-scale of the order of the size of the computational domain. The MA-disturbances are variations on this theme.

Again, we restrict ourselves here on the representation of the development of the energy in time, for each perturbation. The results are given in Figure 6.5.

The most important observation from Figure 6.5 is that the vortices in the cases MA-1 and MA-2 are most eager to merge. In principle, we can share the MA-4-case among these cases. But, the curves from the MA-4-plot are exactly the same as the curves from the MA-1-plot. This observation is fully consistent with the ME-1-plot, which shows that the perturbation with a  $\sin(2kx) \sin(2ky)$ -term does not make any sense. The MA-3-plot shows that a phase-shift equal to  $\frac{1}{2}\pi$  has a significant influence compared to the MA-1-plot: more energy is dissipated.

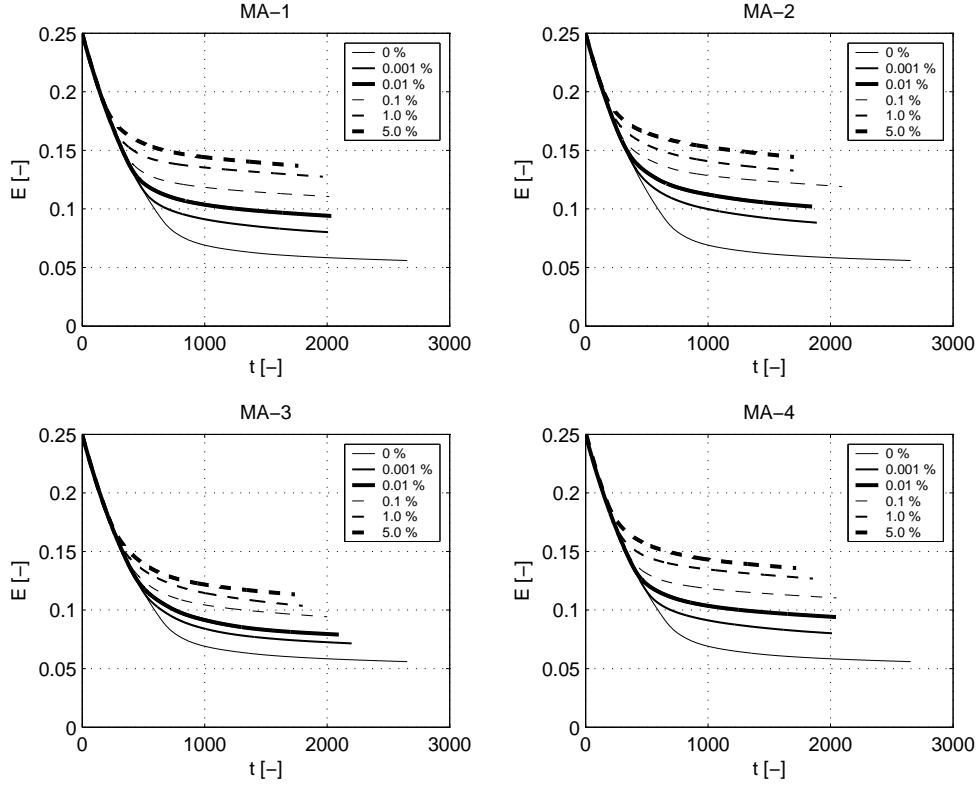


**Figure 6.5:** Development in time of energy in the MA-cases.

### Comparison of the three types of perturbations

Now we have perturbed the initial vorticity-checkerboard in three different ways, i.e. on three different length-scales, we are able to compare the results and see which perturbation has the strongest effect. On the basis of the development of the coherent structures (in the sense of the merging-process) and the development of the energy (and enstrophy) in time, we are able to make some remarks with regard to the different effects of the perturbations.

Firstly, it is observed that when perturbing the initial field on a length-scale larger than the length-scale of the initial vortices ( $16D$ ), the initial vortices immediately start merging. The explanation for this is, that these perturbations lay a direct connection between two or more vortices, which make merging significantly more easy. This process becomes most visible, when an initial  $8 \times 8$  checkerboard is covered with a perturbation of a  $4 \times 4$  checkerboard. In this case, the original checkerboard will immediately merge into a  $4 \times 4$  checkerboard, the configuration of the perturbation. This explains why the MA-2-setting is most prone to merging. After all, this case covers the initial vorticity-field with a  $4 \times 4$  checkerboard, and a  $2 \times 2$  checkerboard and a  $1 \times 1$  checkerboard. With other words: all connections are made, be it in phase. Recalling our hypothesis, that the sooner the energy is transferred to the larger length-scales, the smaller is the dissipation of turbulent kinetic energy, the observation from Figure 6.5, that the case that is most prone to merging (MA-2) reveals the largest conservation of initial present kinetic energy, affirm this hypothesis. This also explains the success of the ME-2-case, where the length-scale of the perturbation

is an odd multiple of the length-scale of the initial vortices and therefore makes the connection between relative many vortices compared to even multiple equivalents as given in the other cases, and the restricted success of the MA-3-case. Despite the fact that, due to the periodic boundaries, the perturbation in this case has a length-scale equal to the size of the computational domain, the effect is apparently not noticeable beyond these periodic boundaries.

Secondly, as we have observed, that the large-scale perturbations have a stronger effect on the merging-process than the local perturbations, we are interested in the development of the amount of energy for two cases, namely the MI-case (least eager to merge) and the MA-2-case (most eager to merge). To come to a sound analysis, we first introduce a new quantity, namely the dissipation of energy,  $\epsilon(t)$ :

$$\epsilon(t) = \frac{d(E(t_0) - E(t))}{dt} = -\frac{dE(t)}{dt}.$$

Now the MI-case and the MA-2-case should be compared, only for the  $\delta_4$ -disturbance, to keep the comparison orderly. Here, in both cases, the streamfunction is disturbed for 1%.

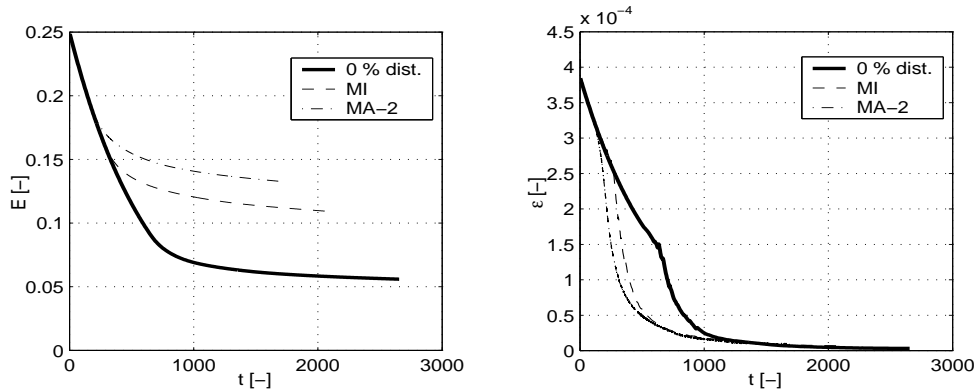


**Figure 6.6:** Development in time of energy (on the left) and the dissipation of energy (on the right) in the MI-case and MA-2-case, for 1% disturbance.

Figure 6.6 shows the development of energy and the dissipation of energy for the two cases to make a mutual comparison possible. It is now obvious that a perturbation of only 1% has large consequences for the development of energy in time. From the calculations, it is clear that the vortices in the MA-2-case merge the earliest, namely almost immediately. When we keep this in mind, while looking at the dissipation-plot of Figure 6.6, we see that, as soon as larger length-scales are formed, the dissipation becomes much lower. Hence, an affirmation of our hypothesis is found, that the perturbation on supra-depth length-scales have a large influence on the development of the flow as well as the dissipation of turbulent kinetic energy.

Thirdly, carrying on with our second point, it is remarkable that the differences between the effects of the local perturbation MI and the large-scale perturbation MA-2 are not very big. Our explanation is found in the observation of the development of the vortices that the small-scale perturbations are rather quickly dissipated away. As a result of this quick dissipation, the vortex as a whole becomes less stable. Rather paradoxically, it can therefore be stated that the small-scale perturbations themselves as *small-scale* perturbations have not so much an influence, but, however, as *large-scale* perturbations they have.

### 6.3 Spatial development of coherent structures

In the previous section the *temporal* development of coherent structures was investigated. This investigation led us to the conclusion that large-scale perturbations are of large importance with respect to the development of the initial field. To set this observation into a wider perspective, the *spatial* development of disturbed coherent structures is investigated. To that end, a grid at the inflow-boundary will be used to induce coherent structures. This inflow-boundary will also be used to disturb the flow, in order to get a good comparison with the data of the previous section.

#### 6.3.1 Numerical setup

The computational domain and the discretisation for the grid-flow-case are given in Table 6.6.

	$L_x$	$L_y$	$L_z$	$N_x$	$N_y$	$N_z$
2D	$60D$	$20D$	$D$	720	240	3
3D	$60D$	$20D$	$D$	720	240	16

**Table 6.6:** Lengths of the domain with the number of gridpoints in each direction, for the two-dimensional case and the three-dimensional case.

To represent the grid, a profile for the *streamwise* velocities  $u$ , as given in Figure 6.7, is put at the inflow-boundary, while the transverse velocities  $v$  are set on 0. By imposing a specific inflow-boundary, the periodic boundaries in the streamwise direction are not applicable anymore. Therefore, the Poisson-solver (within the pressure-correction algorithm) is modified. Now, only the boundaries in transverse direction are periodic.

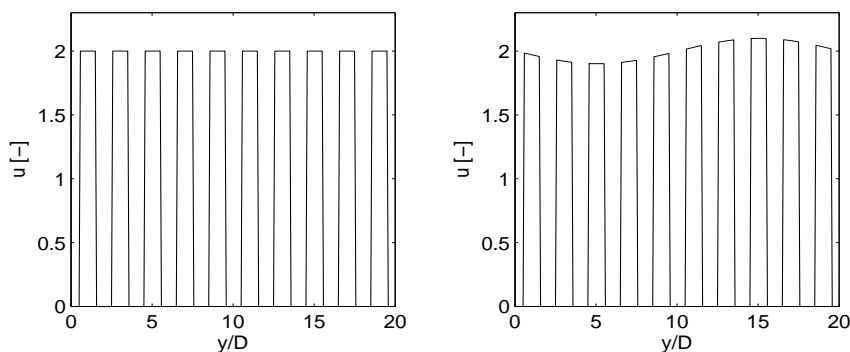


**Figure 6.7:** Distribution of streamwise velocities at the inflow-boundary representing the grid at the inflow. On the left, the unperturbed case, on the right, a perturbed case.

The streamwise velocity and transverse velocity elsewhere in the domain are set equal to 1 and 0, respectively, while the Reynolds-number  $Re$  is chosen to be equal to 500. This grid-flow setup will be calculated first with free-slip boundaries at  $z = 0$  and  $z = D$  (the 2D-case), and with a no-slip boundary (due to the rather low Reynolds-number) at  $z = 0$  and a free-slip boundary at  $z = D$  (3D-case).

### 6.3.2 Perturbations

While at the vorticity checkerboard the flow was perturbed by a superposition of coherent structures by means of the streamfunction, the grid-flow-case is now perturbed by multiplying the velocity profile with a sinusoidal function. Again, a set  $\delta_n$  is defined to be the set of different intensities of perturbing the inflow boundary (see Table 6.7).

$n$	$\delta_n$
1	0.01 %
2	0.1 %
3	1.0 %
4	3.0 %
5	5.0 %

**Table 6.7:** Values for  $\delta_n$ , representing the intensity of each disturbance.

Let  $k_y$  be the wavenumber corresponding to a wavelength equal to the size of the domain in transverse direction,  $k_y = \frac{2\pi}{L_y}$ , then, after combining two principles for perturbing the inflow boundary with the two Reynolds-numbers, the following (Table 6.8) cases will be calculated:

<i>Case</i>	2D/3D	<i>Re</i>	<i>Disturbance</i>
GD-1	2D	500	$\delta_n u(y) \sin(k_y y) \sin(k_y u_{max} t)$
GD-2	2D	500	$\delta_n u(y) \sin(\frac{1}{2} k_y y) \sin(\frac{1}{2} k_y u_{max} t)$
GD-3	3D	500	$\delta_n u(y) \sin(k_y y) \sin(k_y u_{max} t)$

**Table 6.8:** Grid-flow perturbations, with  $u(y)$  the inflow-profile and  $u_{max}$  the non-zero inflow velocity.

A  $\sin(k_y u_{max} t)$  -term is added, to give the perturbation also a disturbing effect in time, namely with a length-scale equal to the length-scale of the perturbation in space, using Taylor's hypothesis of frozen turbulence. The factor  $\delta_n$  can be considered as an amplitude in time and space. The case GD-3 is only computed for  $\delta_0$  (zero-disturbance) and  $\delta_4$  for computing-time reasons. The cases GD-1 and GD-2 are calculated for all  $\delta_n$ , except  $\delta_4$ .

### 6.3.3 Results

#### Vorticity patterns

Of four cases, the vorticity patterns are given in Figure 6.8. The pictures of this figure are taken after a long while, when the flow has fully developed. The first figure shows the development in space of a grid-flow without any disturbance at the inflow. It is clear that this flow is stable and not prone to merging. This observation is consistent with the observation at the vorticity-checkerboard from the previous section, where the flow was stable as well. The second figure from Figure 6.8 shows the development in space of a grid-flow with a disturbance at the inflow, namely the case GD-2 with a disturbance of 1%. From this figure, it becomes clear that the perturbation at the inflow has a significant influence on the spatial development of the flow. Consistent to what we saw in the previous section, large-scale coherent structures are formed after a while, here in a spatial sense: the length-scale of the coherent structures is growing with increasing distance from the inflow-grid.

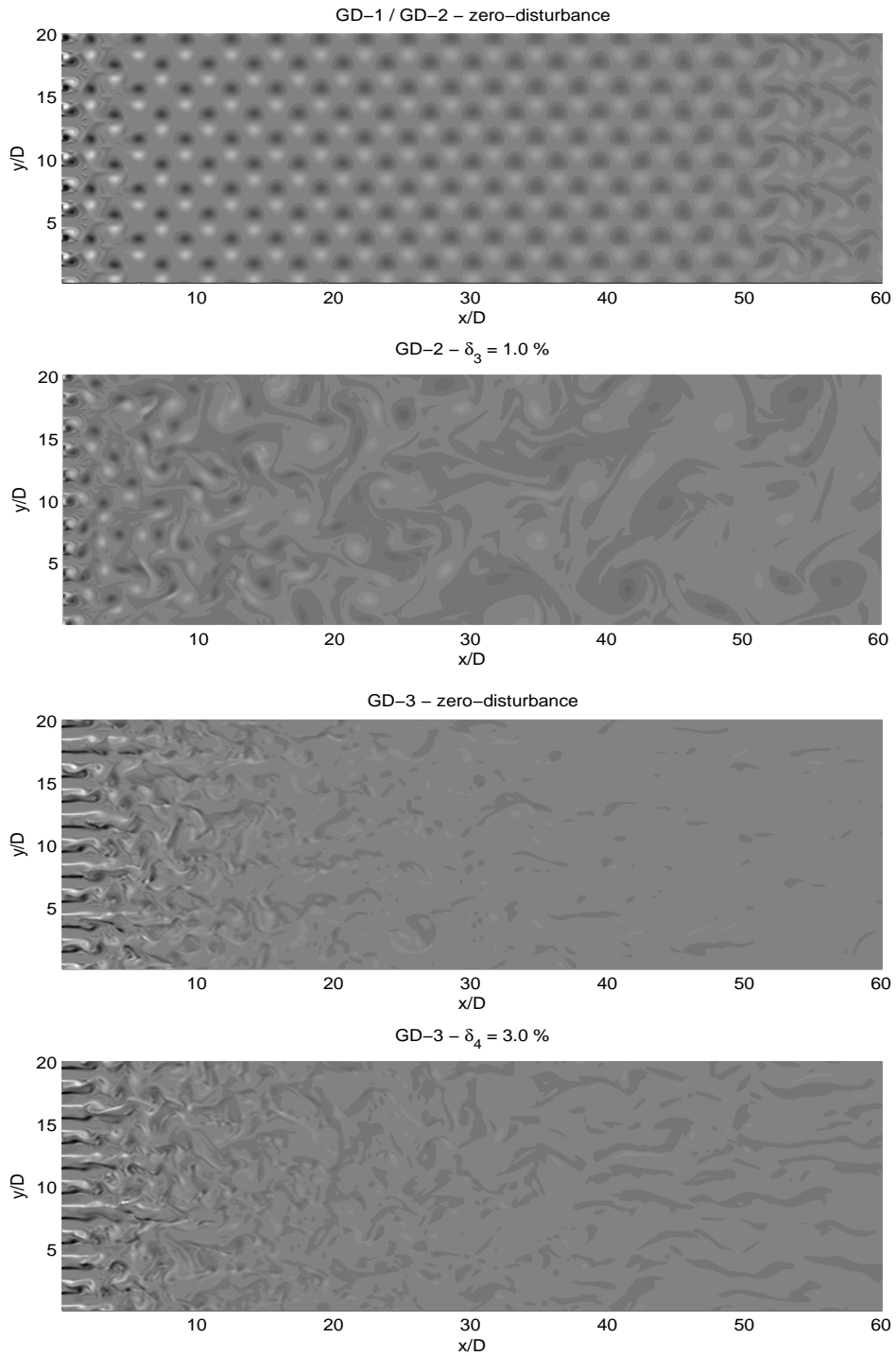


**Figure 6.8:** Two upper plots: vorticity patterns for the case GD-2 with  $\delta_0$  (upper plot) and  $\delta_3$  (lower plot). Two lower plots: vorticity patterns for the case GD-3 with  $\delta_0$  (upper plot) and  $\delta_4$  (lower plot), at  $z = D$ . Flow from the left to the right.

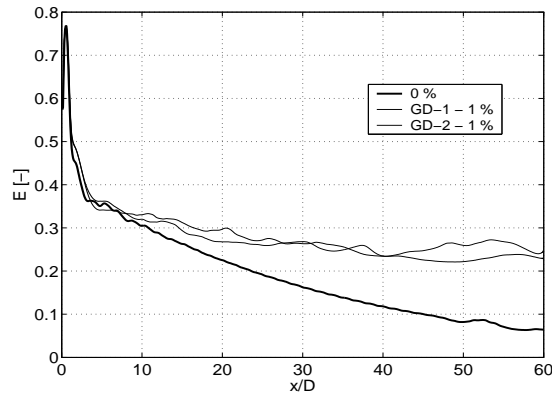


**Figure 6.9:** Development of turbulent kinetic energy in streamwise direction, for the undisturbed case and the cases GD-1 and GD-2 with 1% disturbance.

The GD-3 cases (3D) show different vorticity patterns. The patterns, as given in Figure 6.8, are observed at  $z = D$ , at the free surface. It is visible that in both cases, coherent structures are formed downstream of the obstacles. It is observed, that just after the start of the calculation, the development of the zero-disturbed GD-3 case was very similar to the development of the zero-disturbed GD-2 case. But after some time, three-dimensional effects start to play an important role. Therefore, the two-dimensional self-organisation principle is suppressed by the three-dimensionality of the flow. However, 2D-effects are still visible, be it less pronounced. After all, the development of to larger length-scale is, in some way, visible. But, considering that just after the beginning the development of the zero-disturbed GD-3 is similar to the zero-disturbed GD-2, it becomes clear that the presence of the bottom causes (large-scale) perturbations itself. After all, the differences between the undisturbed GD-3 case is very similar to the disturbed GD-3 case, be it somewhat less noisy, which can be associated with the fact that both the pictures from Figure 6.8 are just situations on an arbitrary moment.

### Energy and enstrophy

In order to gain more insight in the physical processes during the development from the initial length-scales to the larger length-scales, we focus on the development of turbulent kinetic energy and enstrophy as a function of  $x$ . The algorithm that is used to determine these curves, is described in Appendix C. The results for the development of turbulent kinetic energy is given in Figure 6.9.

Firstly, it should be noticed that the energy-curves for the different cases are the same. Therefore, in Figure 6.9 only the cases where  $\delta_3 = 1\%$  are shown, for clarity. Consistent with the observations done in the previous section, Figure 6.9 shows that the larger the length-scale of the coherent structure, the smaller is the amount of turbulent kinetic energy that is lost. Hence, the merging of vortices has conservative effects with regard to the conservation of energy. It is striking that each disturbance has the same clear effect. Apparently, the flow downstream of the grid is very sensitive to disturbances at the inflow boundary. In literature (see, for instance, Uijttewaal & Jirka (2003) and references therein), several characteristic slopes in the log-log-plot of the development of energy or enstrophy are found, namely a  $-1.3$  -slope for the energy-decay and a  $-2$  -slope for the enstrophy-decay. Therefore, our results for the energy and enstrophy as a function of  $x$  are plotted in a double-logarithmic plot, see Figure 6.10.

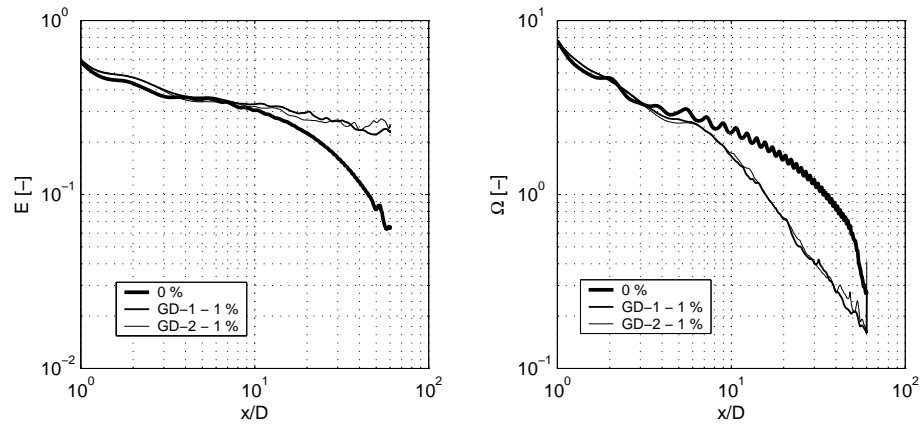


**Figure 6.10:** Development of turbulent kinetic energy (on the left) and enstrophy (on the right) in streamwise direction, for the undisturbed case and the cases GD-1 and GD-2 with 1% disturbance.

Figure 6.10 shows a logarithmic decay of both the energy and enstrophy: energy with a slope of about  $-1/4$  and enstrophy with a slope of about  $-6/4$ . These values have never been found in literature yet. It is questionable whether these values are general for real two-dimensional flows. But that question is not very relevant for our investigation: fact is that a little perturbation at the inflow has significant influence on the development of the flow. The fact that the energy-curves and enstrophy-curves of the GD-1 cases and the GD-2 cases coincide, indicates that the presence of a large-scale disturbance itself is more important than the length-scale on which it disturbs the flow.

Question is now, how the 3D-case develops in streamwise direction. The development of energy and enstrophy is given in Figure 6.11. Figure 6.11 makes clearly visible that imposing perturbations at the inflow boundary does not make sense, as the energy- and enstrophy-curves coincide. Having seen that in the 2D-cases the perturbations had large influence on the development of the flow, together with the observation that these perturbations have no influence in the 3D-case, makes clear that the bottom-induced perturbations are dominant above the inflow-perturbations. Hence, it is clear that, after a while, spectral distributions, as for example in chapter 4, have developed under influence of the bottom. When these spectral distributions have fully developed, large-scale bottom-induced coherent structures are present that can make the initial coherent structures merge. This stresses the need of a kinematic simulation in two-dimensional simulations, which represents the perturbations induced by the bottom.

Furthermore, Figure 6.11 shows that the development of energy follows a  $-1.3$ -slope quite well, while the development of enstrophy follows a  $-2$ -slope quite well. The occurrence of both slopes, the  $-1.3$ -slope and the  $-2$ -slope, is consistent with literature (e.g. Uijttewaal & Jirka (2003) and references therein) and can be recognised as a sign of two-dimensionality.

### Spectral distributions

When studying turbulence properties, a representation in terms of energy-density spectra gives an indication of the energy distribution over the various length- and time-scales. The process of energy decay can be interpreted from the shape of the spectrum. These spectra are given in Figure 6.12. Remembering that the size of the obstacles at the inflow-boundary equals  $D$ , the corresponding angular frequency  $\omega$  should equal

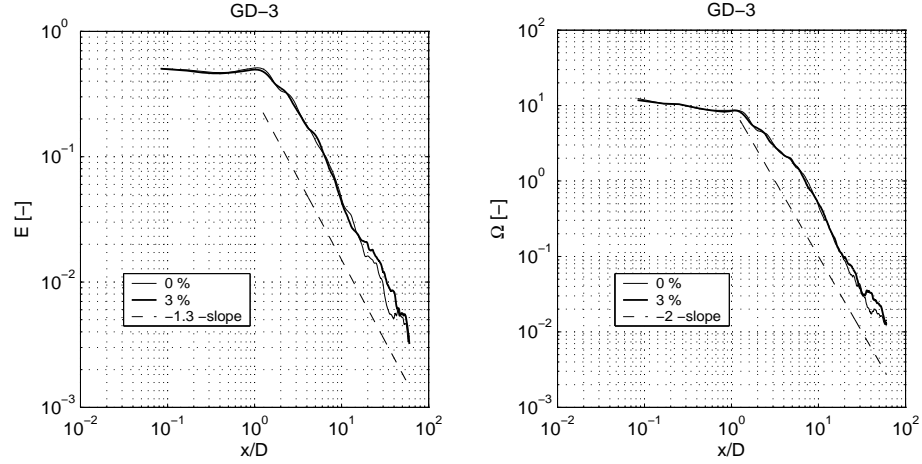


**Figure 6.11:** Development of turbulent kinetic energy (on the left) and enstrophy (on the right) in streamwise direction, for the case GD-3, measured at  $z = D$ .

$\pi$  in the near-field, using Taylor's hypothesis of frozen turbulence. This value  $\omega = \pi$  is found in Figure 6.12. Especially in the  $E_{vv}$ -spectra, the shift to the larger length-scales is well visible: the  $E_{vv}$ -spectrum in the far-field shows a peak-value at  $\omega \approx 1$ , while the  $E_{uu}$ -spectrum shows a peak-value at  $\omega \approx 0.4$ . Apparently, the coherent structures are elongated in streamwise direction, which is consistent with observations from chapter 4. On the basis of Figure 6.12, it is clear that the large-scale bottom-turbulence enforces a shift to the larger length-scales.

An interesting observation from Figure 6.12 is the presence of the  $-3$ -slope on the right side of the peak-value. This value is associated with the enstrophy-cascade, as inferred in chapter 2 (equation (2.29)). Other characteristic slopes ( $-5/3$  and  $-1$ ) are not observed, as these slopes occur in the rather small-scale parts of the spectrum, that are not well represented by an LES.

## 6.4 Conclusion

The calculations on the vorticity-checkerboard shows the importance of initially imposed large-scale perturbations. These perturbations force the initially present eddies to merge. It has been confirmed that the larger the length-scale of the resulting eddies, the lesser the loss of turbulent kinetic energy, with the consequence that the large-scale perturbations have a energy-conserving influence.

The calculations on the grid-flow provides us information on the spatial development of grid-induced coherent structures in shallow flows. The 2D-cases shows the importance of imposing perturbations at the inflow-boundary. In fact, these perturbations are essential to make vortex-merging possible. This vortex-merging, on its turn, has a conservative effect with regard to the conservation of turbulent kinetic energy. The energy-curves shows a  $-1/4$ -slope in the area where merging of eddies occurs, while in this area a  $-6/4$ -slope was observed in the enstrophy-curves. Mutual differences between the flows for several disturbances are not observed: the fact that the flow is disturbed is more important than the intensity of the disturbance.

The 3D-cases showed that the imposing of perturbations at the inflow-boundary had no longer importance

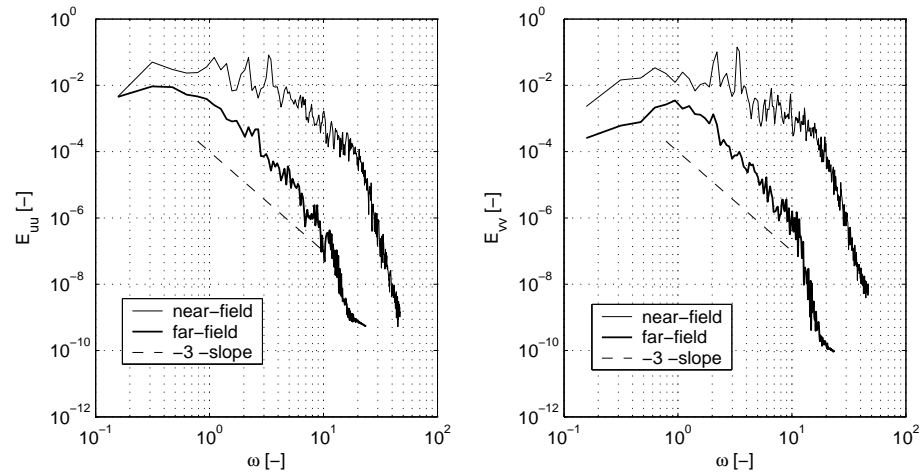


**Figure 6.12:** Energy-density spectra  $E_{uu}$  (left) and  $E_{vv}$  (right) measured in the near-field and the far-field of the 3D-LES.

with regard to the occurrence of a flow different from the stable vortex-field as seen in Figure 6.8 (most upper plot). Apparently, the bottom acts as a large-scale perturbation. This is consistent with the observations as done in chapter 4, where we saw that coherent structures with very large length-scales have a clear non-zero energy amount. The perturbations in the 2D-cases showed that just a little bit of energy is needed to create large-scale coherent structures. Furthermore, the 3D-cases showed a clear  $-1.3$ -slope in the energy-decay curves, while they showed a clear  $-2$ -slope in the enstrophy-decay curves. Both slopes are consistent with analyses and observations as done in literature. Hence, it is concluded that the large-scale bottom turbulence acts as a disturber and that therefore these large length-scales are the cause of the principle of self-organisation in quasi-two-dimensional flows. This shift to the larger length-scales is affirmed by the associated spectral distributions.



## Chapter 7

# Application of 2D-TRANS+ks

In the previous chapters, we gained, on the one hand, insights in the development of large-scale coherent structures influenced by perturbations on length-scale of the order of the water-depth, and, on the other hand, we formulated a strong basis for the application of the 2D-TRANS with kinematic simulation. In this chapter, we will apply the 2D-TRANS+ks on the grid-flow case, as already been calculated at in the previous chapter.

### 7.1 Background and objective

The 2D-TRANS+ks has already been tested for shallow mixing layers (see Van Prooijen (2003)), and was in this case found to be suitable to represent the mean flow well and the coherent structures reasonably: the mean velocities agreed well with the experiments, while the velocity-fluctuations and the Reynolds-stresses deviated strongly. Van Prooijen made in his discussion on the practical use of 2D-TRANS+ks some notions about the model, which should be made here as well. Firstly, the model as implemented here requires a grid that is aligned to the main flow direction. This assumption is also important for the implementation of the kinematic simulation in the shallow water equations (see also Appendix B:  $u_{fil} = u_{new}$ ). Secondly, as Van Prooijen compared the model results with experiments, he argued that the model does not contain vertical shear, which is an important mechanism in the real 3D world, as in the experiments. He argued that this mechanism should be accounted for in the model, for instance, by means of a multi-layered model. Considering the restricted size of our research, no attention is paid to the construction of a multi-layered model with kinematic simulation. Thirdly, in Van Prooijen (2003), only the mechanism of *internal instabilities* (see chapter 2) was considered, while no attention was paid to the mechanism of *topographical forcing*. In our grid-flow case, there is a matter of the latter mechanism. However, considering the domain size that will be used in this chapter (namely  $120D \times 40D \times D$ ), the mechanism of internal instabilities will be far dominant above the mechanism of topographical forcing. In any case, there *is* topographical forcing, so, we will see what the influence will be.

Being conscious of these notions, in this chapter we will carry out calculations with the 2D-TRANS+ks model and compare these results with the results of a full 3D-LES of the same case. In this way, we can investigate the similarities and differences between the two models. If there is a mutual agreement observable between the two models, the advantage would be that expensive 3D-LES calculations can be replaced by much cheaper 2D-TRANS+ks methods.

## 7.2 Numerical setup

### Computational domain

Three cases will be calculated, taking  $Re_\tau = 590$  as the governing flow-parameter, namely a 2D-TRANS *without* kinematic simulation, a 2D-TRANS *with* kinematic simulation and a 3D-LES.

In Van Prooijen (2003) it is argued that for the proper representation of coherent structures with length-scale equal to twice the water depth, a discretisation of  $D/3$  is needed. We, therefore, choose  $dx = dy = D/3$ .

Hence, we come to the following domain settings for the 3 cases (Table 7.1):

<i>Case</i>	<i>Type</i>	$L_x$	$L_y$	$L_z$	$N_x$	$N_y$	$N_z$
A	2D-TRANS	$120D$	$40D$	$D$	360	120	3
B	2D-TRANS+ks	$120D$	$40D$	$D$	360	120	3
C	3D-LES	$120D$	$40D$	$D$	720	240	16

**Table 7.1:** Lengths of the domain with the number of gridpoints in each direction.

The values of  $\alpha$ ,  $\beta$  and  $\lambda$  for the kinematic simulation are chosen to be equal to 1.3, 3.0 and 0.4 respectively. For the bottom friction coefficient  $c_f$  the value 0.003 is used (see Appendix B). Using 10 obstacles at the inflow (see Figure 6.7), the width of an obstacle is  $2D$ .

### Boundary conditions and initial conditions

The inflow-boundary of the cases A and B is the same as in the previous chapter. Initially, the velocities at the inflow boundary are 0 or  $37u_\tau$ , and  $\frac{1}{2} \cdot 37u_\tau$  elsewhere in the domain. In case C, we use equation (3.39) with  $n = \frac{1}{7}$  and  $u_{max} = 42u_\tau$ . The value  $37u_\tau$  arises from averaging the inflow-profile of case C. In case C, we use (3.39) with  $n = \frac{1}{7}$  and  $u_{max} = 21u_\tau$  elsewhere in the domain. But, in principle, this is not of any relevance, as the flow has to establish itself a while, in any case.

The bottom of cases A and B is chosen to be free-slip, while the bottom of cases C is chosen to be partial-slip (i.e. free-slip with wall-function). Again the velocities are scaled with the friction-velocity  $u_\tau$ .

## 7.3 Results

Some results of the calculations are shown in Figure 7.1. The figure from the 3D-LES is measured at the free surface ( $z = D$ ). The upper plot shows the merging behaviour of the coherent structures, probably due to numerical errors and/or the presence of a friction term in the shallow water equations (5.19) and (5.20). The 2D-TRANS+ks shows, on eye, good resemblance with the results from the 3D-LES. To what extent this is true, is investigated in this section.

### Validation

In principle, the profile of the streamwise velocities  $u$  in the far-field should be approximately similar to the streamwise velocities profile of the channel flow. To that end, this profile is calculated and compared with the DNS data of Moin, Kim and Mansour (1999) (see Figure 7.2).

Figure 7.2 shows that the differences between the MKM-data and the grid-flow-data are sufficiently small.

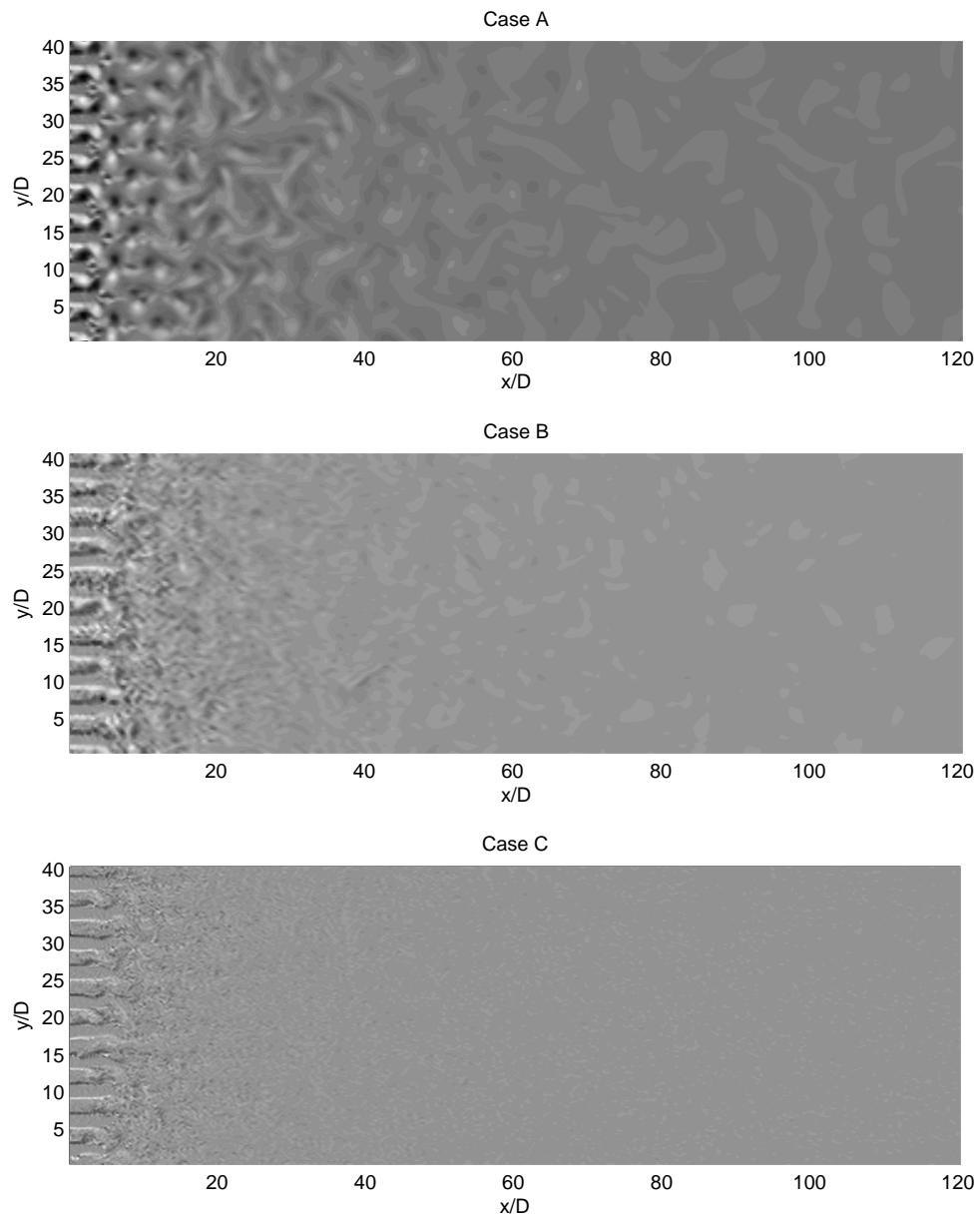


**Figure 7.1:** Vorticity patterns for the cases A (2D-TRANS), B (2D-TRANS+ks) and C (3D-LES).

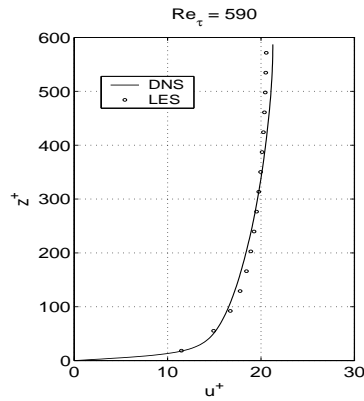


**Figure 7.2:** Profile of the streamwise velocities in the far-field of the grid-flow.

### Influence of disturbances

As we calculated case C for two different disturbances, namely 0% and 3%, we investigate the influence of these disturbances. We saw in the previous chapter, that these disturbances have no longer influence, since the flow is three-dimensional with a bottom. So, this calculation is just a test for affirmation of this observation.

Figure 7.3 shows the result of the comparison of the both disturbances. Again, it is visible that the disturbances at the inflow-boundary have no influence at all: both the curves fully coincide. The figure also shows that the  $-1.3$ -slope in the energy-curve is less pronounced visible compared to Figure 6.11. The  $-2$ -slope in the enstrophy-curve is, however, well visible.

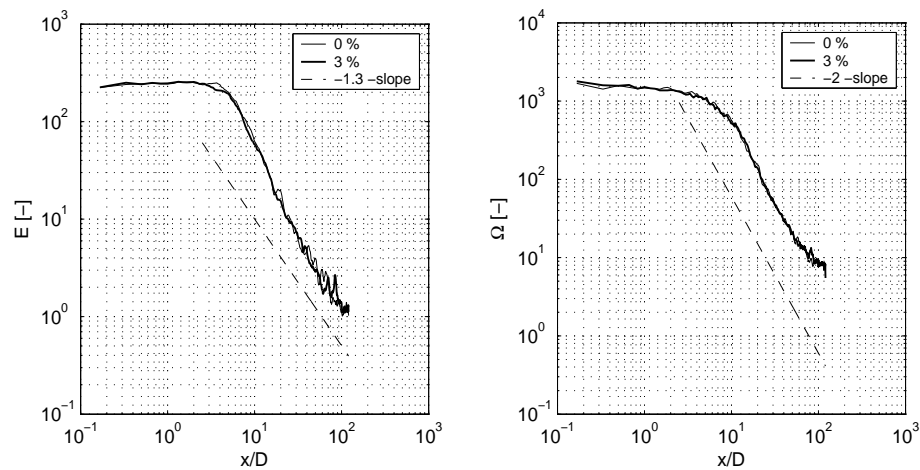


**Figure 7.3:** Development of turbulent kinetic energy and enstrophy in streamwise direction for case C at two different disturbances, measured at  $z = D$ .

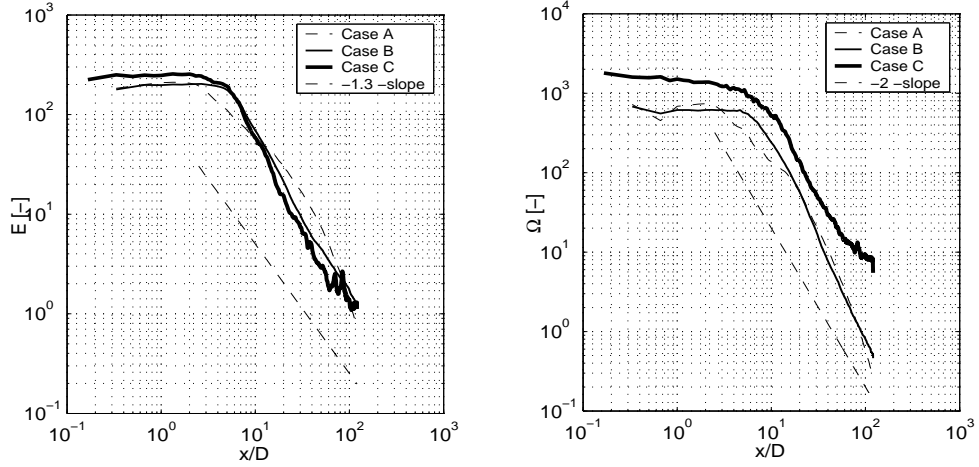


**Figure 7.4:** Development of energy (left plot) and enstrophy (right plot) in streamwise direction. Results for case C is determined at the free surface.

### Comparison of decay of energy and enstrophy

Now the question is, to what extent the two-dimensional model with kinematic simulation produces the same output as the 3D-LES. To speak in terms of Table 7.1, the cases A/B (without/with kinematic simulation) are compared with case C. To that end, again, only the development of energy and enstrophy in streamwise direction is determined. It is clear that many quantities can be used in order to come to a good comparison of the data. We restrict ourselves, however, to only these two quantities. These two quantities are, in case C, measured in three different ways: 1. using the velocity map at the free surface ( $z = D$ ), 2. using the velocity map where  $\bar{u} \approx 18.5$  (equal to the used velocity in the cases A and B), and 3. using depth-averaged velocity maps. These three cases are referred to as cases C1, C2 and C3 respectively. The differences of the cases C1, C2 and C3 are found in the fact that case C3 contains the lowest amount of energy, while cases C1 and C2 contain, more or less, equal amounts. This is explained by the fact that during the depth-averaging operation energy is lost. The results are given in Figure 7.4, where only the cases A, B and C1 are given.

For the enstrophy-curves, the  $-2$  -slope is again observed, in each case, which is a sign of the two-dimensionality of the flow. The  $-1.3$  -slope in the energy-curves is not very pronounced: the energy decays somewhat faster.

When comparing the cases A and B, it is visible that the energy-curves show a different development, while the enstrophy-curves are almost similar, except in the near-field. Apparently, the presence of the kinematic simulation does not much affect the development of enstrophy far from the grid. The energy-curve of case B, however, resembles the energy-curve of the 3D-LES much better, in particular when the energy, in case C, is measured at the free surface.

Striking fact is that case A shows merging of vortices and a clear shift of the length-scale of the eddies to larger length-scales. In principle, this case should not show merging, because of the absence of disturbances. Apparently, numerical errors function as a disturber. Moreover, it can be due to the presence of a friction term in equations (5.19) and (5.20), which was absent in the original Navier-Stokes equations, that were the basis of our investigation in the previous chapters.

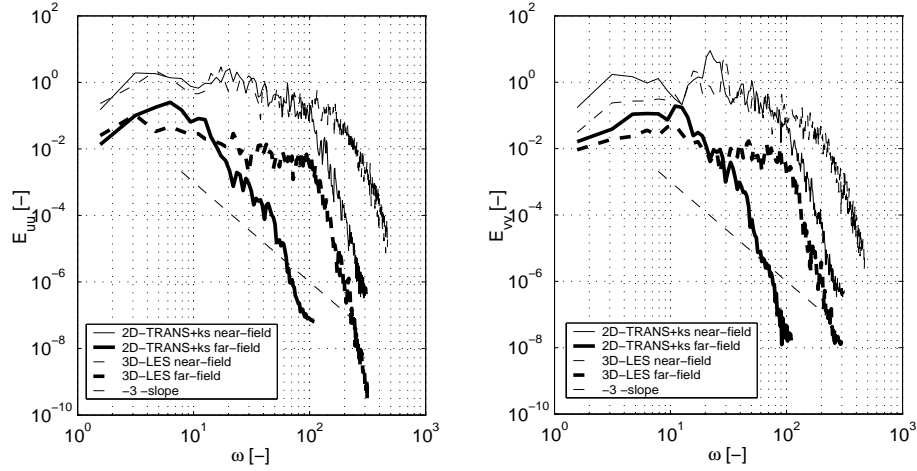


**Figure 7.5:** Energy-density spectra  $E_{uu}$  (left) and  $E_{vv}$  (right) measured in the near-field and the far-field for the 2D-TRANS+ks and the 3D-LES.

Figure 7.4 shows that the energy-curve of the 3D-LES is well simulated by the 2D-TRANS+ks. Contrary to this similarity, the enstrophy is underestimated by the 2D-TRANS+ks. But still information about the presence of large-scale motion is absent. For the detection of very-large-scale motion, the energy-density spectra are needed.

### Spectral distributions

In Figure 7.5, the spectral distributions of energy for the 2D-TRANS+ks and the 3D-LES are given. A peak-value of the spectra is found at  $\omega \approx 28$ , which is consistent with the given size of the obstacles ( $2D$ ) and Taylor's hypothesis of frozen turbulence. The location of the peak-value is shifted to the small-frequency side of the spectrum. This, again, indicates that the self-organisation principle of the quasi-two-dimensional flow is present again: energy is transferred to the larger length-scales. The  $-3$ -slope, however, indicating the enstrophy-cascade, is not clearly visible in this case.

When comparing the results of the depth-averaged simulation with the full three-dimensional LES, it turns out that the large-scale side of the spectra are simulated quite well, although the transverse velocities tend to an overestimation of the energy amount. Length-scales smaller than the forcing length-scale  $2D$  are, however, not very well represented in the far-field.

## 7.4 Conclusion and discussion

With a 3D-LES as a reference, it can be concluded that the 2D-TRANS+ks performs rather well for the simulation of the flow downstream of a grid of obstacles: the energy-curves are almost similar, but the enstrophy-curves are strongly underestimated. The energy-curves and the enstrophy-curves show, more or less, similarities with characteristic slopes from the literature, namely the  $-1.3$ -slope for energy, and the  $-2$ -slope for enstrophy. These slopes are characteristic for quasi-two-dimensional turbulence, which has the shift to the large length-scales as its signature. Also considering that the large-scale part of the

energy-density spectra are simulated quite well, it can be inferred that the 2D-TRANS+ks model performs reasonably well in the investigated grid-flow.

The difference between the 2D-TRANS *without* kinematic simulation and the 2D-TRANS *with* kinematic simulation makes clear that the kinematic simulation adds substantial information to the calculation: from the beginning the initial large-scale coherent structures have their influence, while this influence is absent in the model without kinematic simulation. In spite of this absence, the flow shows merging after some time, which might be the result of numerical errors due to the rather coarse resolution or to the different equations that are solved. Van Prooijen (2003) observed, studying shallow mixing layers, that the bare 2D-TRANS model showed a small mixing layer width-growth rate, compared to his experiments and 2D-TRANS+ks model. This observation, together with our observations of the grid-flow, gives rise to the conclusion that the 2D-TRANS model without kinematic simulation cannot simulate the three-dimensional dynamics sufficiently accurate and is too insecure to reckon on. Addition of the kinematic simulation, however, makes the model more predictable, while representing the physical properties of the flow more appropriately.

However, the 2D-TRANS+ks model has still some clear disadvantages. The most important disadvantage is that it can only handle rectangular computational domains, as it is based on a channel flow, also considering that use of the channel flow properties on flows other than channel flows is rather doubtful itself. Hence, the collection of flow setups that are eligible for a treatment with 2D-TRANS+ks is rather small.



## Chapter 8

# Conclusions and recommendations

### 8.1 Overview

Large-scale coherent structures in shallow flows have been investigated with the aim of developing better insights in the development of coherent structures to larger length-scales under influence of disturbances and under influence of the bottom. Within this context, it is tried to get an answer on the question to what extent the bottom acts as a disturber itself.

To that end, spectral analyses of a channel flow have been carried out in order to see how the turbulent kinetic energy is distributed over the present wavenumber-range as a function of the Reynolds-number. Moreover, the temporal and spatial development of coherent structures is investigated using a checkerboard of vortices and the flow downstream of a grid of obstacles at the inflow-boundary of a channel flow, in 2D, as well as in 3D. The obtained insights have been used in a two-dimensional TRANS model, enriched with a kinematic simulation, representing the bottom-induced turbulence.

### 8.2 Conclusions

The spectral analysis of the channel flow of chapter 4 resulted in a huge database which can be used for the modelling of large-scale coherent structures using two-dimensional energy-density spectra of shallow flows in rectangular computational domains (chapter 5). For all the three used Reynolds-numbers, it became, moreover, clear that the small-scale turbulence is found near the bottom, while the length-scales of the most energetic eddies increase with the distance to the wall. Moreover it has been observed that the large-scale coherent structures become less energetic with increasing Reynolds-number.

The investigation on the influence of disturbances in chapter 6 lead to the insight that imposing large-scale perturbations is of large importance with regard to the genesis and development of very-large length-scales. Without any perturbation, no shift to the larger length-scales has been observed. The three-dimensional case showed that the presence of the bottom acts as a large-scale disturber, which pushes the present coherent structures to larger length-scales. This has been proved by the presence of certain slopes in the energy-curves and enstrophy-curves, which are characteristic for quasi-two-dimensional turbulence with its characteristic shift of coherent structures to larger length-scales. This shift to the larger length-scales was also visible in spectral distributions.

These insights have been used in practical model by representing the large-scale bottom-induced turbulence

in a two-dimensional depth-averaged model (chapter 5). This model (2D-TRANS+ks) has been tested on a channel flow with a grid of obstacles at the inflow boundary (chapter 7). The application of the 2D-TRANS+ks showed rather good agreement with a 3D-LES, which has been carried out for reference, with special focus on the development of turbulent kinetic energy, enstrophy and the spectral distributions. It was found that the development of coherent structures was rather well simulated, but that the deviations between the 3D-LES and the 2D-TRANS+ks are sometimes visible in underestimated (enstrophy) and overestimated quantities (spectral densities). Therefore, in future, a 2D-TRANS+ks should be applied with care. But, the differences between the 2D-TRANS+ks model and the bare 2D-TRANS model showed that addition of the kinematic simulation is a good step forward to make the 2D-TRANS model represent 3D flows more appropriately.

### 8.3 Recommendations

In chapter 4 we observed an evolution of the coherent structures to larger length-scales with increasing distance from the wall. In literature, e.g. Kim & Adrian (1999), much larger dominant large-scale coherent structures have been observed, while this shift has not been observed so strongly in results of this present research. The difference between these cases is the fact that Kim & Adrian (1999) dealt with 3D-flows and that this research dealt with quasi-2D-flows. This difference makes curious to the influence of shallowness on the evolution of large-scale motions near a solid wall. It is good to investigate the differences between these kinds of flows with the focus on the growth of large-scale motions with increasing distance from the wall.

During the investigation on the grid-flow, some physical phenomena are left out of consideration, for instance, the presence of a boundary layer besides the inflow-obstacles, the presence of sideward walls and the presence of an hydraulic rough bottom. With some small calculations (results not shown in this report), it was seen that the presence of a boundary layer at the inflow-obstacles have an effect on the development of the flow. No attention was paid to this subject during this research. It would be interesting to investigate the influence of these issues on the development of the flow and the need for disturbances. Comparison of the data with comparative data as found in Uijtewaal & Jirka (2003) would give extra insight in the physical correctness of the used models.

Furthermore, some recommendations can be given with regard to the 2D-TRANS+ks model. In the first place, the model should be extended to more general flow geometries, as the channel flow and its characteristics as basis are too restrictive to make the model useful for civil engineering applications. Secondly, the formulated multi-layered model should be tested, in future. This extension to more layers might make the 2D-TRANS+ks model perform better. Perhaps, in this way, three-dimensional effects can, be it possibly to a small extent, be represented.

# Bibliography

- Batchelor, G. K. (1969). Computation of the energy spectrum in homogeneous two-dimensional turbulence. *Phys. Fluids Suppl. II*, 233–239.
- Del Alamo, J. C. and J. Jimenez (2003). Spectra of the very large anisotropic scales in turbulent channels. *Physics of Fluids 15-6*, L41 – L44.
- Fung, J. C. H., J. C. R. Hunt, N. A. Malik, and R. J. Perkins (1992). Kinematic simulation of homogeneous turbulence by unsteady random fourier modes. *J. Fluid Mech.* 236, 281–318.
- Hinterberger, C. (2004). *Dreidimensionale und tiefengemittelte Large-Eddy-Simulation von Flachwasserströmungen*. PhD dissertation, Universität Karlsruhe.
- Jimenez, J. (1998). The largest scales of turbulent wall flows. *Center for Turbulence Research - Annual Research Briefs*, 137 – 154.
- Jirka, G. H. (2001). Large scale flow structures and mixing processes in shallow flows. *Journal of Hydraulic Research 39-6*, 567 – 573.
- Jirka, G. H. and W. S. J. Uijttewaal (2004). Shallow flows: a definition. *Proceedings of the International Symposium on Shallow Flows*.
- Kim, K. C. and R. J. Adrian (1999). Very large-scale motion in the outer layer. *Physics of Fluids 11-2*, 417–422.
- Kolmogorov, A. N. (1941). *Dokl. Akad. Nauk SSSR* 30, 299.
- Kraichnan, R. H. (1967). Inertial ranges in two-dimensional turbulence. *Phys. Fluids* 10, 1417–1423.
- Moser, R. D., J. Kim, and N. N. Mansour (1999). Direct numerical simulation of turbulent channel flow up to  $re_\tau = 590$ . *Physics of Fluids 11-4*, 943 – 945.
- Nieuwstadt, F. T. M. (1998). *Turbulentie*. (in Dutch), Epsilon Uitgaven Utrecht.
- Nikora, V. (1999). Origin of the -1 spectral law in wall-bounded turbulence. *Phys. Rev. Lett.* 83, 734–736.
- Piomelli, U. and E. Balaras (2002). Wall-layer models for large eddy simulations. *Annu. Rev. Fluid Mech.* 34, 349–374.
- Piomelli, U. and E. Balaras (2003). The inner-outer layer interface in large-eddy simulations with wall-layer models. *Int. Journal of Heat and Fluid Flow* 24, 538 – 550.
- Pope, S. B. (2000). *Turbulent flows*. Cambridge University Press.
- Sagaut, P. (1998). *Large Eddy Simulation for Incompressible Flows*. Springer Verlag.
- Schumann, U. (1975). Subgrid scale model for finite difference simulations of turbulent flows in plane channels and annuli. *Journal of Computational Physics* 18, 376–404.

- Squires, K. D. (2004). Detached-eddy simulation: current status and perspectives. *Proceedings of Direct and Large-Eddy Simulation-5*.
- Uijttewaal, W. S. J. and G. H. Jirka (2003). Gridturbulence in shallow flows. *J. Fluid Mech.* 489, 325–344.
- Van Heijst, G. J. F. (1993). Self-organisation of two-dimensional flows. *Ned. Tijdschrift voor Natuurkunde* 59, 321–325.
- Van Prooijen, B. (2003). *Shallow mixing layers*. PhD dissertation, Delft University of Technology.
- Wesseling, P. (2001). *Principles of computational fluid dynamics*. Berlin: Springer Verlag.

# Appendix A

## List of calculations

In this report, the results of many calculations are presented. In Table A.1, the calculations are listed.

Chapter	$L_x$	$L_y$	$L_z$	$N_x$	$N_y$	$N_z$	$Re$	$Re_\tau$	Bottom	Periodic
4	$80D$	$80D$	$D$	1024	1024	16		395	wall-function	in $x$ - and $y$ - dir.
4	$80D$	$80D$	$D$	1024	1024	16		590	wall-function	in $x$ - and $y$ - dir.
4	$80D$	$80D$	$D$	1024	1024	16		1000	wall-function	in $x$ - and $y$ - dir.
6	$128D$	$128D$	$D$	512	512	3	100		free-slip	in $x$ - and $y$ - dir.
6	$60D$	$20D$	$D$	720	240	3	500		free-slip	in $y$ - dir.
6	$60D$	$20D$	$D$	720	240	16	500		no-slip	in $y$ - dir.
7	$120D$	$40D$	$D$	360	120	3		590	free-slip	in $y$ - dir.
7	$120D$	$40D$	$D$	720	240	16		590	wall-function	in $y$ - dir.

**Table A.1:** List of calculations.

Two remarks should be done after Table A.1. Firstly, all calculations are carried out by means of an LES, except the first one of chapter 7. Those calculations is carried out with a 2D-TRANS, with and without kinematic simulation (2D-TRANS+ks). Secondly, the calculations from chapter 6 are carried out more than once, namely for several disturbances.



# Appendix B

## Implementation aspects

Several numerical codes are used to generate the data that form the basis for our conclusions as done in this report. Here, we give some technical details about the codes that are used. From the spectrum of turbulence modelling (DNS, LES and RANS), a Large Eddy Simulation and a Reynolds-Averaged Numerical Simulation are used; the latter (made Transient) with a kinematic simulation added.

### B.1 Non-dimensionality

In the first chapter, it was already noted that a flow is fully governed by the Navier-Stokes equations, which turned out to contain just one parameter, namely the Reynolds-number  $Re$ . This Reynolds-number is defined by a characteristic velocity, a characteristic length-scale and the molecular kinematic viscosity:

$$Re = \frac{UL}{\nu} \tag{B.1}$$

The LES-code has such been programmed, that the Reynolds-number can be interpreted as an inverse molecular kinematic viscosity, which is only possible if  $U = 1$  and  $L = 1$ . Hence, all the velocities and length-scales within the calculations are scaled with  $U = 1$  and  $L = 1$ . Sometimes, the quantities  $U$  and  $L$  can be physically interpreted. For instance, at the calculation on the channel flow, we can define a friction velocity  $u_\tau$  equal to unity to scale all the velocities with. This  $u_\tau = 1$  is again consistent with the use of a pressure-gradient equal to unity (see equations (3.37) and (3.38)). In this case, the Reynolds-number as defined by (B.1) can be interpreted as a friction-velocity-based Reynolds-number  $Re_\tau$ . Furthermore, the depth  $D$  can be chosen for the typical length-scale  $L$ .

In other cases, for instance, the vorticity-checkerboard and the grid-flow from Chapter 5, another typical velocity  $U$  can be chosen. In the vorticity-checkerboard-case the amplitude  $U_0 = 1$  can be used for scaling, in the grid-flow-case the mean velocity (again equal to unity) can be chosen for scaling. In the grid-flow-case from Chapter 6, together with the calculations with kinematic simulation, again the friction velocity  $u_\tau$  can be chosen for scaling.

The timestep  $dt$  is defined using

$$dt_{inv} = \max \left( \frac{u}{dx} + \frac{v}{dy} + \frac{w}{dz} + \frac{\nu}{dx^2} + \frac{\nu}{dy^2} + \frac{\nu}{dz^2} \right) \tag{B.2}$$

and the Courant-Friedrich-Lewy number ( $CFL$ ):

$$dt = \frac{CFL}{dt_{inv}} \quad (\text{B.3})$$

Using a Adams-Bashforth scheme, we choose  $CFL = 0.35$ .

## B.2 Large Eddy Simulation

In this section we will make some remarks on important, basic elements as used in the LES-code. This LES-code uses non-periodic boundaries in the  $z$ -direction. The boundaries as referred to in the following, are the boundaries in  $x$ -direction and  $y$ -direction.

### B.2.1 The algorithm

#### All boundaries periodic

For the calculations on the channel flow and the vorticity checkerboard, all the boundaries are periodic. The algorithm that is used, is as follows:

```

call init
call boumpj
do istap = 1,nstap
  call submod
  call bouprj
  call chkdt
  time = time + dt
  call adamsb
    call momx
    call momy
    call momz
  call boumpj
  call fillps
  call solmpj
  call bouprj
  call boumpj
  call boumpj
  call chkdiv
enddo

```

In this algorithm the subroutines `boumpj` and `bouprj` apply the boundary conditions on the velocities and on the viscosity and the pressure, respectively. The subroutine `submod` contains the Smagorinsky subgrid-model. The subroutine `adamsb` is the temporal integration routine for the momentum equations and invokes the spatial integrations routines `momx`, `momy` and `momz`, for the  $x$ -,  $y$ - and  $z$ -direction respectively. The subroutine `fillps` (*cf.* equation (3.35)) fills the Poisson-matrix, which is solved by subroutine `solmpj`. The solver algorithm is based on Fast Fourier Transformations instead of a Krylov method. Without going into detail here, the boundaries are of the type *Neumann* in order to avoid wiggles.

### One boundary periodic

For the grid-turbulence case, we used an LES-algorithm, which is slightly different from the algorithm for channel flow, as we have, in this case, a non-periodic boundary in  $x$ -direction. Therefore, two things change. Firstly, the solver is changed (we do not go into detail at this point). Secondly, some rules are added in order to make a correction such that the inflow exactly equals the outflow.

### B.2.2 The wall-function

In chapter 3, the Grötzbach-wall-function is described (see equation (3.13)). This wall-function is implemented as follows:

```

utau = 1
do i = 1,25
    utau = umean/(2.439*log(utau/(2.0*dzi*Rei))+5.29)
enddo
tau = utau*utau
do j = 1,jmax
    do i = 1,imax
        u(i,j,1) = u(i,j,1)-(u(i,j,1)/umean)*tau*dt*dzi
    enddo
enddo

```

Here, `umean` is the mean velocity at the most near-wall gridpoint, `dzi` is the inverse grid-cell-size in  $z$ -direction, `Rei` is the inverse Reynolds-number and `dt` is the timestep.

## B.3 Transient Reynolds-Averaged Numerical Simulation

The TRANS-model is based on the depth-averaged, Reynolds-averaged Navier-Stokes equations. In our case, also the bottom-friction is represented (see equations (5.2) and (5.3)). In this section we will do some notions about the implementation of the added kinematic simulation.

### B.3.1 Bottom friction

Using equation (5.5), we can calculate a proper friction coefficient, namely, with

$$u_\tau = \sqrt{c_f \tilde{u}} \quad \text{and} \quad \tilde{u} \approx 18u_\tau,$$

we obtain a friction coefficient  $c_f \approx 0.003$ . This value for the friction coefficient is used.

### B.3.2 Kinematic simulation

In the following, we give a short description of the implementation of the kinematic simulation in the 2D-TRANS-model. For our purpose, we used the model as made by Bram van Prooijen during his research for his dissertation. It should be mentioned that the implementation seems to differ from the description as it is given in Chapter 4. The responsibility for the correctness of the implementation lays at Bram van Prooijen. Notions on the kinematic simulation can be found in Van Prooijen (2003).

The application of the kinematic simulation is handled in four steps. Firstly, the random phases are generated as well as the randomly chosen wavenumbers from the *a priori* known spectrum. After all, with representing only the two-dimensional energy-density spectra in the ways as it is done in Chapters 3 and 4, we lost the phase-information, as we have only the amplitudes. These random phases and 'semi-random' wavenumbers are globally declared within the model. The random vectors have length  $N$ .

Secondly, the perturbations are calculated. This is, for each gridpoint and for each  $N$ , done as follows:

```
Xks = i/dxi
Yks = j/dyi
A = 1.0/(1.0*N**0.5)*alpha*kk*labda*exp(1.-(kk*labda))*(abs(ky/kk))**beta
peru0 = A*(ky/kk)*sin(2*pi*(kx*(Xks+dx)+ky*Yks)+2*pi*phi)
perv0 = A*(kx/kk)*sin(2*pi*(kx*Xks+ky*(Yks+dy))+2*pi*phi)
```

After that, thirdly, the perturbations are coupled with the actual velocities, in the program described with `unew` and `vnew`. Therefore, for each gridpoint and for each  $N$ , the following is done:

```
ufil = unew
A = 1.414*sin(2*pi*theta)*ufil*cf**0.5
unew = unew + A*peru0
vnew = vnew - A*perv0
XX = 0.0
```

After these three steps, we only have the initial field. The time-dependency, is, for each gridpoint and for each  $N$ , formulated as follows:

```
A = 1.414*sin(2*pi*XX+2*pi*theta)*ufil*cf**0.5
uksnew = uksnew + A*peru0
vksnew = vksnew - A*perv0
XX = XX - ufil*kx*dt
```

The velocity fluctuations from this algorithm, namely `uksnew` and `vksnew`, are put into the equations (see equations (5.19) and (5.20)).

# Appendix C

## Postprocessing aspects

The calculations produce huge amounts of numbers. For our aimed investigation, the accent is laid on spectral distributions and the development of turbulent kinetic energy and enstrophy. Here, we give a short overview the applied algorithms.

### C.1 One-dimensional spectral distributions

An arbitrary vector  $\mathbf{u}$  is treated according the following algorithm in order to obtain the spectral distribution of turbulent kinetic energy:

- Step 1. Determine the average of vector  $\mathbf{u}$ :  $\mathbf{u}_{\text{mean}}$
- Step 2. Determine fluctuations  $\mathbf{u}_{\text{fluc}} = \mathbf{u} - \mathbf{u}_{\text{mean}}$
- Step 3. Apply windowing to fluctuation vector  $\mathbf{u}_{\text{fluc}}$ , because of data-leakage
- Step 4. Apply the 1D-Cooley/Tukey FFT algorithm
- Step 5. Normalise the obtained periodogram, to account for the windowing

The wavenumber vector  $\mathbf{k}$  is defined on  $\left[ \frac{2\pi}{L_x}, \frac{2\pi}{2dx} \right]$ , where  $L_x$  is the domain-length in  $x$ -direction and  $dx$  the gridsize in the corresponding direction.

### C.2 Two-dimensional spectral distributions

An arbitrary matrix  $\mathbf{U}$  is treated according the following algorithm in order to obtain the spectral distribution of turbulent kinetic energy:

- Step 1. Determine the average of matrix  $\mathbf{u}$ :  $\mathbf{u}_{\text{mean}}$
- Step 2. Determine fluctuations  $\mathbf{u}_{\text{fluc}} = \mathbf{u} - \mathbf{u}_{\text{mean}}$
- Step 3. Apply the 2D-Cooley/Tukey FFT algorithm
- Step 4. Normalise the obtained periodogram (in 4 quadrants) to 1 quadrant

The wavenumber vectors  $\mathbf{k}_x$  and  $\mathbf{k}_y$  are defined on  $\left[ \frac{2\pi}{L_x}, \frac{2\pi}{2dx} \right]$  and  $\left[ \frac{2\pi}{L_y}, \frac{2\pi}{2dy} \right]$  respectively, with  $dx$  and  $dy$  the gridsizes.

## C.3 Averaging algorithms

The most important averaging algorithms that are applied during our research, is the depth-averaging algorithm in the channel flow case, and the energy-averaging algorithm in the grid-flow case.

### C.3.1 Depth-averaged velocity maps

The applied LES on the channel flow resulted in large 3D-arrays with velocities  $u$ ,  $v$  and  $w$ . For the depth-averaged velocity maps as input for a two-dimensional spectral distribution algorithm only the  $u$ - and  $v$ -velocities are of importance. Let  $k$  be the grid-number counter in  $z$ -direction and let  $u(:, :, k)$  be a 2D-array with velocity maps at grid-number  $k$ , then the averaging-procedure is as follows (in Matlab-oriented terms):

- Step 1. For each  $k$ : `ufluc(:, :, k) = u(:, :, k) - mean(mean(u(k)))`
- Step 2. Average the matrices `ufluc(:, :, k)` in  $k$ -direction
- Step 3. If wanted, apply spectral algorithm

This algorithm results in depth-averaged velocity fluctuation maps.

### C.3.2 Grid-flow

In order to obtain an energy-curve in  $x$ - direction, the following procedure is followed, assuming the presence of  $n$  velocity arrays in a 2D configuration:

- Step 1. Average the velocity maps in time (over  $n$ )
- Step 2. Average the resulting velocity map in transverse direction (over  $j$ )
- Step 3. For each  $n$  and  $i$ , apply: velocity map minus mean velocity-vector
- Step 4. For each  $n$ , calculate the amount of turbulent kinetic energy
- Step 5. Repeat Step 1 and Step 2, but now for the 2D energy arrays

with  $i$  and  $j$  the grid-number counters in  $x$ - and  $y$ - direction respectively.



## Appendix D

# List of Symbols

---

**LATIN**

---

$c_f$	friction coefficient
$C_s$	Smagorinsky constant
$D$	water-depth
$dt$	timestep
$dx$	gridsize in $x$ -direction
$dy$	gridsize in $y$ -direction
$dz$	gridsize in $z$ -direction
$E$	turbulent kinetic energy
$E_{uu}$	energy-densities of streamwise velocity fluctuations
$E_{vv}$	energy-densities of transverse velocity fluctuations
$E_{uu}^i$	circular integrated equivalents of 2D spectra $E_{uu}$
$E_{vv}^i$	circular integrated equivalents of 2D spectra $E_{vv}$
$F$	forcing term
$G$	filter function
$h$	water-height
$i$	counter in $x$ -direction
$i$	integer in index-notations
$j$	counter in $y$ -direction
$j$	integer in index-notations
$k$	counter in $z$ -direction
$k_i$	wavenumber vector with components $k_x$ , $k_y$ and $k_z$
$L$	characteristic length-scale
$L_x$	domain-length in $x$ -direction
$L_y$	domain-length in $y$ -direction
$L_z$	domain-length in $z$ -direction
$l_m$	mixing-length
$N$	integer
$n$	integer
$N_x$	number of gridpoints in $x$ -direction
$N_y$	number of gridpoints in $y$ -direction

---

LATIN(continued)	
$N_z$	number of gridpoints in $z$ -direction
$\mathcal{O}$	Landau's order symbol
$p$	pressure
$q_{ij}$	Reynolds stress tensor
$q_t$	total amount of turbulent kinetic energy
$Re$	Reynolds-number
$Re_\tau$	friction-velocity based Reynolds-number
$R$	Fourier-transform of the autocovariance function
$r$	autocovariance function
$S_{ij}$	rate of strain tensor
$T$	characteristic time-scale
$t$	time
$U$	characteristic velocity
$\mathbf{u}$	vector notation of the velocity-vector
$u_i$	index notation of the velocity-vector
$u$	streamwise velocity
$u_*$	friction velocity
$u_\tau$	volume-integrated friction velocity per unit of mass
$u^+$	$u$ normalised with $u_\tau$
$u'$	fluctuation of the streamwise velocity
$V_f$	grid-cell volume
$v$	transverse velocity
$v'$	fluctuation of the transverse velocity
$w$	wall-normal velocity
$w'$	fluctuation of the wall-normal velocity
$x_i$	index notation of the coordinate-vector
$x$	coordinate in streamwise direction
$y$	coordinate in transverse direction
$z$	coordinate in wall-normal direction
$z^+$	non-dimensional wall-coordinate
GREEK	
$\alpha$	empirical constant
$\beta$	empirical constant
$\Delta_f$	filter-length
$\delta_{ij}$	Kronecker delta
$\delta_n$	intensity of disturbances
$\epsilon$	energy-dissipation
$\eta$	rate of enstrophy transfer
$\theta$	phase
$\kappa$	Von Karman constant
$\Lambda$	length-scale of a coherent structure
$\lambda$	wavelength
$\lambda$	length-scale
$\lambda$	empirical constant

---

GREEK(continued)

---

$\mu$	dynamic viscosity
$\nu$	molecular kinematic viscosity
$\nu_t$	turbulence viscosity
$\rho$	density
$\tau$	wall shear-stress
$\tau$	time-scale
$\varphi$	arbitrary quantity
$\phi$	phase
$\psi$	streamfunction
$\Omega$	enstrophy
$\Omega_{ijk}$	the computational domain
$\omega$	vorticity
$\omega$	angular frequency

---

ABBREVIATIONS

---

2D	two-dimensional
3D	three-dimensional
DNS	Direct Numerical Simulation
ks	kinematic simulation
LES	Large Eddy Simulation
MKM	Moser, Kim and Mansour
RANS	Reynolds-Averaged Numerical Simulation
SGS	subgrid-scale
TRANS	Transient Reynolds-Averaged Numerical Simulation

---

# Nawoord

Dit nawoord is het slotakkoord van het project waar ik het afgelopen jaar met plezier aan gewerkt heb. Een project waarbij ik uitvoerig kennis heb mogen maken met de numerieke aspecten van de vloeistofmechanica. Op deze plek is een woord van dank voor de mensen, die mij hebben ondersteund gedurende het project, dan ook zeer op zijn plaats. In dit kader denk ik in eerste instantie aan Wim Uijttewaal: bedankt voor de goede begeleiding en de immer aanwezige bereidheid om vragen te beantwoorden. Ik heb de samenwerking altijd als uitstekend en prettig ervaren. Daarnaast gaat een bijzonder woord van dank uit naar Harmen Talstra: bedankt voor het feit dat je zo vaak bereid was in discussie te gaan over het onderwerp en voor het delen van de vakkennis die je op dit gebied hebt. Tevens wil ik, bij deze, mijn dank uitspreken aan prof. Guus Stelling en Garth Wells voor de feedback op het onderzoek en de scriptie.

Natuurlijk wil ik, bij deze, ook alle mensen die in en om de kamer, waar ik het afgelopen jaar zat, bijgedragen hebben aan de gezelligheid en de goede sfeer, die er eigenlijk altijd wel was, hartelijk bedanken. Hierbij denk ik vooral aan de leuke discussies en gesprekken met mijn kamergenoten, de verhalen van beide buurmannen en de gesprekken bij de koffie.

Tot slot wil ik graag ook God bedanken voor Zijn steun en zegen tijdens dit afstudeerproject. Ervan uitgaande en gelovende dat God de wereld heeft geschapen en onderhoudt, is het fascinerend om te zien hoeveel moeite een mens moet doen om een stukje van Zijn schepping in kaart te brengen. Dit laat, mijns inziens, zien hoe magistraal de schepping in elkaar zit en dat enerzijds de wetenschap tot veel in staat is, maar anderzijds beperkt is vergeleken met Zijn scheppende kracht. Zo ben ik het met Blaise Pascal eens, dat er een veelheid aan dingen is die het menselijk verstand te boven gaan. Maar wetende in Wiens handen we ons bevinden lijkt me dat feit geenszins verontrustend.